Characterising Electrolyte Interactions with Carbon Anodes for Sodium Ion Batteries

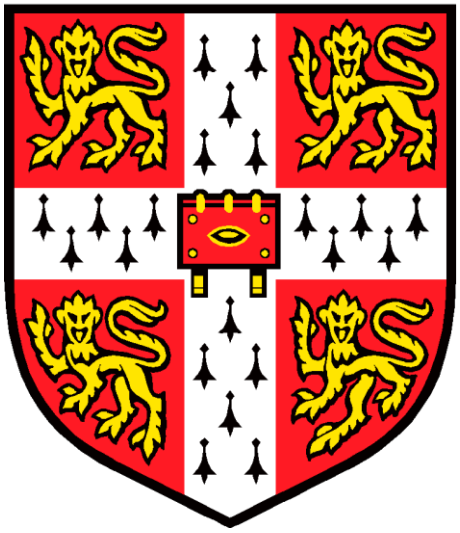

Thomas Henry Smith

Department of Chemistry

University of Cambridge

Clare College

January 2022

This thesis is submitted for the degree of Doctor of Philosophy

Declaration

This thesis is the result of my own work and includes nothing which is the outcome of work done in collaboration except as declared in the Preface and specified in the text. I further state that no substantial part of my thesis has already been submitted, or, is being concurrently submitted for any such degree, diploma or other qualification at the University of Cambridge or any other University or similar institution except as declared in the Preface and specified in the text. It does not exceed the 60,000 word limit prescribed by the Degree Committee for the Faculty of Physics and Chemistry.

Thomas Henry Smith

January 2022

Abstract

Characterising Electrolyte Interactions with Carbon Anodes for Sodium Ion Batteries

Thomas Henry Smith

Battery technologies are of fundamental importance to the modern world and the current development of electric vehicles, as well as grid storage of renewable energy, is placing an increased demand on Li-ion batteries (LIBs). Na-ion batteries (NIBs) are seen as a promising alternative to LIBs due to their lower cost and environmental impact. As Na has a similar chemistry to Li, the transfer of battery technology is also expected to be straightforward, but this is not always the case. For example, graphite is the most common anode for LIBs; however, it is not able to accommodate Na under normal circumstances. Disordered hard carbons are often used instead, this is despite their structure and sodiation mechanism not being fully understood. The choice of electrolyte for a battery is critical and if certain electrolyte solvents such as diglyme are used, co-intercalation of Na into graphite occurs. In Chapter 3, the interactions between diglyme molecules and graphite are investigated using various techniques, including nuclear magnetic resonance spectroscopy and thermogravimetric analysis. Similar techniques were then also used to provide evidence that diglyme also co-intercalates into the disordered hard carbons that are normally used as anodes, albeit to a lesser extent than in graphite.

Chapter 4 sets out to probe the dynamics of diglyme co-intercalated into hard carbon using ^{2}H NMR and simulations, and then use the dynamics of diglyme as an indirect probe for the structure of hard carbon. It was found that the motion of diglyme can be described by simulating a molecular rotation of diglyme with a lognormal distribution of rotation rates, which is indicative of the range of different sites that Na-diglyme complexes can occupy in hard carbon. By probing hard carbon at different states of charge, it was also found that the motion of diglyme increased on sodiation, indicating that hard carbon expands as Na intercalates into the structure, giving diglyme more space to move in. By comparing hard carbons with different capacities, it was also found that as capacity increases, the motion of diglyme decreases, possibly reflecting the increasingly graphitic nature of high-capacity hard carbons.

Within a NIB, the surface layer that forms on the anode during cycling, i.e., the solid electrolyte interphase (SEI), is of crucial importance to the performance of the battery as it inhibits the transfer of electrons whilst also allowing the desired Na^{+} ions to pass through. Despite this, the structure and composition of the SEI in NIBs is not fully characterised. There have been several works that aim to study the SEI formed on hard carbon; however, these reports study hard carbons cycled in half-cells where Na metal is used as a counter electrode. Commercial NIBs would be full-cells that use high

voltage cathodes, such as transition metal oxides, and it is likely that that the SEI formed in half-cells will be heavily influenced by Na metal as it is a strong reducing agent. Therefore, in Chapter 5 we study the SEI formed on hard carbon anodes in full- and half-cells compared using a combination of NMR and X-ray photoelectron spectroscopy (XPS). For half-cells, it was found that SEI forms more quickly than full-cells, even before any cycling has taken place. Furthermore, whilst all SEIs were composed of species such as NaF, Na alkyl carbonates and $NaPO_2F_2$, half-cells had an increased amount of polymeric species in their SEIs compared to the full cells.

I would like to dedicate this thesis to my parents and to Hannah.

Acknowledgements

There are many people I need to thank for helping me to complete my PhD, and my apologies go to anyone that I have missed out. First and foremost, I would like to thank my supervisor Professor Clare Grey for giving me the opportunity to work in her group in such an exciting and important field of science. Additionally, I would like to thank the Engineering and Physical Sciences Research Council (EPSRC) and Shell for funding my project (*via* I-Case studentship EP/R512461/1), with a special thanks to Dr Peter Klusener and Dr Nicola Menegazzo of Shell for encouraging collaboration with other groups and providing many thought-provoking discussions throughout my PhD.

Within the Grey group, I would like to thank all past and present members for making me feel at home and providing a supportive atmosphere. However, there are some members I would like to single out. I would like to thank Dr Lauren Marbella and Dr Pierrick Berruyer for supporting me through the first year of my PhD. I would particularly like to thank Dr Christopher O'Keefe for not only teaching me NMR, but also for providing (both scientific and non-scientific) day-to-day support during my PhD, as well as proofreading this thesis. I would also like to thank Dr Chao Xu for his help, especially with electrochemistry, particularly in the early days of my PhD.

A big thank you also goes out to all PhD other students in my year group, as well as the other members of the fishbowl office for making the last few years so enjoyable. Elsewhere in Cambridge, I would like to acknowledge use of the Cambridge XPS System, part of Sir Henry Royce Institute - Cambridge Equipment, EPSRC grant EP/P024947/1 and thank Dr Carmen Fernandez-Posada for her help with XPS.

A special thank you goes out to my parents, Margaret and Richard, for all of your support, without whom I would not have made it this far. Finally, I would like to thank Hannah for being so kind, supportive and understanding throughout my PhD (and the three and half years before!) especially when work has not stayed in the office and has encroached on evenings and the weekends.

Table of Contents

List of Figures

List of Tables

Abbreviations

BET – Brunauer Emmett Teller

CEI – Cathode electrolyte interphase

CMC – Carboxymethyl cellulose

CP – Cross polarization

CT – Central transition

DEC – Diethyl carbonate

DFEC – *trans*-difluoroethylene carbonate

DMC – Dimethyl carbonate

DMSO – Dimethyl sulfoxide

EC – Ethylene carbonate

ES – Ethylene sulfate

EV – Electric vehicle

FEC – Fluoroethylene carbonate

FML – Fast motion limit

FTIR – Fourier transform infrared spectroscopy

FWHM – Full width at half maximum

HAXPES – Hard X-ray photoelectron spectroscopy

IMR – Intermediate motional regime

LIB – Li-ion battery

MAS – Magic angle spinning

MOF – Metal organic framework

NaTf – $NaCF_3CO_3$

NaTFSI – $NaN(CF_3SO_2)_2$

NEDC – Na ethylene decarbonate

NEMC – Na ethylene monocarbonate

NIB – Na-ion battery

NMP – *N*-methyl-2-pyrrolidone

NMR – Nuclear magnetic resonance spectroscopy

NVPF – $Na_3V_2(PO_4)_2F_3$

NVP – $Na_3V_2(PO_4)_3$

PC – Propylene carbonate

PDF – Pair distribution function

PVDF – Poly(vinylidene) fluoride

PVDF-HFP – Poly(vinylidene fluoride-co-hexafluoropropylene)

SANS – Small angle neutron scattering

SARS – Surface enhanced Raman spectroscopy

SAXS – Small angle X-ray scattering

SEM – Scanning electron microscopy

SEI – Solid electrolyte interphase

SML – Slow motion limit

SOC – State of charge

SOLA – Solid lineshape analysis

SSNMR – Solid state nuclear magnetic resonance spectroscopy

ST – Satellite transition

TEM – Transmission electron microscopy

TGA – Thermogravimetric analysis

THF – Tetrahydrofuran

UHV – Ultra-high vacuum

VC – Vinylene carbonate

XAS – X-ray absorption spectroscopy

XPS – X-ray photoelectron spectroscopy

XRD – X-ray diffraction

1 Introduction

Climate change caused by the release of greenhouse gases into the atmosphere is currently one of the biggest problems facing humanity, with increasing temperatures and extreme weather events starting to become the norm.[1] As atmospheric CO_2 levels are now significantly above 400 ppm,[2] significant changes are needed to mitigate the worst effects of climate change. This is evidently a large problem, and the solution will be multifaceted. Part of the solution will be a transition away from burning fossil fuels for energy and an increased use of energy harnessed from renewable resources, such as wind and solar. One of the issues with these sources is that energy is often not supplied at the time it is required, so increased storage capacity for the grid is required.[3] Additionally, other transitions such as the large-scale introduction of electric vehicles[4] (EV) will also require a significant increase in energy storage capacity.

Currently, the state-of-the-art system for energy storage is rechargeable Li-ion batteries (LIBs), which have become ubiquitous in the modern world since their first commercialisation by Sony in the early 1990's,[5] mainly due to their prevalence in portable electronics. This is due to several desirable features including high energy and power densities, long lifetime and high-rate capability.[6,7] The importance of LIBs was highlighted in 2019 when the Nobel Prize in Chemistry was awarded to John B. Goodenough, M. Stanley Whittingham and Akira Yoshino for their work on the development of LIBs. LIBs work on the so-called "rocking chair" model where during discharge, Li^+ ions are transferred from an anode to a cathode through an electrolyte. This process is accompanied by the flow of electrons through an external circuit, generating a current that can be harnessed and the reverse process occurs during charging.

Despite the benefits outlined above, there are some drawbacks associated with LIBs. Most notably, Li has a relatively low natural abundance, and its reserves are limited to a few countries, mainly in South America, and the increased demand for Li has caused a commensurate increase in expense. There are also environmental and ethical concerns associated with the increasing production of Li,[8] as well as other components of LIBs such as Co for the cathodes.[9] Therefore, the development of alternatives to LIBs is highly desirable, and one of these alternatives is Na-ion batteries (NIBs). NIBs are analogous to LIBs and were originally developed at the same time as LIBs.[10] However, research efforts focused on LIBs as the specific capacities are higher than those of NIBs. But given the recent increase in interest for energy storage, NIBs have become an increasingly active area of research.

Na has a similar chemistry to Li and is more readily available, it is approximately one thousand times more abundant than Li in the earth's landmass[11] and more evenly distributed. As Na also does not alloy with Al, the more expensive Cu does not have to be used as a current collector, further reducing costs. These cost savings add up to make NIBs potentially 10 % cheaper per energy unit.[12] Many of the most promising cathodes for NIBs also do not contain any Co;[12] meaning NIBs are seen as being

potentially cheaper and more environmentally friendly way of storing energy. However, the larger ionic size of Na^+ (1.02 Å) compared to Li^+ (0.76 Å)[13] corresponds to a lower charge density. This means NIBs are unlikely to replace LIBs for applications where size is the main driving factor, such as portable electronics, and to a lesser extent EVs. But for applications where cost, not size is the primary concern, such as grid storage of renewable energy, NIBs are increasingly seen as an attractive solution. Moreover, the lower cost of NIBs, combined with good energy density means they are also seen as being a competitor to more traditional Pb-acid batteries, which have very limited energy densities, as well as containing toxic Pb.[14] Hence, several companies have recently emerged to develop commercial NIBs including (but not limited to): Faradion (UK), Tiamat (France), HiNa (China) and Novasis (USA).

NIBs work using the same "rocking chair" principle as LIBs, where during discharge, Na^+ ions and electrons are released from an anode (negative electrode). The Na^+ ions then transfer through an electrolyte, and electrons transfer through an external circuit, to a cathode (positive electrode), where the Na^+ ions and electrons combine with the cathode material. Then during charging the reverse process occurs and Na^+ ions are transferred back from the cathode to the anode, as demonstrated in Figure 1-1. A separator, not shown, is present between the electrodes, to prevent them from making contact which would cause the battery to short-circuit and fail.

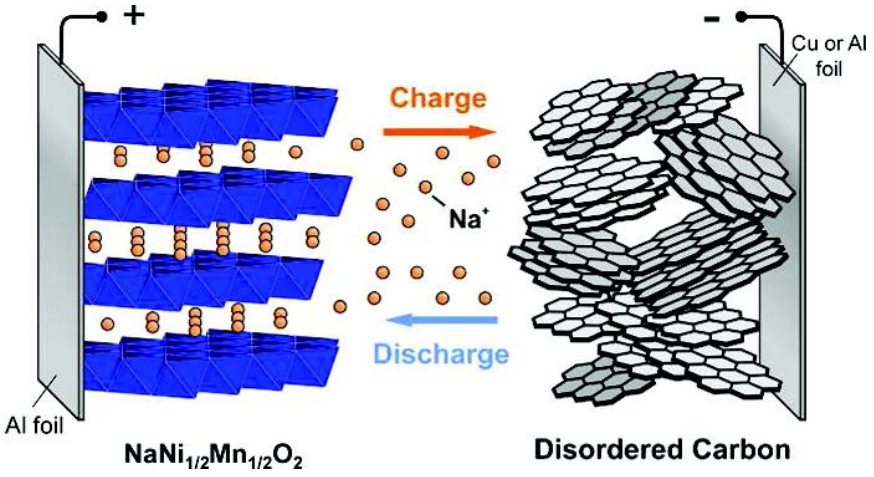

Figure 1-1: A diagram showing the working of a NIB, reproduced with permission from reference.[15] *Copyright 2011 American Chemical Society.*

1.1 Anodes

For LIBs, the ideal anode would be Li metal as it has an extremely high theoretical capacity (3860 mAh g^{-1}) and the lowest negative chemical voltage (– 3.04 V vs. a standard hydrogen electrode).[16] However, the use of Li metal as an anode is limited by practical issues relating to the growth of dendrites and electrolyte degradation, both of which lead to a poor electrochemical performance.[17] That being said, in academic research both anodes and cathodes are often tested in cells with Li metal as a counter electrode (so called "half-cells", as opposed to "full-cells" where more typical anodes and cathodes are used (*vide infra* Section 2.1). The most common anode material for commercial LIBs is graphite, which

is a layered, crystalline material of sp^2-bonded graphene sheets held together by van der Waals forces. This is because it is cheap, abundant, has a good cycling stability and relatively small volumetric expansion on lithiation (~10 %).[18] The reversible intercalation of Li^+ ions into graphite to the intercalation compound LiC_6 is given below:

$$C_6 + Li^+ \leftrightarrow LiC_6 \quad (1.1)$$

The intercalation of Li into graphite has been well studied, and it is understood to occur by a staged insertion mechanism. These stages are denoted as stage *n*, which corresponds to a layer of Li separated by *n* carbon layers. On increased lithiation, *n* decreases such that by stage 1 (which corresponds to full lithiation) there are alternating layers of Li and C.[19] Na however, intercalates very poorly into graphite (the equivalent intercalation compound formed is NaC_{64}),[20] which corresponds to a very low capacity. At first, this might be attributed to the greater ionic radius of Na^+ (1.02 Å) compared to Li^+ (0.76 Å), meaning that the spacing between graphene layers in graphite is too small to accommodate Na^+ ions.[21] However, it has been shown that K^+ and even larger alkali metal ions are able to intercalate into graphite.[22] Moriwake *et al.*[23] showed that intercalation becomes more favourable for elements further down group one of the periodic table as ionic interactions between the cations and graphite increase in strength. Li is the exception to this rule, as Li-C bonds have a significant covalent character which stabilises the Li intercalation compounds. Unfortunately, for NIBs, Na intercalation into graphite is not stabilised by ionic or covalent interactions and is therefore energetically unfavourable.

It is therefore evident that a different material is required for NIB anodes. As opposed to crystalline graphite, disordered forms of carbon are used as anode materials. These disordered carbons are split into two groups: hard and soft carbons. Hard (non-graphitizing) carbons which are not transformed to graphite on heating (up to 3000 °C) in an inert atmosphere and soft (graphitizing) carbons which can be transformed to graphite on heating in an inert atmosphere.[24] Of these materials, hard carbons are often used as anodes in NIBs (as well as LIBs, but to a lesser extent). These hard carbons are typically prepared by heating sugars[25] or other naturally occurring biomaterials[26] under Ar or N_2 at temperatures in excess of 1000 °C. The structure of hard carbon was traditionally described by the "house of cards" model[27] which states that hard carbon consists of randomly arranged turbostratic graphitic domains (i.e. when there graphene sheets are randomly stacked with no long range order), with a large amount of internal porosity. This is illustrated in Figure 1-2, where the lines represent individual graphene sheets.

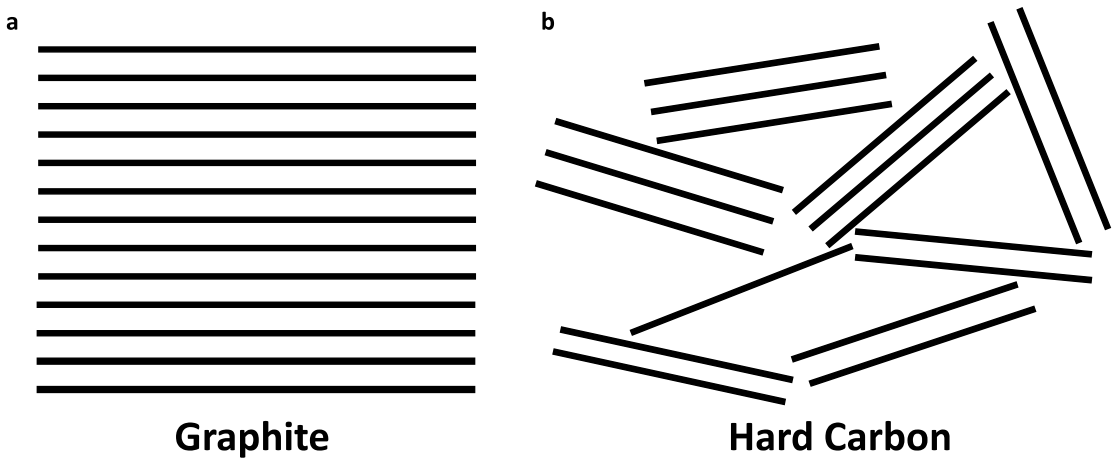

Figure 1-2: Schematics of the structure of (a) graphite and (b) the "house of cards" model of hard carbon.

Due to the disordered nature of hard carbons, several different techniques have been used to analyse them. X-ray diffraction (XRD) is of limited use as only two broad reflections are observed in diffraction patterns: (002) and (100). The first of these relates to the interlayer spacing and the second corresponds to the lateral extent of the carbon layers.[28] Raman spectroscopy is often used to give an estimate of defect concentration (such as 5- and 7- membered rings) by comparing the relative intensities of the D and G bands, which correspond to the E_{2g} graphitic mode and the defect induced mode, respectively.[29] Transmission electron microscopy (TEM)[30] provides a snapshot of the level of order in a hard carbon as well as showing how "graphitic" the hard carbon is. However, this is not a quantitative measure and the small area analysed means it is not necessarily representative of the whole material.

More detailed information about hard carbons come from techniques such as pair distribution function (PDF) and small angle X-ray scattering (SAXS). PDF provides information about the coherence length of the graphitic domains (typically 2-4 nm), the number of stacked carbon layers (typically 2-10 nm), as well as information about the sheet curvature.[31] Whilst SAXS provides further information about the carbon layer spacings (typically 3.5-3.8 Å) and the size of the pores (1-5 nm).[32] Furthermore, the relatively low surface area of hard carbons as determined by Brunauer-Emmett-Teller (BET) surface area analysis (on the order of 10 $m^2\ g^{-1}$)[33], suggests that the BET gases are not able to access the internal porosity of hard carbon.[34]

Based on this information, more recent studies[33,35] have described the structure of hard carbon as consisting of curved graphitic sheets, with a larger amount of internal porosity where the degree of curvature relates to the number of defects, this structure is demonstrated in Figure 1-3. It has also been shown that the properties of hard carbons can be tuned by preparing them at different temperatures.[33] With higher temperatures, corresponding to larger stack sizes, pores and basal plane sizes. Whilst the defect concentration and interlayer spacings decrease with increased temperature, although the spacings never reach that of graphite (3.3 Å)[36] due to the curved nature of the sheets.

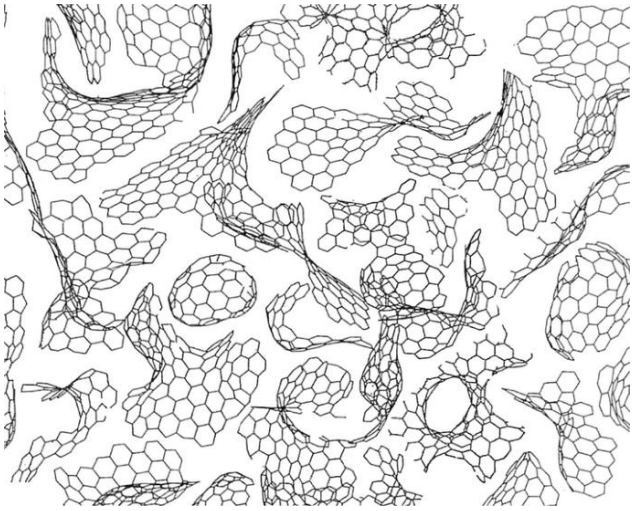

Figure 1-3: A more accurate model of the structure of hard carbon, consisting of curved carbon sheets, reproduced with permission from reference.[37] *Copyright 2013 Springer.*

Figure 1-4 shows the voltage profile of the first sodiation of a hard carbon electrode in a Na half-cell, achieving a capacity of approximately 320 mAh g^{-1}. Here, two different cycling domains are observed in the electrochemical voltage profile, a sloping region at higher voltages and a plateau close to 0 V vs. Na. There is some debate in the literature on the physical origin of these two regions. The traditional "house of cards" model proposed that these regions correspond to a two-stage mechanism for the insertion of Na into hard carbon. The first (sloping stage) corresponds to intercalation of Na between carbon layers, this is then followed by pooling of Na within the pores during the low voltage phase.[27] During this process, there is expected to be a partial transfer of electrons from hard carbon to the pooled Na in the pores of the material to form Na^{x+} ($0 < x < 1$),[38] and such species are referred to as quasi-metallic. However, more recent studies have assigned the slope to Na^{+} ions being stored at defects, within interlayers and on pore surfaces, with the plateau still corresponding to pore filling.[33,39]

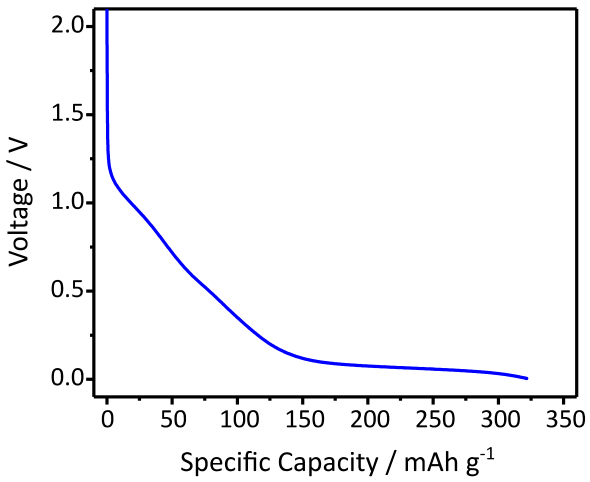

Figure 1-4: Voltage profile for the first sodiation of a hard carbon electrode in a Na half-cell with a 1 M $NaPF_6$ in EC:DMC electrolyte.

Solid state nuclear magnetic resonance spectroscopy (SSNMR) is a useful technique to study hard carbon during sodiation as diamagnetic species can be easily differentiated from metallic species in SSNMR spectra because of a phenomenon known as Knight shift.[40] This is where free moving electrons in a metal introduce an extra field that induces an additional shift. When fully sodiated, the quasi-metallic Na species expected to pool in the pores of the hard carbons should be observable by ^{23}Na SSNMR. However, these quasi-metallic species were not observed in *ex situ* ^{23}Na SSNMR spectra of sodiated hard carbon by Gotoh *et al.*[41] Stratford *et al.*[31] however did observe quasi-metallic Na with both *ex situ* and *in situ* ^{23}Na SSNMR. The authors suggest that Gotoh was unable to observe the quasi-metallic species as they are very air sensitive and degrade quickly, even in a glovebox. The presence of quasi-metallic Na species is good evidence for a pore filling mechanism. An example ^{23}Na SSNMR spectrum for a fully sodiated hard carbon electrode is given in Figure 1-5. In this spectrum, the overlapping peaks near 0 ppm correspond to diamagnetic species such as residual electrolyte and electrolyte degradation products, and the peak at 750 ppm corresponds to quasi-metallic Na that has pooled in the pores of the material. This peak is well outside the expected shift range for diamagnetic compounds and approaches that of Na metal (1100 ppm). It has been shown that higher capacity carbons, where the plateau near 0 V contributes a greater amount of the overall capacity, have larger pores, form larger pools of quasi-metallic Na, as evidenced by this signal becoming shifted closer to the expected shift of metallic Na on full sodiation.[33]

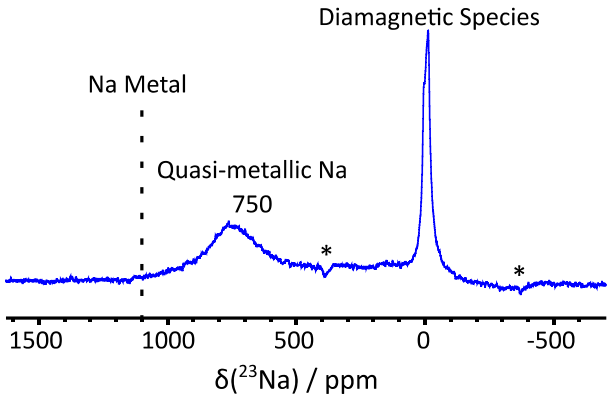

Figure 1-5: ^{23}Na MAS SSNMR spectrum of hard carbon fully sodiated to 5 mV with a 1 M $NaPF_6$ in propylene carbonate electrolyte. A MAS spinning speed to 50 kHz was used, spinning side bands are denoted by asterisks.

Recently, it has been reported that a good electrochemical performance can be achieved for Na intercalation into graphite when diglyme (the molecular structure of which is given in Figure 1-6) is used as an electrolyte solvent, achieving a specific capacity of ~100 mAh g^{-1}.[42] Na insertion into graphite is possible due to the co-intercalation of diglyme solvent molecules and this intercalation is stabilised by van der Waals interactions between diglyme and the graphene sheets. It has been determined through a combination of neutron scattering and empirical potential structure refinement, that each Na^+ ion is coordinated to two diglyme molecules to form the complex $Na^+(diglyme)_2$.[43]

Subsequently, other glymes and crown ethers[44,45] have also been shown to co-intercalate with Na into graphite. This will be discussed in more detail in Chapter 3.

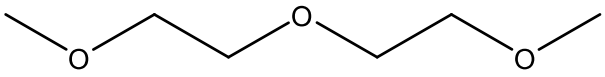

Figure 1-6:The molecular structure of diglyme.

In addition to carbonaceous materials, other materials that are being explored for anodes in NIBs include materials that can alloy with Na. Some examples with high theoretical gravimetric capacities include Sn (847 mAh g^{-1}),[46] Sb (610 mAh g^{-1})[47] and Ge (369 $mAhg^{-1}$).[48] However the stress and strain that these anodes experience over cycling limits their long term cyclability. Other intercalation anodes include titanates, such as $Na_2Ti_3O_7$[49]. This material has an open structure and a safe operating voltage (0.3 V vs. Na^+/Na), but it is practical uses are limited by poor electronic conductivity.

1.2 Cathodes

Transition metal oxides (such as $LiCoO_2$)[50] are the most popular cathode materials for LIBs, due to their high operating potentials and capacities, low discharge and good long-term cycling performance.[51] These materials have structures that consist of layers of transition metal oxide that are separated by layers of Li. On charging, Li is removed from the layers, creating crystallographic vacancies, and on discharge Li intercalates back into the vacancies. Due to the parallels between the technologies, layered transition metal oxides have been investigated as cathode materials for NIBs. For use in NIBs, there is a desire to move away from elements such as Co and Ni, as these elements are toxic and expensive (there are also ethical and environmental concerns about extracting them), and towards more earth abundant, cheaper, and less toxic elements such as Fe and Mn. Fortunately for NIBs, materials such as $NaFeO_2$ have been shown to be electrochemically active unlike their Li equivalents.[52] As Na^+ ions are larger than Li^+ ions, 4-coordination tetrahedral sites, which are reasonably common for Li^+, are rare for Na^+ and 6-coordination sites are more common. The coordination environment for Na^+ is denoted as either O for octahedral or P for prismatic, the latter of which is not observed for the Li equivalents. These letters are then followed by a number which relates to the number of transition metal layers in the stacking repeat unit.[53]

Na transition metal oxides (Na_xMO_2) frequently used in NIBs generally have P2 and O3 as the most common phases.[54] Typically, P2 structures have a less than stoichiometric amount of Na ($x < 1$), which limits their capacity. Whilst O3 phases (Na_1MO_2) have a stochiometric amount of Na that improves the capacity, these electrodes have issues with kinetics that limit their rate capabilities. Therefore, attempts have been made to improve the overall electrochemical performance by combining P2 and O3 phases.[55]

In addition to layered transition metal oxides, other classes of anode materials for NIBs are also being investigated. One of these groups are three-dimensional polyanionic phases such as $Na_3V_2(PO_4)_2F_3$ (NVPF) and $Na_3V_2(PO_4)_3$ (NVP). Whilst the bulky anions would likely limit the energy density of these materials, the stronger covalent bonding of the anions is expected to improve the long-term cycle life of these cathodes. Of these materials, NVPF is often reported as one of the best cathodes for NIBs,[56] as its structure has open channels to allow Na^+ diffusion, but the synthesis is sometimes difficult to control. The synthesis of NVP however, is easier to control and there is a good electrochemical performance with a plateau at 3.4 V that corresponds to V^{3+}/V^{4+}. However, NVP has a poor ionic conductivity which means rate capability is limited and the materials have to be carbon coated.[57] Another issue for these anode materials is the toxicity of V.

Another class of materials used as cathodes are Prussian Blue analogues, such as $NaMnFe(CN)_6$. These materials are easy to synthesis and have an open face-centred cubic structure that can easily accommodate the insertion of larger Na^+ ions and allow for their diffusion, leading to high-rate capabilities. However structural defects limit their capacity and long term cyclability.[58]

1.3 Electrolytes

The ideal electrolyte for a NIB must be ionically conducting, whilst also electronically insulating and it should also have a reasonable electrochemical stability.[59] The electrolyte consists of two major components; a Na salt and a solvent. Typically, the salts used in NIBs are the Na equivalents of the salts that are commonly used in LIBs; such as $NaPF_6$, $NaClO_4$, $NaCF_3SO_3$ (NaTf) and $NaN(CF_3SO_2)_2$ (NaTFSI). Generally, $NaPF_6$ and $NaClO_4$ have good ionic conductivities and electrochemical stabilities. However, these salts have safety issues as ClO_4^- is a strong oxidant and is typically banned for any practical cells, and in the presence of water, PF_6^- hydrolyses leading to the formation of HF. Whilst generally being safer, NaTf has a lower conductivity and it is known to corrode current collectors, the later of these issues also effects NaTFSI.[60,61] In practise $NaPF_6$ is often used, especially in academic research as it dissociates well and has a low cost.

1.3.1 Electrolyte Solvents

There are several constraints placed on the solvent used for electrolyte, as the ideal electrolyte solvent needs to be polar (to easily dissolve the Na salt), have a low viscosity (to aid in the diffusion of Na^+ ions), have a large liquid range, be safe and economical. Therefore, the solvents that are typically used are organic molecules such as carbonate esters or ethers. Cyclic carbonate esters are of particular interest due to their high polarity. For example, propylene carbonate (PC) was originally used for both LIBs and NIBs due to its high dielectric constant (64.9 at room temperature)[62] and large liquid range (–48.8 °C – 241.6 °C)[63]. However, PC was eventually replaced in LIBs by ethylene carbonate (EC), as PC intercalates between graphene layers in graphite and then decomposes, forming gaseous species such as propene. This causes exfoliation of graphite, ultimately leading to disintegration of the graphite

particles and a poor electrochemical performance.[64] Conversely, EC passivates the surface of graphite (forming a stable solid electrolyte interphase, *vide infra*, Section (1.4)) and no exfoliation occurs, leading to a more stable electrochemical performance. However, as EC is a solid at room temperature (its melting point is 36.3 °C)[63], it has to be mixed with another solvent. Typically, linear carbonate esters, such as dimethyl carbonate (DMC) or diethyl carbonate (DEC), are used as they have a low viscosity and are liquid at room temperature, although they have a lower polarity than cyclic carbonate esters. As the hard carbon electrodes used for NIBs are disordered, they do not undergo the same exfoliation process as graphite electrodes, hence PC can still be used for of NIBs.[61] However, it is still common for EC based solvents to be used for NIBs.

Besides the major components outlined above, additives are commonly added to the electrolyte to improve the electrochemical performance. These often improve electrochemical performance by degrading on initial cycles to form a solid electrolyte interphase (*vide infra*) which is a surface layer on the electrode that prevents further degradation and capacity loss. For LIBs several additives have been reported that successfully improve electrochemical performance, including fluoroethylene carbonate (FEC),[65] *trans*-difluoroethylene carbonate (DFEC),[66] ethylene sulfate (ES)[67] and vinylene carbonate (VC).[68] Of these additives, only FEC has been shown to be beneficial in NIBs.[15]

1.4 The Solid Electrolyte Interphase (SEI)

As a NIB (or LIB) is cycled, a solid layer builds up at the interface between the anode and the electrolyte. This layer is called the solid electrolyte interphase (SEI) and it is formed mainly from decomposition products of the electrolyte due to the low operating voltages of the anode. The SEI is of crucial to the performance of a NIB as it prevents further contact between the anode and electrolyte, which would lead to further electrolyte degradation on the anode, whilst also allowing Na^+ ions to transfer from the electrolyte to the anode. The ideal SEI is therefore both an ionic conductor and an electronic insulator. It is also important that the SEI is insoluble in its chemical environment, otherwise the continual addition and removal of SEI would expose the active surface of the electrode, leading to parasitic reactions that could cause heterogeneity in the SEI, and continual breakdown of the electrolyte. Ultimately, this would lead to capacity loss and poor electrochemical performance. Therefore, the ideal SEI would form once on the cell's first cycle and remain there. It is also thought that a similar layer forms on the cathodes called the cathode electrolyte interphase (CEI),[69] but as the cathode operates at higher voltages there are not as many degradation products and consequently the CEI has not been studied to the same extent.

The formation of a stable SEI is one of the reasons why graphite is commonly used as an anode in commercial LIBs, despite Si having a theoretical capacity (3579 mAh g^{-1}) an order of magnitude greater than graphite (372 mAh g^{-1}).[70] On Li intercalation, Si undergoes a volume expansion of ~300 %,[71] compared to the volume expansion on lithiation of ~10 % previously mentioned for graphite. This

means that on each cycle "cracking" of the SEI previously formed occurs, which exposes fresh surface of the electrode. This enables more breakdown of the electrolyte, forming more SEI and a poorer long-term cycling performance than graphite. However, the increased amount of SEI formed, makes analysis of the SEI easier.[72]

In LIBs the SEI is often described by the mosaic model,[73] where the layer closest to the anode consists of inorganic compounds such as LiF, Li_2O and Li_2CO_3 and a second organic layer of polyolefins and semicarbonates is closer to the electrolyte, as demonstrate in Figure 1-7. It is thought that equivalent Na layers exist in NIBs. As Na salts are more soluble than their Li equivalents,[61] it is thought that a greater amount of SEI dissolution occurs for NIBs, leading to a poor electrochemical performance.[74] More information about the SEI in NIBs is provided in Chapter 5.

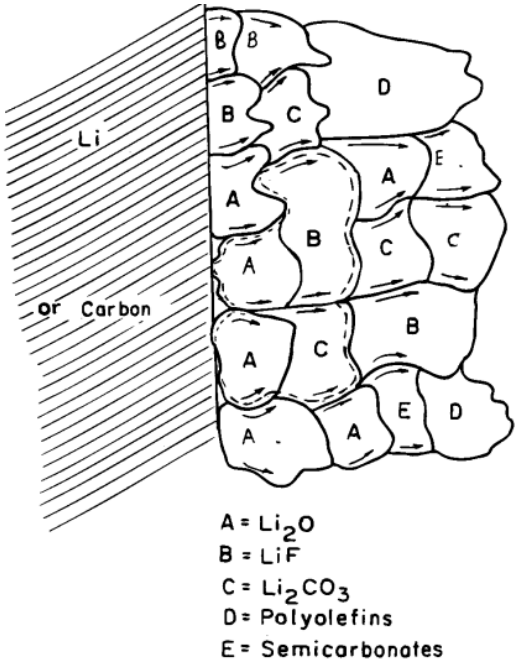

Figure 1-7: A diagram showing the mosaic model of the SEI, reproduced with permission from Reference.[73] *Copyright 1997 The Electrochemical Society.*

1.5 Aims of this Thesis

This thesis sets out to study several interactions between electrolytes and carbon anodes for NIBs. In Chapter 3, the interactions between diglyme molecules and graphite are investigated using various techniques, including SSNMR and thermogravimetric analysis (TGA). Similar techniques were then also used to provide evidence that diglyme also co-intercalates into hard carbons, albeit to a lesser extent than in graphite.

Chapter 4 sets out to probe the dynamics of diglyme co-intercalated into hard carbon using ^2H SSNMR and simulations, and then use the dynamics of diglyme as a probe for the structure of hard carbon. It was found that the motion of diglyme can be described by simulating a molecular rotation of

diglyme with a lognormal distribution of rotation rates, which is indicative of the range of different sites that Na-diglyme complexes can occupy in hard carbon. By probing hard carbon at different states of charge, it was also found that the motion of diglyme increased on sodiation, indicating that hard carbon expands on sodiation, giving diglyme more space to rotate in. By comparing hard carbons with different capacities, it was also found that as capacity increases, the motion of diglyme decreases, possibly reflecting the increasingly graphitic nature of high-capacity hard carbons.

In Chapter 5 the SEIs formed on hard carbon anodes in full- and half-cells are compared, as it is expected that the SEI in half-cells will be heavily influenced by the presence of Na metal as it is a strong reducing agent. To do this, a combination of NMR and X-ray photoelectron spectroscopy (XPS) was used. For half-cells it was found that the SEI forms more quickly than full-cells, even before any cycling has taken place. Furthermore, whilst all SEIs were composed of species such as NaF, Na alkyl carbonates, $NaPO_2F_2$, half-cells had an increased amount of polymeric species for in their SEIs, compared to the full cells.

2 Methodologies

2.1 Electrochemical Methods

When investigating electrodes for NIBs in an academic setting, electrodes are often tested in half-cells, where the electrode of interest is the working electrode and the counter electrode is Na metal. This means that Na metal is both a source of Na and a pseudo-reference electrode, meaning that the potentials of the working electrode can be referenced against Na/Na^+. This method was used for most of the work reported in this thesis. For practical applications however, half-cells are considered a safety hazard due to the potential for dendrites to form,[75] which could cause the cell to short-circuit.

Therefore for commercial applications, full cells (where true cathodes and anodes are present) are used. For full cells the operating voltage of the cell is the difference between the potentials of the two electrodes. Determining the voltage of each electrode is therefore difficult unless a third reference electrode (which does not take place in the redox process) is used. When cycling full cells it is important that the cell is mass balanced, meaning the overall capacity is the same on both sides of the cell. This is done by taking into account the specific capacity of each electrode and adjusting the mass accordingly. In practise however it is common to have excess capacity on the side of the anode to minimise the risk of plating Na metal on the surface of the anode, as this can be a safety risk.

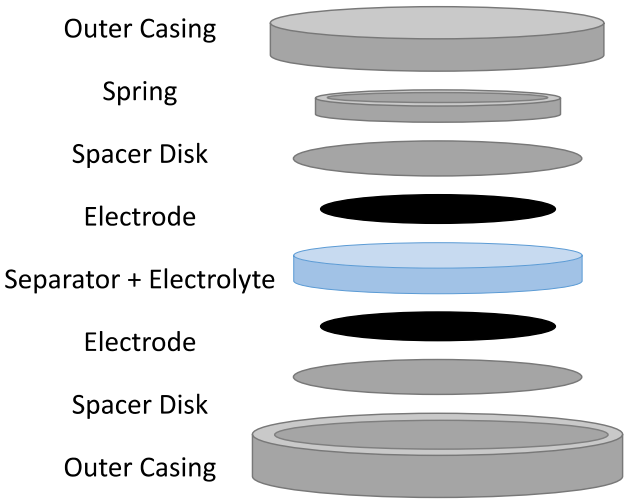

Figure 2-1: An expanded view of a coin cell.

In this work, coin cells (an expanded view of which is given in Figure 2-1) were used to test electrodes, as the cells are relatively easy to assemble and disassemble under an inert atmosphere in a glove box. Specifically, 2032 coin cells were used, which are defined by the dimensions of the cell; a diameter if 20 mm and thickness of 3.2 mm. For all subsequent analysis, the electrodes are recovered from coin cells by disassembly in a glovebox and air sensitive transfer is required the use of an air sensitive sample transfer for the following analysis techniques.

2.1.1 Electrodes

Electrodes for coin cells (both anodes and cathodes) are typically prepared by mixing the active electrode material with a conductive carbon, typically carbon black (later referred to as Super P), and a binder. This mixture is made into a slurry by mixing with a solvent, which is then cast onto a metallic foil (typically Cu or Al) that acts as a current collector. The electrode is then dried to remove excess solvent.

The Super P additive consists of largely amorphous sp^2 hybridised carbon, that forms a chain-like network of spherical particles, with diameters of 20-30 nm.[76] These particles allow for increased contact (and therefore higher conductivity) amongst the active material particles, enabling more efficient insertion and extraction of Na^+ ions and therefore an improved electrochemical performance.[77] Whilst Super P is capable of intercalating Na^+ ions, it has a high surface area which results in a large capacity loss due to the formation of SEI.[78] Hence Super P is generally not used as an active electrode material.

A binder is added to hold the electrode together, commonly used binders are polymers such as poly(vinylidene fluoride) (PVDF), which have high mechanical strength and chemical resistance. However, PVDF binders require toxic *N*-methylpyrrolidone (NMP) to be used as a solvent. Therefore, alternative binders such as carboxymethyl cellulose (CMC) are also used as these binders can use water as a solvent.[79]

2.1.2 Cycling Details

In this work, galvanostatic cycling is used. This is where a constant current is applied to a cell and the voltage of the cell is measured over time (as opposed to potentiostatic measurements, where a constant voltage is applied and the change in current is measured). The rate that galvanostatic cycling occurs at is denoted as a *C*-rate, where *C* corresponds to one full charge or discharge in one hour, therefore a rate of *C*/20 corresponds to a charge or discharge takes 20 hours.

The resulting voltage profiles from galvanostatic cycling generally contain two different features: slopes and plateaus. Slopes correspond to solid-solution mechanisms, where the electrode structure (and therefore potential) changes as alkali metal ions are added. Whereas plateaus correspond to a two-phase transition, meaning each ion interacts with the same structure, and the potential does not change.[19]

2.2 Nuclear Magnetic Resonance Spectroscopy

Nuclear magnetic resonance (NMR) spectroscopy is an analysis technique that is very sensitive to different chemical environments, hence it is commonly used in various scientific fields. It was first discovered independently by Purcell[80] and Bloch[81], for which they shared the 1952 Nobel Prize in

Physics. The basis of NMR lies with the magnetic properties of nuclear spins. A nucleus with a non-zero magnetic quantum number (I) generates a magnetic moment $\boldsymbol{\mu}$, as given by:

$$\boldsymbol{\mu} = \gamma \boldsymbol{I} \tag{2.1}$$

where, γ is the gyromagnetic ratio and $\boldsymbol{I}$ is the nuclear spin moment. $\boldsymbol{\mu}$ is quantised into $2I + 1$ directions, which are referred to by the magnetic component quantum number (m_I). Therefore, for an I = 1/2 nucleus there are two spin states: m_I = +1/2 (α) and m_I = -1/2 (β). In the absence of a magnetic field, these nuclear states are degenerate. However, in the presence of an external magnetic field (B_0), the Zeeman interaction removes the degeneracy of the energy levels of α and β and the energy difference between is referred to as the Zeeman energy (E_Z):

$$E_Z = \gamma m_I \hbar B_0 \tag{2.2}$$

where $\hbar$ is the reduced Planck constant. Transitions between α and β are the basis of NMR, and the energy spacing (ΔE_Z) is given by:

$$\Delta E_Z = \gamma \hbar B_0 \tag{2.3}$$

This energy spacing corresponds to the Larmor frequency, v_0 (Hz) or ω_0 (rad s^{-1}), which is given by:

$$\omega_0 = \frac{v_0}{2\pi} = -\gamma B_0 \tag{2.4}$$

The relative populations of the α and β states is given by the Boltzmann distribution:

$$\frac{N_\beta}{N_\alpha} = e^{\frac{-\Delta E_Z}{k_B T}} \tag{2.5}$$

where k_B is Boltzmann's constant and T is temperature. The energy spacing is small such that at room temperature there is a slightly larger population of spins in the α state.

In an NMR experiment, the sample is placed inside a coil, which is attached to an NMR probe and that is placed inside a strong external magnetic field, $\mathbf{B_0}$. The nuclear spins of the sample then either align parallel (α state) or anti-parallel (β state) with $\mathbf{B}_0$. The slightly larger population of the α state results in a bulk magnetization, $\mathbf{M_0}$, which points in the direction of $\mathbf{B_0}$ (defined as the z-axis in the laboratory frame). A radio frequency pulse (at or close to ω_0) is then applied which introduces an oscillating magnetic field, $\mathbf{B_1}$, which perturbs the bulk magnetization away from the z-axis. After the pulse is turned off, the nuclear spins return to precessing around the z-axis. This introduces an alternating current in the coil of the NMR probe, which is detected as a time-domain signal and is known as the free induction decay (FID). The FID decays exponentially as a result of relaxation processes, and when a Fourier transform is applied to the FID, an NMR spectrum is generated.

Although there are several different mechanisms for relaxation, there are two main relaxation processes: longitudinal (or spin-lattice) relaxation and transverse (or spin-spin) relaxation. Longitudinal

relaxation is characterised by the time constant T_1 and relates to the time taken for the net magnetization vector, **M**, which has been perturbed away from $\mathbf{B_0}$ to return to its equilibrium value, $\mathbf{M_0}$. Transverse relaxation, characterised by the time constant T_2, is a measure of the decay of the magnetisation vector perpendicular to $\mathbf{B_0}$, after a radio frequency pulse has been applied.

2.2.1 Other NMR Interactions

Whilst the Zeeman interaction typically represents the largest contribution to nuclear energy levels (on the order of 10^8 Hz). The overall Hamilton for NMR interactions is given by:

$$\hat{H} = \hat{H}_Z + \hat{H}_{CS} + \hat{H}_{DD} + \hat{H}_J + \hat{H}_Q \tag{2.6}$$

where the remaining Hamiltonians $\hat{H}_{CS}$, $\hat{H}_{DD}$, $\hat{H}_J$, and $\hat{H}_Q$ correspond to chemical shift (shielding) (which is typically on the order of 10^3 Hz), dipolar coupling (which is also typically on the order of 10^3 Hz), indirect spin-spin (J) coupling (which is typically on the order of 10 Hz) and quadrupolar coupling (which is on the order of 10^6 Hz), respectively.

The chemical shift interaction arises from the circulation of electrons in molecular orbitals that is induced by $\mathbf{B_0}$. These circulating electrons produce small local magnetic fields ($\mathbf{B_{loc}}$) at the nucleus. The magnitude and orientation of these fields depend on bond types and the coordination environment surrounding the nucleus. The local magnetic field can have either a deshielding or shielding effect on the nucleus, leading to higher and lower resonance frequencies, respectively, as described by:

$$\omega_0 = -\gamma(\mathbf{B}_0 - \mathbf{B}_{\mathrm{loc}}) \tag{2.7}$$

Therefore, the Hamiltonian for the chemical shift interaction can be written as:

$$\hat{H}_{\mathrm{CS}} = \gamma\hbar\mathbf{I_Z}\ddot{\boldsymbol{\sigma}}\mathbf{B}_0 \tag{2.8}$$

where $\mathbf{I}_Z$ is the z-component (parallel to $\mathbf{B}_0$) of the nuclear spin angular momentum and $\ddot{\boldsymbol{\sigma}}$ is the chemical shift tensor.

Dipolar coupling is a through-space interaction between nuclear spins, where the magnetic moments of nuclei couple with each other. The Hamilton for the interaction between two spins I and S is:

$$\hat{H}_{DD} = \mathbf{I} \cdot \ddot{\mathbf{D}} \cdot \mathbf{S} \tag{2.9}$$

where the $\ddot{\mathbf{D}}$ dipolar interaction tensor, which is given by:

$$\ddot{\mathbf{D}} = hR_{\mathrm{DD}} \tag{2.10}$$

where h is the Planck constant and R_{DD} is the dipolar coupling constant:

$$R_{\mathrm{DD}} = \hbar\left(\frac{\mu_0}{4\pi}\right)\frac{1}{r^3}\gamma_1\gamma_2 \tag{2.11}$$

where μ_0 is the vacuum permeability, γ_{I} and γ_{S} the gyromagnetic ratios of the nuclei and r is internuclear distance. It is notably that R_{DD} is inversely proportional to the cube of r, meaning the dipolar

interaction is very sensitive to internuclear distance. The dipolar interaction typically leads to broadening of signals in SSNMR spectra; however, this interaction can be exploited to transfer magnetization between nuclei and to measure interatomic distance.

Indirect dipole-dipole, or *J*-coupling, is a magnetic interaction of nuclear spins with each other that occurs via electrons (through chemical bonds). This interaction is typically on the order of tens of Hz and is usually not observed in SSNMR spectra as the influence of other NMR interactions is much larger. In solution NMR, *J*-coupling is useful for differentiating nuclei in different chemical environments and to determine bonding connectivities between different chemical sites. *J*-coupling is manifested in a spectrum of nucleus *I* as a splitting of signal into $2nS + 1$ peaks, where *n* is the number of equivalent coupled nuclei with spin *S*. The relative intensities of the components of the J-coupling multiplets can be determined using Pascal's triangle.

The quadrupolar interaction is only present for nuclei with quadrupolar nuclei (i.e., those with $I > 1/2$), which have an asymmetric distribution of nuclear charge. As previously mentioned, it is significantly stronger than the other interactions in the solid state, however it less of an effect on solution NMR as the effect is diminished by molecular tumbling. The asymmetric charge distribution is described by the nuclear quadrupole moment, *Q*, and the Hamilton for the quadrupole interaction is given by:

$$\hat{H}_Q = \frac{eQ}{2I(2I-1)}\mathbf{I}\cdot\ddot{\mathbf{V}}\cdot\mathbf{I} \tag{2.12}$$

where *e* is the charge of an electron, **I** is the spin angular momentum operator and $\ddot{\mathbf{V}}$ is the electric field gradient (EFG) tensor, which is defined in its principal axis system by three components $|V_{11}| \leq |V_{22}| \leq |V_{33}|$. The EFG tensor is traceless and as such, only two parameters are needed to define the quadrupolar interaction. The first of these is nuclear quadrupolar coupling constant (C_Q) and describes the magnitude of the quadrupole interaction, the definition of which is given by:

$$C_Q = \frac{eQV_{33}}{h} \tag{2.13}$$

where *h* is the Planck constant. The second of these is the asymmetry parameter (η_Q), which is a measure of the axial symmetry of the EFG tensor and is given by:

$$\eta_Q = \frac{V_{11} - V_{22}}{V_{33}} \tag{2.14}$$

Two quadrupolar nuclei are studied in detail in this thesis: ^{23}Na and ^{2}H which are $I = 3/2$ and $I = 1$ nuclei, respectively. A schematic of the energy levels of an $I = 3/2$ nucleus is given in Figure 2-2 (a), there are four spin states and three corresponding transitions: $m_I = 1/2 \leftrightarrow m_I = -1/2$, $m_I = 1/2 \leftrightarrow m_I = 3/2$ and $m_I = -1/2 \leftrightarrow m_I = -3/2$, the first of these is the central transition (CT) and the latter two are satellite transitions (ST). If considering only the Zeeman interaction, these transitions are all separated

by the ν_0; however, the quadrupolar interaction perturbs the nuclear energy levels, which alters the energy of the transitions. The quadrupolar interaction can be split into two perturbations: first- and second-order, the Hamiltonians for which are denoted $\hat{H}_Q^{[1]}$ and $\hat{H}_Q^{[2]}$, respectively. The first-order quadrupolar interaction alters the STs, however the CT is not affected. Magic angle spinning (MAS) (*vide infra*) can be used to average first-order interactions to zero (in practise high enough spinning rates cannot always be achieved and it is common to see spinning side bands). The second order interaction alters all transitions. Second-order interactions cannot be fully averaged by MAS, but they can be reduced by increasing field strength. In SSNMR, the quadrupolar interaction has a complex orientation dependence (i.e., each orientation of the EFG tensor with respect to B_0 gives rise to a distinct frequency). This results in characteristic powder patterns which can be simulated to extract the quadrupolar interaction.[82]

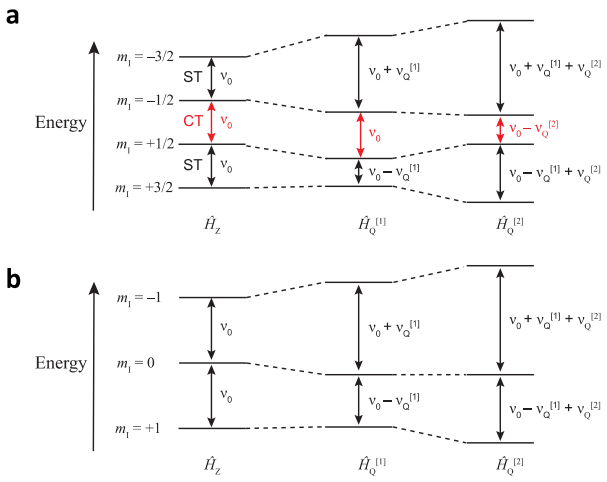

*Figure 2-2: Schematics explaining first- and second-order quadrupolar interactions for an (a) I = 3/2 (a) and (b) I = 1 nuclei adapted with permission from Reference.*72

Figure 2-2 (b) shows a similar schematic of the energy levels for an $I = 1$ nucleus (e.g., ^{2}H). There are two transitions: $m_I = 1 \leftrightarrow m_I = 0$ and $m_I = 0 \leftrightarrow m_I = -1$ (i.e., no CT), and both transitions are influenced by the first- and second-order quadrupolar interactions and are therefore have different energy spacings. Therefore, if an NMR spectrum was collected for a single crystal, two sharp peaks would be observed. In practise however, when NMR spectra are collected for powders a "Pake doublet" forms instead.[84] This consists of two overlapping powder patterns and an example is given in Figure 2-3, where there are three main features: horns, shoulder and feet are highlighted. This distinctive shape arises from the distribution of orientations of the crystallites (and hence, EFG tensors). The horns correspond largest component of the EFG tensor being perpendicular to the magnetic field. This is the most common orientation and hence the intensity is much higher. The feet correspond to the largest component of the EFG tensor parallel to the magnetic field which is less common, hence the lower intensity.

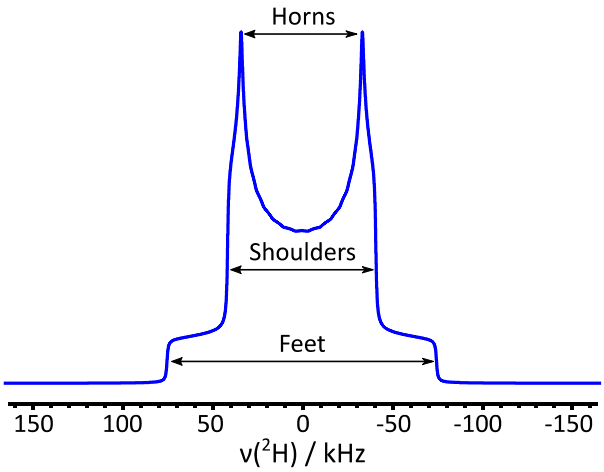

Figure 2-3: A simulated static ^2H SSNMR spectrum showing a Pake doublet with C_Q = 100 kHz and η_Q = 0.1, with the horns, shoulders and feet labelled.

2.2.2 Solid-state NMR

In solution NMR, rapid tumbling of molecules averages dipolar coupling and the quadrupolar interaction to zero and the chemical shift anisotropy (CSA) and *J*-coupling to isotropic values. Consequently, NMR spectra of liquids typically exhibit highly resolved sharp peaks (with the exception of solution NMR of quadrupolar nuclei which can result in broad peaks due to fast relaxation). For solids, such resolution is usually not observed. Indeed, the rapid tumbling does not occur and leads to peak broadening. Typically, for powders, each molecular orientation with respect to the external magnetic field gives a different resonance frequency and one will observe a broad peak (the aforementioned powder pattern). Whilst powder patterns can give information on the orientation of different molecular fragments, enabling other techniques such as NMR crystallography, the broadening results in low resolution. The spread of the signal intensity over a larger frequency range also results in lower signal-to-noise ratios. High resolution spectra can be obtained, and anisotropic interactions selectively reintroduced using magic-angle spinning (MAS) techniques, which are described in the following section.

2.2.2.1 Magic Angle Spinning

The Hamiltonians that describe first-order NMR interactions (i.e., the chemical shielding, dipolar coupling, first-order quadrupolar interaction) have the orientation dependence shown below:

$$(3\cos^2\theta - 1) \tag{2.15}$$

in this expression, θ is the angle between the largest component of the interaction tensor and B_0. Spinning the sample at an angle with respect to B_0 results in the orientation of tensor changing overtime and the average orientation is given by:

$$\langle 3cos^2\theta - 1\rangle = \frac{1}{2}(3cos^2\theta_M - 1)(3cos^2\beta - 1) \tag{2.16}$$

where θ_M is the angle between the rotation axis and B_0 and β is the angle between the largest component of the tensor and the rotation axis. By setting θ_M to the magic angle (54.74°), the right-hand side of the equation goes to 0. The quadrupolar interaction however, is only partially removed by MAS, despite the first order term interaction being averaged to zero. This is because the second order interaction contains an additional orientational dependence which is not removed by MAS.

To completely average these interactions, the sample needs to be spun at a rate greater than the largest anisotropy. In practise, however this is not always possible and if the sample is spun at a speed lower than the largest anisotropy, spinning sidebands are observed. These are sharp lines in the spectra that are separated by from the isotropic peak by integer multiples of the spinning speed and mirror the shape of the powder pattern. These sidebands can make identifying the isotropic peaks, especially if multiple environments are present. However, by collecting spectra at different spinning speeds the sidebands can easily be identified.

To perform MAS experiments, the sample is loaded into an NMR rotor. This is hollow cylinder, mounted with a turbine, or drive, cap that enables spinning when compressed gas is applied. Typically, these rotors are made from zirconia as it is chemically unreactive and has a low thermal conductivity. As the rotor caps provide a close fit, it can be assumed that the rotor is air sensitive. Chemical shift referencing is performed by collecting a spectrum of a compound with a known chemical shift (a secondary refence) in a separate rotor.

2.2.3 Hahn Echo

The most basic NMR experiment is a single pulse experiment, the pulse sequence diagram of which is given in Figure 2-4 (a). In this experiment, a 90° pulse is applied, which tips magnetization from the *z*-axis (which aligns with the external magnetic field, B_0) to the *x*-*y* plane. A spectrum is then immediately collected. In practice, a small delay called the deadtime is inserted after the pulse so that the pulse has fully dissipated in the coil before the receiver is turned on. However, in the case of broad patterns or rapidly decaying signals, a significant portion of the signal is lost during the dead time, resulting in severe line shape distortions. Therefore, the Hahn echo[85] pulse sequence is the often used (the pulse sequence diagram of which is given in Figure 2-4 (b)) as it can resolve the issues associated with the dead time. Like the singe pulse experiment, a 90° pulse tips magnetization from the *z*-axis to the *x*-*y* plane. After a time τ, due to inhomogeneities in the local magnetic field or differences in resonance frequencies caused by anisotropic NMR interactions, the spins precess at different rates in the *x*-*y* plane, causing a fanning out of magnetization. By applying a 180° pulse, the magnetization is refocused and after another time τ, an echo is formed. Typically τ is an integer multiple of the rotor period, if so the experiment is described as rotor-synchronised.

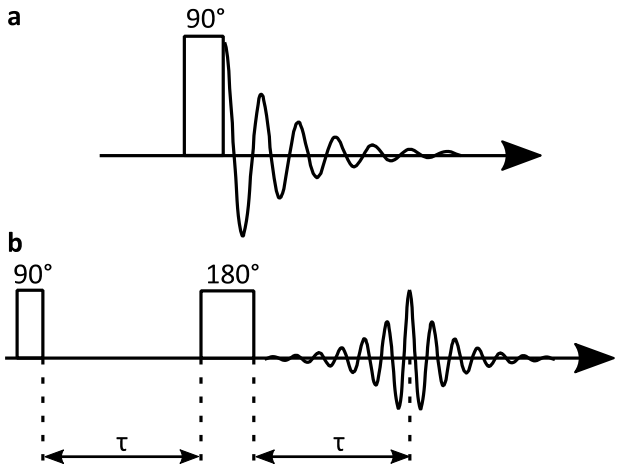

Figure 2-4: Pulse sequences for (a) single pulse and (b) Hahn echo NMR experiments.

Whilst this pulse sequence is generally very useful, there are some situations where it is not applicable. For example, the quasi-metallic Na species that have pooled in the pores of hard carbon, have a very fast T_2 relaxation time constant, which means the signal decays completely before the refocusing pulse is applied. Hence, a single pulse NMR experiment has to be used when studying quasi-metallic Na in the pores of hard carbon.

2.2.4 Cross Polarization

Due to the combination of low gyromagnetic ratio and low abundance, some nuclei (such as ^{13}C and ^{15}N) have an intrinsic low sensitivity, which makes them difficult to study. One way around this is to use a cross polarization (CP) experiment, where polarization from abundant nuclei like ^{1}H is transferred to less abundant nuclei, denoted as X. As the transfer of polarization occurs via dipolar coupling, which is a through-space interaction, the transfer does not require a chemical bond between the two atoms. Furthermore, as the dipole interaction is inversely proportional to the cube of internuclear distance, CP only works over short distances. This can be used to help peak assignments as signals are only present for atoms that are close to each other, with limited motion relative to each other. The theoretical maximum enhancement for the CP experiment is given by the ratio of the two gyromagnetic ratios: $\gamma^{\mathrm{H}}/\gamma^{\mathrm{X}}$.

The pulse sequence diagram for CP is given in Figure 2-5. First, a 90° pulse is applied to ^{1}H, a second pulse is then applied simultaneously on both ^{1}H and X channels which spin-locks (i.e. keeps ^{1}H magnetization in the transverse plane) and transfers magnetization to X. Once magnetization has been built up, the signal can be acquired, under ^{1}H-X heteronuclear decoupling (where the sample is irradiated with at a frequency to limit ^{1}H-^{1}H dipole interactions). For polarization transfer to occur, the *Hartmann-Hahn* condition[86] must be fulfilled, which is given by:

$$\gamma^{\mathrm{H}} B_1^{\mathrm{H}} - \gamma^{\mathrm{X}} B_1^{\mathrm{X}} = n\omega_r \qquad (2.17)$$

where B_1 is the field associated with a pulse, $n = 0, \pm1, \pm2, \ldots$ and ω_r is the (angular) spinning frequency. In practise, as this interaction occurs via dipolar coupling, it is important that spectra are not collected at high MAS spinning speeds as this would minimise the interaction and CP signal would not be observed.

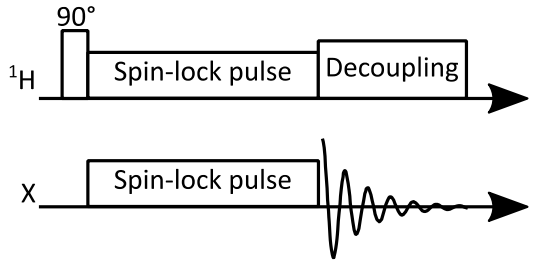

Figure 2-5: A pulse sequence for a ^{1}H-X CP experiment

2.3 X-ray Photoelectron Spectroscopy

X-ray photoelectron spectroscopy (XPS) is a highly surface sensitive technique. It can be used to both qualitatively determine what elements are present and the chemical state they are in, as well as quantitatively to determine the proportions of elements and oxidation states present. The technique was originally developed by Siegbahn *et al.*,[87,88] who was awarded the 1981 Nobel Prize in physics for his contribution to the development of high-resolution electron spectroscopy.

2.3.1 Photoelectric Effect

XPS is based on the photoelectric effect, which states that when a material is irradiated with photons, electrons are emitted (which are now referred to as photoelectrons). Whilst this effect was first observed in by Hertz in 1887,[89] it was not until Einstein's work in 1905[90] that the effect was understood, and in recognition of this work on the photoelectric effect that Einstein was awarded the 1921 Nobel Prize in physics. The kinetic energy (E_k) of these photoelectrons is given by:

$$E_k = h\nu - E_b - \phi \tag{2.18}$$

where $h\nu$ is the photon energy, E_b is the binding energy of the electron and φ is the work function, which is the minimal energy needed to remove an electron from a solid to a point in the vacuum immediately outside the solid surface. Given that h, ν and φ are known, E_b can be determined for the photoelectrons directly from E_k. As E_b is different for each element (and each electronic orbital), the elemental composition can be easily determined for each sample. In addition, the oxidation state of the atom varies the binding energy of the photoelectrons, as a more positive oxidation state will make it harder to remove electrons, hence higher oxidation states will correspond to higher values of E_b. It is worth noting that not all electrons have the same probability of being excited (this probability is expressed as the photoionization cross section) and consequently, the areas of different peaks cannot be directly compared. To account for these differences, each orbital has its own sensitivity factor which

enables the area of each peak to correspond to the number of electrons present. One of the most common types are Scofield[91] sensitivity factors.

2.3.2 Surface Specificity

Whilst X-rays are able to penetrate quite far into the bulk of a material (typically on the order of μm), photoelectrons are not able to travel that far without interacting with other atoms and losing energy, this is referred to as inelastic scattering. The probability of a photoelectron travelling a certain distance (*d*) before being inelastically scattered is given by the exponential function given by:

$$P(d) = e^{-\frac{d}{\lambda}} \tag{2.19}$$

where λ is the inelastic mean free path length. This is not a constant and varies for different elements and different orbitals within each element, as expressed by a so-called universal curve.[92] Overall, the result is that most detected photoelectrons will come from the outermost 10 nm of the material, with the majority coming from an even smaller distance. This corresponds to the outermost atomic layers, hence XPS is a surface sensitive technique. It is for this reason that XPS is performed under ultra-high vacuum (UHV), as if a normal atmosphere were present, it would interact with the photoelectrons and cause them to be inelastically scattered.

2.3.3 Spin-orbit Coupling

Table 2-1: A table showing how j varies with different values of l and peak area ratios.

Orbital	*l*	*j*	Peak Area Ratio
s	0	1/2	n/a
p	1	1/2, 3/2	1:2
d	2	3/2, 5/2	2:3
f	3	5/2, 7/2	3:4

Spin-orbit coupling describes the interaction between an unpaired electron (with a spin angular quantum number, $s = \pm 1/2$) and its electronic orbital (with an orbital angular momentum quantum number, $l = 0, 1, 2, 3$, for *s*-, *p*-, *d*- and *f*-orbitals, respectively). These quantum numbers combine to give the total angular momentum quantum number, $j = |l + s|$, of the electron. Table 2-1 shows the possible values of *j* for each orbital. As *j* cannot be negative for *s* orbitals, there is only one value of *j* (1/2), therefore these signals consist of singlet peaks. The *p*, *d* and *f* orbitals all have two values of *j* and so these signals consist of doublet peaks. However, sometimes the energy difference between the doublet peaks is too small (< 0.5 eV) to separate with laboratory-based instruments and they appear as singlets. The peak area ratios for the doublets are then defined by the degeneracy of the spin states ($2j + 1$), hence *p* orbitals have an area ratio of 1:2, *d*-doublets have an area ratio of 2:3 and *f*-doublets have an area ratio of 3:4. The peaks for each in XPS spectra are therefore labelled as *nlj*, where *n* is the principal quantum number of the electron (such that $n = 1, 2, 3\ldots$). In practise, the letter *s*, *p*, *d* and *f* are used instead of the numerical value of *l* and the "/2" of *j* is sometimes omitted.

2.4 Thermogravimetric Analysis

Thermogravimetric analysis (TGA) is a technique where the mass of a sample is measured as a function of temperature. This allows information about the physical (e.g., phase transitions or physisorption) or chemical (such as thermal decomposition or oxidation and reduction reactions with a gas) properties of a material to be analysed.[93] For the TGA analysis in this thesis, a sample is heated under an inert atmosphere (N_2) and the mass decreases as a function of temperature are displayed as a TGA curve, where each mass loss can be assigned to certain properties of the material being analysed.

2.5 X-ray Diffraction

X-ray diffraction (XRD) is a commonly used analysis technique for studying crystals. It provides information about the geometry and size of repeating unit cells in a material. During XRD, X-rays are scattered by the electrons in the material. This is different to other scattering techniques such as neutron scattering where neutrons are scattered by the nuclei rather than electrons.[94] Neutron scattering can be useful as the neutron scattering length is not proportional to the atomic number and varies more randomly, meaning elements adjacent to each other in the periodic table are easier to differentiate and lighter elements are easier to observe. However, neutron sources have a low flux compared to X-rays and cannot be performed on the lab scale, unlike XRD.

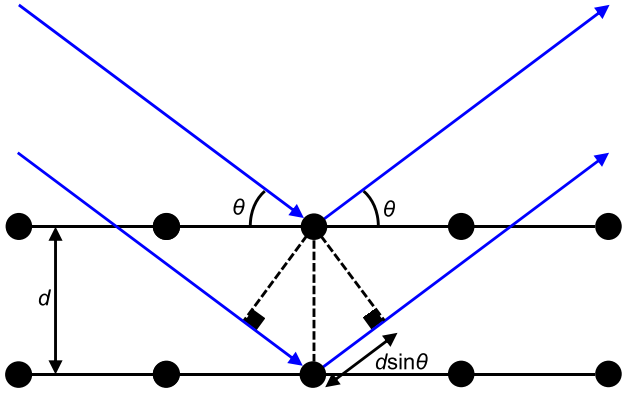

Figure 2-6: A schematic representing that the difference between the incident and diffracted beams have a path difference of 2d sinθ, which gives Bragg's law.

During an XRD experiment, an X-ray beam is radiated upon a sample, the X-rays can either be transmitted or scattered by the electrons in the material. The diffracted beams can then interfere with each other, either constructively or destructively. If destructive interference occurs the X-rays cancel each other out, but those that combine constructively combine can be observed. In order for constructive interference to occur, X-rays must come from angles determined from Bragg's law:[95]

$$n\lambda = 2d \sin\theta \tag{2.20}$$

where n is an integer, λ is the wavelength of the X-rays, d is the spacing between the diffraction planes and θ is the incidence angle, this is demonstrated in Figure 2-6.

The resulting diffraction pattern consists of several different peaks, which correspond to different planes in the material, which are defined as (*h k l*), where *h*, *k* and *l* are Miller indices which describe the orientation of the plane within the unit cell. The position of these peaks is determined by the inter-planar spacing for series of planes, with smaller diffraction angles corresponding to a larger interplanar spacing, due to Bragg's law. Peak intensities are determined the position of other atoms in a unit cell, this is because these other atoms also diffract X-rays, and the intensity of a single peak is superposition of all the constructive and destructive contributions.

Peak width depends on two factors: crystallite size and strain. Smaller crystallites generally lead to broader peaks as these crystallites are slightly out of alignment, meaning X-rays will be scattered with slightly different angles. Strain can also influence peak width, this is because compressed lattices decrease lattice size, which in turn increases interplanar spacing and decreases the diffraction angle. The opposite occurs for stretched lattices, and a combination of both effects will lead to peak broadening. Based on these factors a significant amount of information can be obtained for crystalline materials. However for amorphous materials or those that contain a significant amount of disorder, the diffraction peaks will become broader and have a lower intensity and become much harder to observe.

2.5.1 Powder X-ray Diffraction

To determine an unknown structure of a crystalline material XRD usually has to be performed on a single crystal. However, preparing a single crystal can be challenging, especially for battery samples. Therefore, if a single crystal cannot be produced or a bulk analysis is required, powder X-ray diffraction (PXRD) can be performed instead. During PXRD, many different crystallites are present, which means many different planes fulfil the Bragg condition simultaneously and the position of Bragg peaks in the PXRD pattern may easily determined. Whilst determining an unknown structure from PXRD is possible, it is difficult and time consuming. However, if the structure is known information about the unit cells can be easily determined. Additionally techniques such as Rietveld[96] refinements can be used to refine the structure and give a better understanding of the material.

In this work, electrodes were compared using XRD after electrochemical cycling. Due to the air sensitive nature of the samples being studied, an air sensitive sample holder was used. To allow the transmittance of X-rays, the air sensitive sample holder has a window of Kapton film. Kapton is a polyimide, which allows a high transmittance of X-rays. This means it has little effect on the resulting diffraction patterns.

3 Investigating Solvent Co-intercalation into Carbon Anodes for Sodium Ion Batteries

3.1 Abstract

NIBs are seen as being a potentially cheaper and more environmentally friendly way of storing energy, when compared to current LIBs, especially for large scale applications such as grid storage of renewable energy. Whilst a lot of the technology developed for LIBs can be transferred to NIBs, Na does not normally intercalate into graphite (the anode of choice for commercial LIBs) and disordered hard carbons are typically used as anodes instead. However, it is known that if diglyme is used as a solvent for the electrolyte, a good electrochemical performance can be achieved as diglyme co-intercalates with Na^+ ions into graphite.[42] Herein we investigate solvent co-intercalation into graphite at multiple states of charge using solid state nuclear magnetic resonance spectroscopy (SSNMR) and thermogravimetric analysis (TGA). Furthermore, we provide evidence from these techniques that a similar co-intercalation process also occurs for hard carbon, albeit to a lesser extent than in graphite.

3.2 Introduction

For commercial LIBs, the anode of choice is graphite due to its low cost, high natural abundance and good electrochemical performance. Under normal circumstances, Na^+ does not intercalate into graphite. It might be assumed that this is due to the larger ionic radius of Na^+, compared to that of Li^+, meaning more energy is required to pull apart the graphene sheets in graphite upon intercalation of Na^+. However, it has been shown that K^+ and even larger alkali metal ions can intercalate into graphite.[97] Moriwake *et al.*[23] showed that intercalation becomes more favourable for elements further down group one of the periodic table as ionic interactions between the cations and graphite increase in strength. Li is the exception to this rule as Li-C bonds have a significant covalent character, which stabilises the Li intercalation compounds. Unfortunately for NIBs, Na intercalation into graphite is not stabilised by ionic or covalent interactions and is therefore energetically unfavourable.

It is therefore evident that a different material is required for the anode of NIBs. Currently, the material of choice is a disordered form of carbon called hard carbon, the structure of which consists of randomly arranged turbostratic graphitic domains with large interlayer spacings.[24] Na storage is provided by several environments within hard carbon, such as nanopores, defects, and the spacings between carbon sheets. When Na is electrochemically intercalated into hard carbon, two regions are observed in the voltage profile, a sloping region above ~ 0.1 V and a plateau between 0.1 and 0 V. Traditionally, Na intercalation into hard carbon is often described by the "house of cards" model,[27,98] where the sloping region corresponds to intercalation of Na between the carbon layers, and the plateau corresponds to Na pooling into the pores forming a quasi-metallic species.[31] However more recent studies have suggested that the structure of hard carbon consists of curved carbons sheets, where the amount of defects relate to the degree of curvature.[33,39] The slope therefore, corresponds to Na^+ ions that

are being stored at defects, within interlayers and on pore surfaces, with the plateau still corresponding to pore filling

Recently, it has been reported by Jache *et al.*[42] and Kim *et al.*[99] that a good electrochemical performance can be achieved for Na intercalation into graphite when diglyme is used as an electrolyte solvent, achieving a specific capacity of ~100 mAh g^{-1}. It is thought that diglyme co-intercalates with Na^+ ions into graphite and that this intercalation is stabilised by van der Waals interactions between diglyme and the graphene sheets.[100] It has been determined through a combination of neutron scattering and empirical potential structure refinement, that each Na^+ ion is coordinated to two diglyme molecules to form the complex $Na^+(diglyme)_2$.[43] Subsequently, other glymes and crown ethers[44, 45] have also been shown to co-intercalate with Na into graphite.

Evidence for co-intercalation has been provided by several techniques. Firstly, X-ray diffraction (XRD)[42] has been used to show that graphite expands on sodiation with diglyme. Solid-state NMR (SSNMR) backs this up as well as providing evidence for the limited mobility of intercalated diglyme molecules. Further structural information has also been provided by SSNMR, such as the distance complexes are from the graphene layers, and how these are larger than the Li equivalents enabling higher mobility of intercalated Na-diglyme complexes, compared to Li-diglyme complexes.[101] Details about the dynamics of diglyme in graphite were provided by ^2H SSNMR,[102] where it was found that diglyme is weakly coordinated to Na^+, enabling molecular rotation of diglyme around the central Na–O bond. It has also been shown that ether-based electrolytes enable hard carbon anodes to be used at higher rates, without the loss in plateau capacity that is observed for carbonate-based electrolytes.[103] It was suggested that is because ether-based electrolytes reduce electrochemical polarization, but potentially this could be because the solvent molecules are also co-intercalating into hard carbon.

Herein, we investigate the co-intercalation of diglyme with Na into graphite and a commercial hard carbon (Carbotron P(J), Kureha Corporation) utilizing a combination of SSNMR and thermogravimetric analysis (TGA). Electrochemical measurements show that a graphite electrode with a diglyme based electrolyte has an initial capacity of 170 mAh g^{-1}, compared to 10 mAh g^{-1} for a EC:DMC electrolyte. The later of these is likely due to sodiation of the carbon black additive or the formation of the SEI. Whereas for hard carbon electrodes, both diglyme and EC:DMC electrolytes gave similar initial capacities of approximately 340 mAh g^{-1}, with both electrolytes having similar charge-discharge curves (i.e., consisting of sloping and plateau regions). By comparing SSNMR data of graphite and hard carbon electrodes sodiated to different states of charge with diglyme based electrolytes, we provide evidence that diglyme co-intercalates with Na into hard carbon. While less diglyme co-intercalates into hard carbon, it appears to be more mobile than in graphite. This could explain the high-rate capability of hard carbons with diglyme electrolytes, compared to carbonate electrolytes.

3.3 Experimental

3.3.1 Sample Preparation

Hard carbon electrodes were prepared by mixing Carbotron P(J) (Kureha Corporation, 90 wt%) with poly(vinylidene fluoride-co-hexafluoropropylene) (PVDF-HFP, Kynar, 5 wt%) and Super P (Timcal, 5 wt%) into a slurry with *N*-methyl-2-pyrrolidone (NMP, Sigma Aldrich) as a solvent. The resulting slurry was cast on copper foil and dried at 120 °C *in vacuo*. Graphite electrodes were prepared in a similar way by mixing graphite (BTR AGP-8, 92 wt%), poly(vinylidene fluoride (PVDF, Kynar, 6 wt %) and Super P (Timcal, 2 wt%).

Coin cells were prepared from these electrodes using 2032 coin cell components in an Ar glovebox (O_2 < 1 ppm, H_2O < 1 ppm). Na metal (Sigma-Aldrich) was used as a counter electrode; 150 μL of 1 M $NaPF_6$ (Acros Organics) in diglyme (Sigma-Aldrich, 99.5 %, which had been distilled via a vacuum system and stored over 4 Å molecular sieves under Ar until use) was used as an electrolyte and borosilicate glass fibre (Whatman, GF/B) was used as the separator. $NaPF_6$ was dried overnight at 120 °C *in vacuo* prior to use.

The half-cells were sodiated galvanostatically to the desired voltage, using either a Biologic MPG2 or a Lahne CT2001A battery cycler at a rate of *C*/20. For hard carbon this corresponds to a theoretical capacity of 300 mAh g^{-1} in 20 hours based on the mass of hard carbon in the anode and for graphite, this corresponds to a theoretical capacity of 100 mAh g^{-1} in 20 hours based on the mass of graphite in the electrode.

3.3.2 SSNMR Experiments

SSNMR experiments were performed on electrodes that had been cycled in coin cells. After cycling, the cells were transferred to an Ar glovebox (H_2O < 1 ppm, O_2 < 1 ppm) where they were opened, the electrodes were removed, and the carbon films scraped off the current collectors. Most electrodes were not washed or dried prior to analysis. For those samples that were vacuum dried, the electrodes were dried under vacuum in a glovebox antechamber for 15 minutes, and those that were washed were done so with three 1 mL aliquots of dimethyl carbonate (DMC).

All SSNMR spectra were collected on a Bruker Advance III HD console, equipped with a 11.7 T Bruker widebore magnet. Experiments were conducted using either a 2.5 mm or 1.3 mm Bruker double-channel MAS probe. A single pulse experiment was used for ^{23}Na and rotor synchronised Hahn echo experiments were used for ^{1}H, ^{13}C and ^{19}F. ^{1}H-^{13}C and ^{19}F-^{23}Na cross polarization (CP) experiments were performed with either (^{1}H) or (^{19}F) decoupling. The chemical shifts were referenced to adamantane (s) ($\delta_{iso}(^{1}H)$ = 1.85 ppm), glycine-1-^{13}C (s)($\delta_{iso}(^{13}C)$ = 176 ppm), LiF (s) ($\delta_{iso}(^{19}F)$ = –204 ppm) or NaCl (s) ($\delta_{iso}(^{23}Na)$ = 7.2 ppm). Further experimental details are given in Table A1. Simulations for the experimental spectra was carried out using the SOlid Lineshape Analysis (SOLA) tool within TopSpin.

3.3.3 TGA Experiments

Samples for TGA were prepared in a similar way to those for SSNMR. Experiments were performed on a Mettler Toledo STARe System TGA/DSC 2 LF/110, under flowing N_2 at a heating rate of 5 °C min^{-1} up to 500 °C.

3.3.4 XRD Experiments

Samples for XRD were also prepared in a similar manner, except that the electrodes were not scraped off the current collectors and were directly transferred to the diffractometer in an air-sensitive sample holder. Diffraction patterns were collected on a Panalytical Empyrean diffractometer using CuKα radiation (λ = 154.06 pm).

3.4 Results

3.4.1 Co-intercalation into Graphite

Sodiaton of a graphite electrode in a carbonate-based electrolyte (i.e., 1 M $NaPF_6$ in 1:1 v/v% ethylene carbonate and dimethyl carbonate (EC:DMC)) resulted in a very low specific capacity of approximately 10 mAh g^{-1} (Figure 3-1 (a), blue trace). This indicates that only a small amount of Na intercalates into graphite and a significant amount of this capacity is likely due to sodiation of the carbon black (Super P) additive or the formation of the SEI.[98] When a graphite electrode was sodiated with a 1 M $NaPF_6$ in diglyme electrolyte (Figure 3-1 (a), red trace), a specific capacity of 170 mAh g^{-1} was achieved for the first sodiation, indicating appreciable intercalation of Na into graphite. The voltage profile consists of three distinct regions, a sloping region from 1.0 V to 0.6 V, a plateau at 0.6 V, and a sloping region from 0.6 V to just above 0 V. These regions correspond to a staged insertion mechanism, previously characterised by H. Kim *et al.*[99]. In this mechanism, the graphite intercalation stages are denoted as stage n, where n is the number of carbon layers that separate the Na layers. The first step (denoted A in Figure 3-1) from 1.0 V to 0.7 V corresponds to graphite undergoing a one-phase-like transition where many different n > 3 stages are present, however by 0.7 V stage 3 has completely formed. A biphasic reaction begins to occur where stage 2 forms at the expense of stage 3 (B), such that by 0.6 V only stage 2 is present. The plateau then corresponds to the transition from stage 2 to stage 1 (C) and the final slope to just above 0 V corresponds to filling of stage 1 (D). This process is illustrated in Figure 3-1 (b).

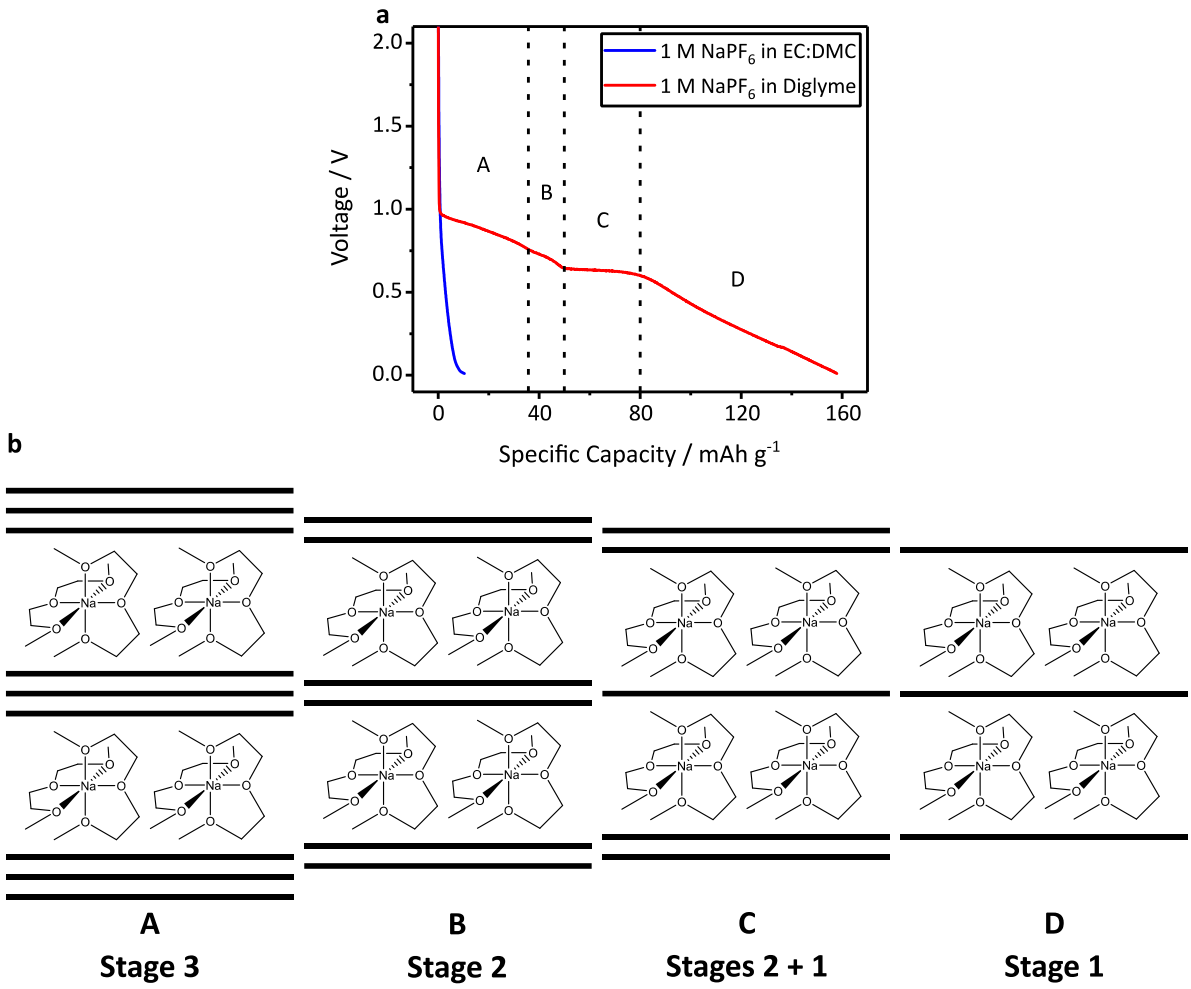

Figure 3-1: (a) Voltage profiles for the first sodiations of graphite half-cells discharged to 10 mV at rates corresponding to C/20 with electrolytes consisting of 1 M $NaPF_6$ in EC:DMC (blue trace) and 1 M $NaPF_6$ in diglyme (red trace). The four transitions of the staged insertion mechanism for graphite sodiated with 1 M $NaPF_6$ in diglyme are denoted A-D. (b) A schematic demonstrating the staged insertion mechanism.

To provide evidence for co-intercalation, TGA was performed on a graphite electrode fully sodiated to 10 mV that was not vacuum dried (Figure 3-2, red trace). To perform TGA experiments, the graphite electrodes were transferred to the TGA in an air sensitive manner. However, they were briefly exposed to air when (for less than on minute) loading. There are two main features in the TGA curve; a large mass loss (~55 %) below 110 °C, and a smaller mass loss (~5 %) at around 250 °C. Guan *et al.*[106] observed similar behaviour for graphite sodiated with monoglyme and assigned the features to surface adsorbed and co-intercalated monoglyme, respectively. A separate graphite electrode was dried under vacuum for 15 minutes (Figure 3-2, blue trace) and TGA shows a similar lineshape, but the first mass loss below 110 °C now corresponds to a slightly smaller mass loss (45 %). This indicates that the first mass loss is not entirely surface adsorbed diglyme and can be partially assigned to co-intercalated diglyme. The mass loss at 250 °C is probably due to salt decomposition or reactions of the surface groups of graphite.

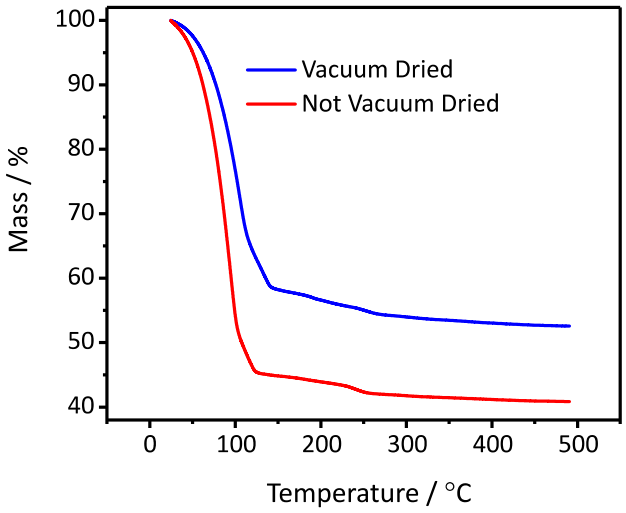

Figure 3-2: TGA curves for fully sodiated graphite electrodes, both vacuum dried (blue trace) and not dried under vacuum (red trace).

The ^{13}C SSNMR spectrum of a graphite electrode fully sodiated to 10 mV (Figure 3-3 (a), blue trace) has sharp peaks at 123 ppm and slightly broader peaks at 73 ppm and 62 ppm. A chemical shift of 123 ppm is in the range expected for sp^2 hybridised carbons and this peak is assigned to carbon atoms in the graphite lattice. However, pristine graphite has a very high orientationally dependent diamagnetic susceptibility along its c-axis (i.e. a measure of how well the material repels a magnetic field). This diamagnetism alters the chemical shift of individual carbon atoms. When an NMR spectrum is collected for graphite powder a broad range of orientations with respect to the magnetic field are present, this results in a broad range of chemical shifts for carbon atoms and a very broad ^{13}C signal for graphite.[107] An expansion along the c-axis due to the co-intercalation of Na-diglyme complexes reduces the interactions between the carbon sheets. This reduces the diamagnetic susceptibility along the c-axis, which means the shift of individual carbon atoms is not influenced by diamagnetic effects and a sharper and narrower graphite signal is observed. Further evidence of this expansion is provided by XRD where an expansion of approximately 345 % is observed on the sodiation of graphite (Figure 3-3 (b)). The two signals at 73 ppm and 62 ppm correspond to the methylene and terminal methyl groups of diglyme, respectively. These signals are relatively broad and resolved $^1J(^1H\text{-}^{13}C)$-couplings are not observed, suggesting that diglyme molecules are in relatively constrained environments, consistent with co-intercalated diglyme. To confirm that these signals are not due to surface adsorbed free diglyme, a ^{13}C SSNMR spectrum was collected for a fully sodiated graphite electrode that was dried under vacuum (Figure 3-3 (a), red trace), which shows these signals persist after vacuum drying and therefore result from co-intercalated diglyme.

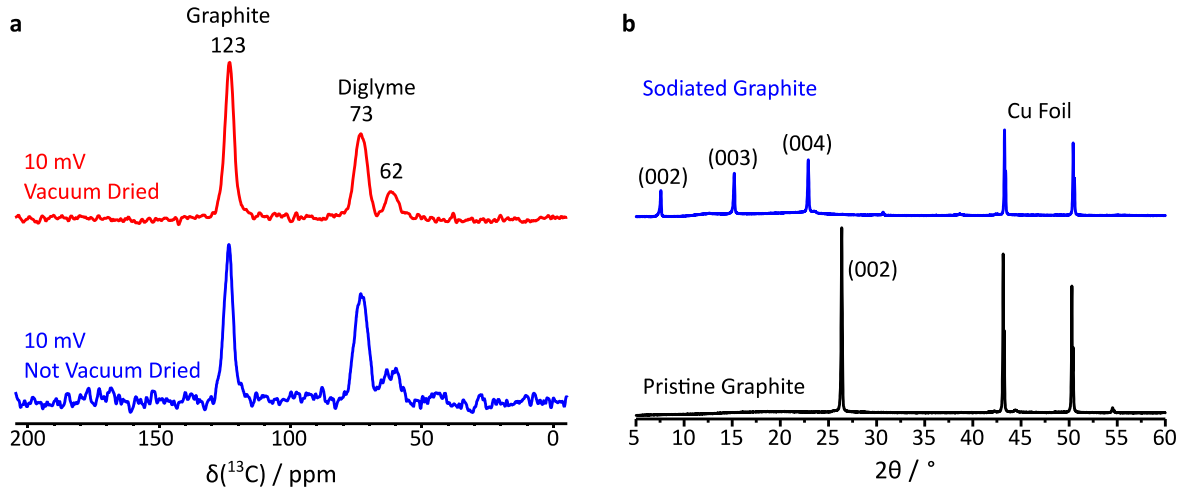

Figure 3-3: (a) ^{13}C MAS SSNMR spectra of graphite electrodes fully sodiated to 10 mV with a 1 M $NaPF_6$ in diglyme electrolyte, not vacuum dried (red trace) and vacuum dried (blue trace), both collected at a MAS speed of 20 kHz.(b) PXRD patterns collected for pristine (black trace) and fully sodiated (blue trace) graphite electrodes.

The ^{23}Na SSNMR spectrum collected for the fully sodiated graphite electrode, dried under vacuum (Figure 3-4 (a), red trace) shows three overlapping peaks at 7 ppm, –4 ppm and –14 ppm. The peak at 7 ppm is consistent with NaF (Figure 3-4 (a), blue trace), a common SEI component and is supported by a ^{19}F SSNMR spectrum (Figure 3-4 (b)) which shows peaks at –73 ppm and –223 ppm, which are assigned to PF_6^- and NaF, respectively. If a higher magic angle spinning speed of 20 kHz is used, the peaks at –4 ppm and –14 ppm coalesce to give a single peak (Figure 3-4 (c)). This suggests that these environments are related and that they are able to undergo chemical exchange, probably induced by the increased frictional heating at higher spinning rates. This process is reversible with the peaks at –4 ppm and –14 ppm returning when the spinning speed is reduced back to 10 kHz. A ^{1}H-^{23}Na cross polarization (CP) spectrum (Figure 3-4 (a), green trace) shows a sharp peak at –14 ppm and a weaker, broad signal at 7 ppm. As the former peak is at a higher chemical shift than pure $NaPF_6$ (–20 ppm) and CP experiments require ^{1}H and ^{23}Na environments to be in close proximity, with limited motion relative to each other, the peak at –14 ppm is assigned to surface adsorbed Na-diglyme complexes, possibly bound to PF_6^-, and the peak at 6 ppm could be due to nano-crystalline NaF with adsorbed H-containing species. The remaining signal at –4 ppm is assigned to co-intercalated Na-diglyme complexes, in agreement with the results previously reported by Leifer *et al.*.[101] The absence of a ^{1}H-^{23}Na CP signal for this environment is likely due to the high mobility of the intercalated species. Furthermore, the negative chemical shift of Na-diglyme complexes is similar to what has previously been reported for similar Na-solvent complexes, such as a Na-crown ether.[108]

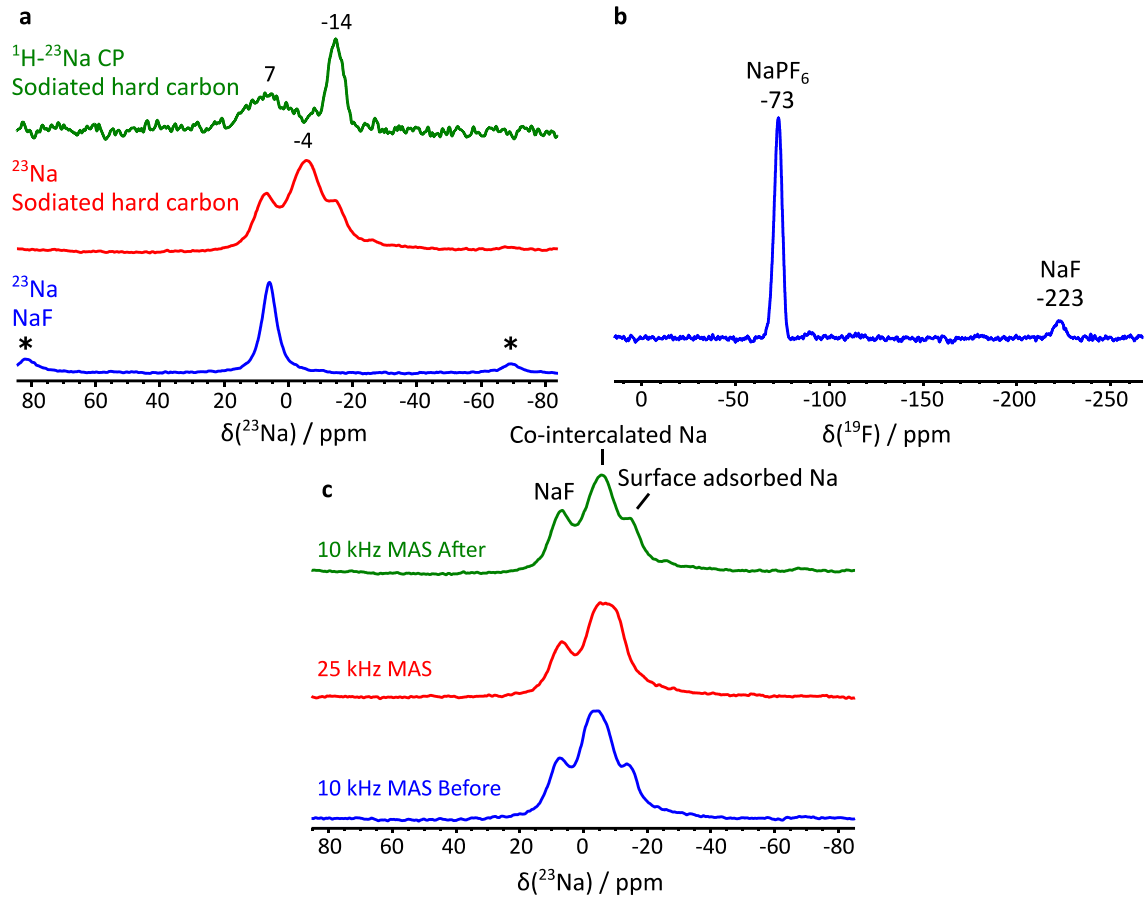

Figure 3-4: (a) ^{23}Na SSNMR spectra of NaF (blue trace), ^{23}Na (red trace) and ^{1}H-^{23}Na CP (green trace) for a graphite electrode fully sodiated to 10 mV with a 1 M $NaPF_6$ in diglyme electrolyte, dried under vacuum. All spectra were collected at a MAS speed of 10 kHz and a contact time of 1000 μs was used for the CP experiment and spinning side bands are denoted by asterisks. (b) A ^{19}F MAS SSNMR spectrum of a graphite electrode fully sodiated to 10 mV with a 1 M $NaPF_6$ in diglyme electrolyte, dried under vacuum. Collected at a MAS speed of 20 kHz. (c) ^{23}Na MAS SSNMR spectra of a graphite electrode fully sodiated to 10 mV with a 1 M $NaPF_6$ in diglyme electrolyte, dried under vaccum. Colleceted at MAS speeds of 10 kHz MAS (blue trace), 20 kHz MAS (red trace) and 10 kHz MAS after spinning at 10 kHz (green trace).

To confirm these assignments, a ^{23}Na SSNMR spectrum was also collected for a fully sodiated graphite electrode, that was washed with DMC and dried under vacuum (Figure 3-5 (a)). This spectrum consists of two peaks at 7 ppm and –4 ppm, with the notable absence of a peak at –14 ppm, this provides further evidence that the peak at –4 ppm corresponds to co-intercalated Na and the peak at –14 ppm corresponds surface adsorbed Na-diglyme, solvated by diglyme, that can be removed by washing. Additionally, a ^{23}Na spectrum was also collected for a sample of $NaPF_6$, to which a small amount of diglyme had been added (Figure 3-5 (b), blue trace). This spectrum is dominated by a peak at –20 ppm, at the same chemical shift position unsolvated $NaPF_6$. However, there are additional signals in the spectrum. Those close to –16 ppm can be enhanced with a ^{1}H-^{23}Na CP experiment (Figure 3-5 (b), green trace). Together these experiments provide further evidence that the peak at –14 ppm corresponds to surface adsorbed $NaPF_6$ solvated by diglyme and therefore that the peak at –4 ppm is co-intercalated Na-diglyme.

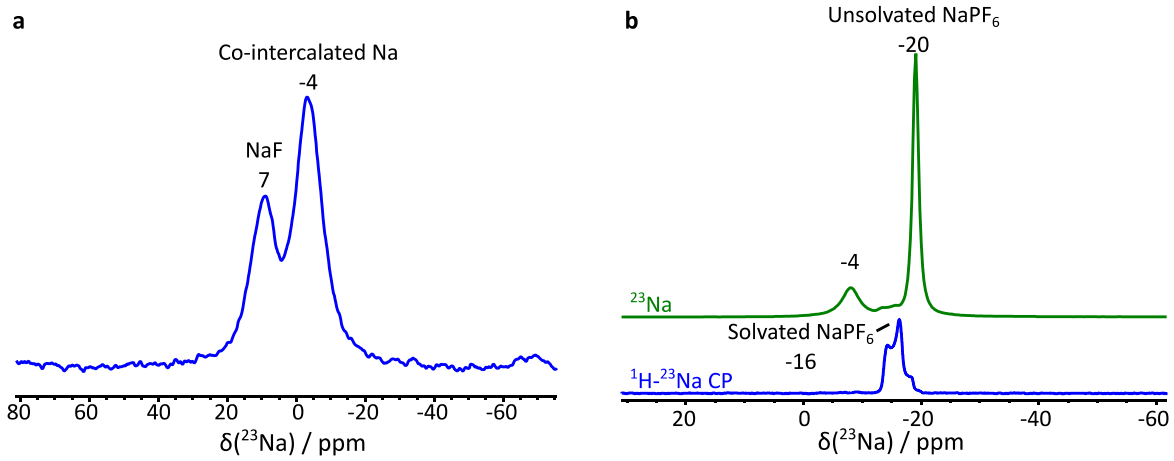

Figure 3-5: (a) A ^{23}Na MAS SSNMR spectrum of a graphite electrode, fully sodiated to 10 mV with a 1 M $NaPF_6$ in diglyme electrolyte, washed with DMC and dried under vacuum. Collected at a MAS speed of 10 kHz. (b) ^{23}Na (green trace) and ^{1}H-^{23}Na CP (blue trace) MAS SSNMR spectra of $NaPF_6$ mixed with diglyme. Both spectra were collected at 10 kHz and the CP experiment had a contact time of 10000 μs.

A ^{13}C SSNMR spectrum was also collected for a graphite electrode after one full discharge-charge cycle desodiated to 2 V (Figure 3-6 (a)). This spectrum shows a graphitic signal at 123 ppm and signals for diglyme at 73 pm and 60 ppm which are similar to those observed in the spectrum of sodiated graphite. The graphite peak is lower in intensity and broader, indicating an increase in the magnetic susceptibility, which is expected for desodiation and concomitant contraction of the graphite lattice. Although the signal has not broadened to the extent expected for pristine graphite, this suggests that some graphitic particles do not fully desodiate, which could be due to co-intercalated diglyme becoming trapped in graphite. Additionally, the diglyme signals remain, albeit with a lower intensity, which further suggests that not all the co-intercalated diglyme is removed. The ^{23}Na SSNMR spectrum for the desodiated graphite (Figure 3-6 (b)) consists of overlapping signals at 7 and –7 ppm. The peak at 7 ppm has the largest intensity and it provides further evidence for the assignment to NaF, an SEI component that is not removed on desodiation. The peak at –7 ppm is assigned to surface adsorbed Na-diglyme, which is also not removed upon desodiation. However, it is possible that this peak could also be partially due to a small amount of residual co-intercalated Na.

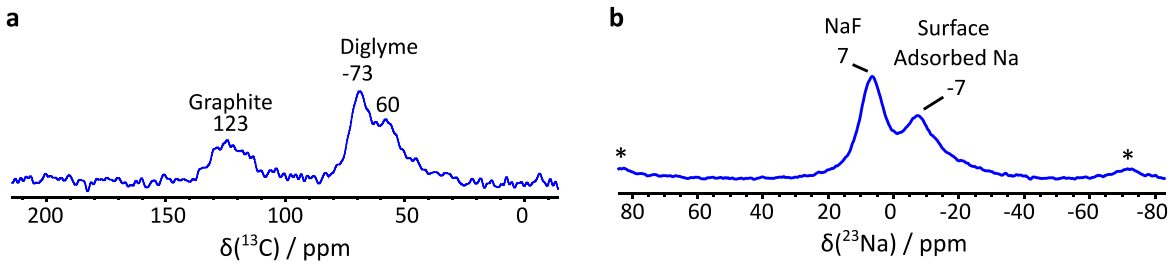

Figure 3-6: (a) ^{13}C and (b) ^{23}Na MAS SSNMR spectra of a graphite electrode, fully desodiated to 2 V with a 1 M $NaPF_6$ in diglyme electrolyte and not vacuum dried, Both spectra were collected at a MAS speed of 10 kHz. The asterisks in (b) corresponds to spinning side bands of the peak at 7 ppm.

To investigate how these spectra evolve for different states of charge (SOC), SSNMR spectra were also collected at the SOCs highlighted in Figure 3-7 (a). Four peaks present for the ^{13}C SSNMR spectra (Figure 3-7 (b)) collected at intermediate SOC. The peaks at 135 ppm and 123 ppm are both assigned to carbon atoms in the graphite lattice, with the 135 ppm signal dominating at lower SOCs and the 123 ppm peak becoming more intense with increased sodiation, such that for full sodiation (5 mV), only the 123 ppm signal is present. Shifting ^{13}C signals have also been observed for the lithiation of graphite (without co-intercalation), which have been partially assigned to an indirect Knight shift.[109] However, for the co-intercalation this shift may also be due to changes in chemical shielding. The peaks at 73 ppm and 60 ppm are again assigned to co-intercalate diglyme. They remain broad at all SOC, indicating that diglyme remains in a constrained environment, and grow in intensity as more diglyme is co-intercalated.

^{23}Na SSNMR spectra were also collected at the same SOCs (Figure 3-7 (c)). For these spectra, there is a peak at 7 ppm and two overlapping peaks at –7 and –10 ppm. This is because less material was available for these experiments and a smaller rotor (and hence faster spinning speed) was used resulting in more frictional heating which drives exchange between intercalated and surface Na species. These spectra were deconvoluted using three peaks at 7 ppm, –7 ppm and –10 ppm (as shown in Figure 3-7 (d)) corresponding to NaF, co-intercalated Na-diglyme and surface adsorbed electrolyte, respectively and the mass normalised integrals of these peaks are given in Figure 3-7 (e). The NaF signal (7 ppm) grows in intensity with increased sodiation, this could be due to the lower potentials of the half cells degrading more electrolyte or simply because to achieve lower potentials meant the electrodes spent more time in the presence of Na metal. The co-intercalated signal (–7 ppm) grows with increased sodiation, as expected as more Na is co-intercalated and the surface adsorbed electrolyte appears to be vary more randomly, as expected as this is not correlated to the SOC.

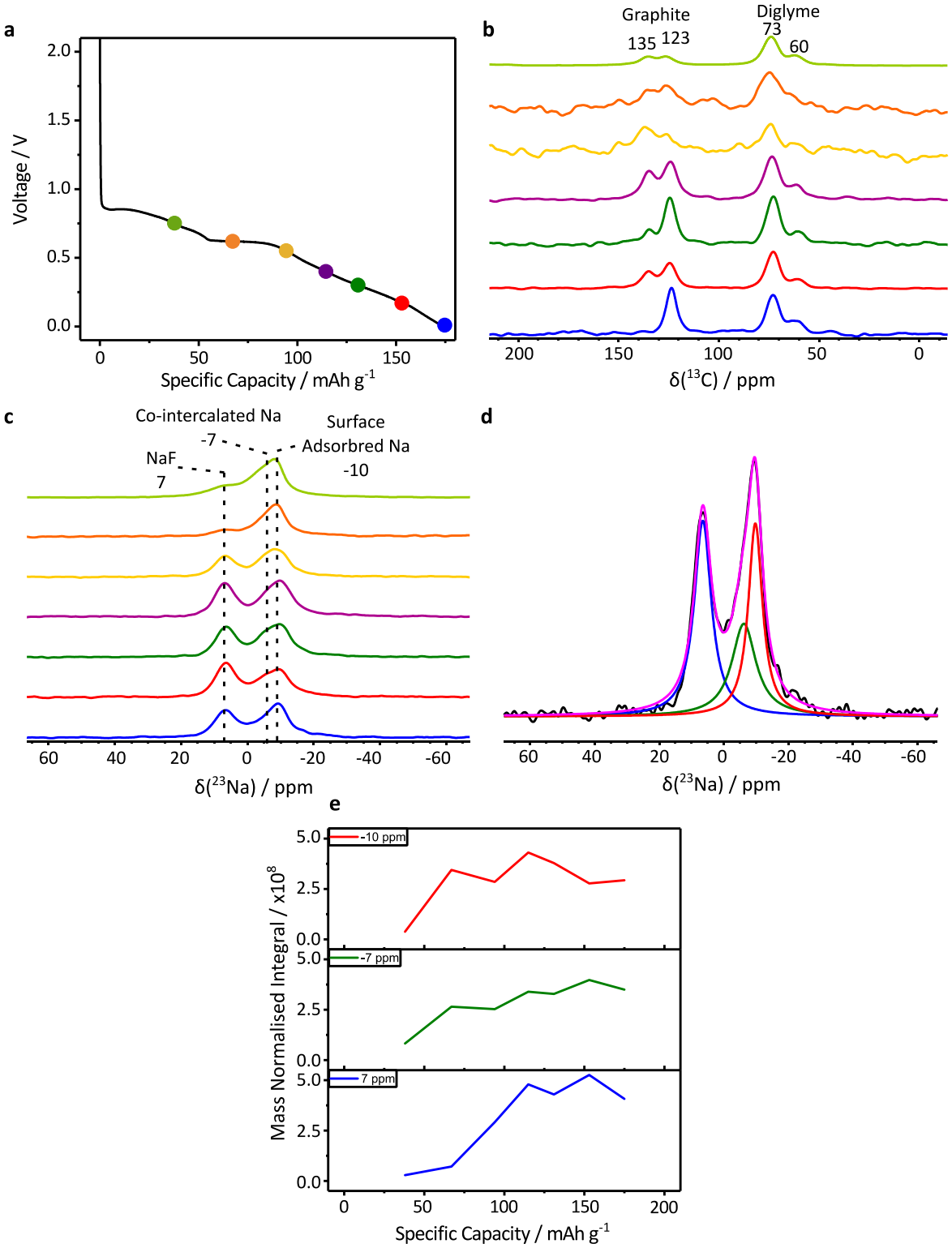

Figure 3-7: (a) A voltage profile of the first sodiation of graphite in a half-cell with a 1 M $NaPF_6$ in diglyme electrolyte, where several SOCs have been highlighte). (b) ^{13}C and (c) ^{23}Na MAS SSNMR spectra of graphite electrodes at the highlighted SOCs, that were not dried under vacuum, All spectra were collected at a MAS speed of 40 kHz. (d) ^{3}Na MAS SSNMR spectrum of a graphite electrode, fully sodiated to 10 mV with a 1 M $NaPF_6$ in diglyme electrolyte and not dried under vaccum. Collected at a MAS speed of 40 kHz (black). Overlaid with a simulated spectrum (purple_consisitng of three signals (blue, green and red). (e) Mass normalised intensities of the three ^{23}Na enviroments after deconvolution.

3.4.2 Co-intercalation into Hard Carbon

The voltage profile of a hard carbon electrode sodiated with an electrolyte consisting of 1 M $NaPF_6$ in diglyme is given in the red trace of Figure 3-8 (a). The voltage profile consists of two distinct regions, a sloping region from about 1.2 V to 0.1 V, and a plateau between 0.1 V to just above 0 V; the total capacity of the cell (340 mAh g^{-1}) is split roughly evenly between these two regions. These two regions and the specific capacity achieved are also commonly observed for hard carbons with standard carbonate electrolytes, such as 1 M $NaPF_6$ in EC:DMC (Figure 3-8, blue trace). where the sloping region has been ascribed to the storage of Na^+ ions at defects, within interlayers and on pore surfaces and the plateau corresponds to pore filling, leading to the formation of quasi-metallic Na. It is notable that for diglyme, two features are seen in the sloping region, with what appears to be a broad process between 1.2 V and 0.6 V and a second below that between 0.6 V and 0.1 V. The corresponding differential capacities (Figure 3-8 (b)) shows for both samples that there are two features between 1.2 V and 0.1 V. However the feature at lower voltages is more prominent for the diglyme electrolyte, as well as being at a slightly lower voltage, 0.4 V, compared to 0.6 V for EC:DMC. This suggests that a different electrochemical process, possibly co-intercalation is occurring for diglyme electrolyte.

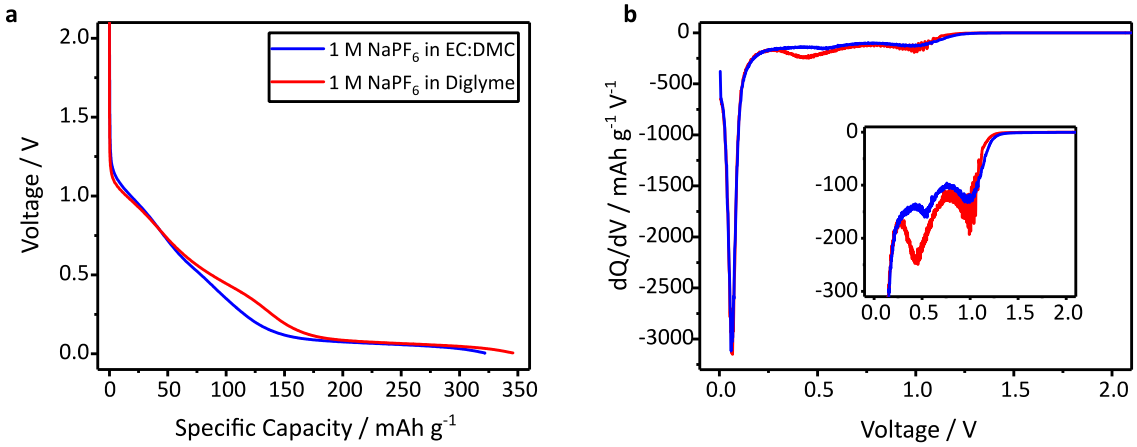

Figure 3-8: (a) Voltage profiles and (b) differenetial capacities (b) of the first sodiation of hard carbon half-cells discharged to 5 mV in half cells at rates corresponding to C/20 with electrolytes consiting of 1 M $NaPF_6$ in EC:DMC (blue traces) and 1 M $NaPF_6$ in diglyme (red traces).

The TGA curve for a hard carbon electrode, fully sodiated (to 5 mV) with a 1 M $NaPF_6$ in diglyme electrolyte that was not vacuum dried (Figure 3-9, red trace) has a similar profile to that of sodiated graphite (Figure 3-9, green trace), with mass loses at approximately 100 °C and 300 °C. However, the first mass loss is smaller than for graphite (~15 %), indicating that there is less diglyme present. To confirm that this diglyme is not surface adsorbed, a TGA curve for a dried hard carbon electrode (Figure 3-9, blue trace) was collected. The mass loss below 110 °C is much smaller (~4 %), indicating that most surface adsorbed diglyme is removed, but a small amount of co-intercalated diglyme remains. It is less than the subsequent mass loss (6 %), which occurs at a slightly lower

temperature of about 250 °C. To provide a reference without co-intercalation, a TGA curve was also collected for a hard carbon electrode that was fully sodiated (to 5 mV) with a 1 M $NaPF_6$ in EC:DMC electrolyte, that was also vacuum dried (Figure 3-9, black trace). For this sample, the TGA curve does not have a mass loss below 110 °C, as no co-intercalation has occurred, and significant mass losses occurring at 200 °C (~10 %) and 250 °C (~5 %). The results together provide further evidence for the co-intercalation of diglyme as co-intercalated diglyme is present for sodiated hard carbon.

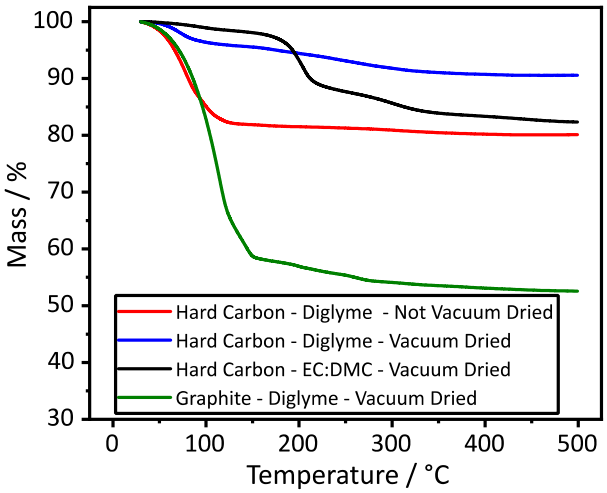

Figure 3-9: TGA curves of hard carbon electrodes, fully sodiated to 5 mV with a 1 M $NaPF_6$ in diglyme electrolyte not vacuum dried (red trace) and vacuum dried (blue trace), as well as a hard carbon electrode fully sodiated to 5 mV with a 1 M $NaPF_6$ EC:DMC electrolyte that was vacuum dried (black trace) and a graphite electrode fully sodited to 10 mV with a 1M $NaPF_6$ in diglyme electrolyte.

The ^{13}C SSNMR spectrum for a pristine (i.e., uncycled) hard carbon electrode is shown as the green trace in Figure 3-10 (a). There is a single broad, featureless peak at approximately 120 ppm. The isotropic chemical shift is consistent with sp^2 hybridized carbon atoms in hard carbon, and the breadth of this signal is due to the distribution chemical shifts from the various carbon environments in the disordered hard carbon structure, as well as broadening due to magnetic susceptibility effects. For the fully sodiated hard carbon (Figure 3-10 (a), red trace), there are three peaks, a broad peak at 135 ppm and narrower peaks at 71 ppm and 58 ppm. The broad peak is again, assigned hard carbon and the slight shift from 120 ppm to 135 ppm, along with the narrowing of this signal is a result of the expansion of the layers in the graphitic regions of the hard carbon and a concomitant reduction in the diamagnetic susceptibility, in a similar manner to that of graphite, as expansion due to co-intercalation limits the interactions between the carbon layers. However, the change in chemical shift of these signal on sodiation are in the opposite to what is seen for graphite, where a shift to lower chemical shifts occurs on sodiation. This is examined further in the discussion section.

The peaks at 71 ppm and 58 ppm are highlighted in the inset figure and are assigned to diglyme. Unlike those in the spectra of graphite, these signals are narrower and resolved *J*-coupling multiplets ($^1J(^1H\text{-}^{13}C)$ = 150 Hz) are visible. This suggests that diglyme is more mobile in hard carbon, possibly

because of the larger interlayer spacings in these materials and/or the inclusion of diglyme molecules within the micropores. The ^{13}C SSNMR spectrum for a fully sodiated hard carbon electrode that was dried under vacuum (Figure 3-10 (a), blue trace) shows the same signals but the diglyme peaks at 71 ppm and 58 ppm have a lower intensity suggesting that diglyme is more easily removed than from hard carbon than graphite, or that a smaller amount of co-intercalation occurs for hard carbon.

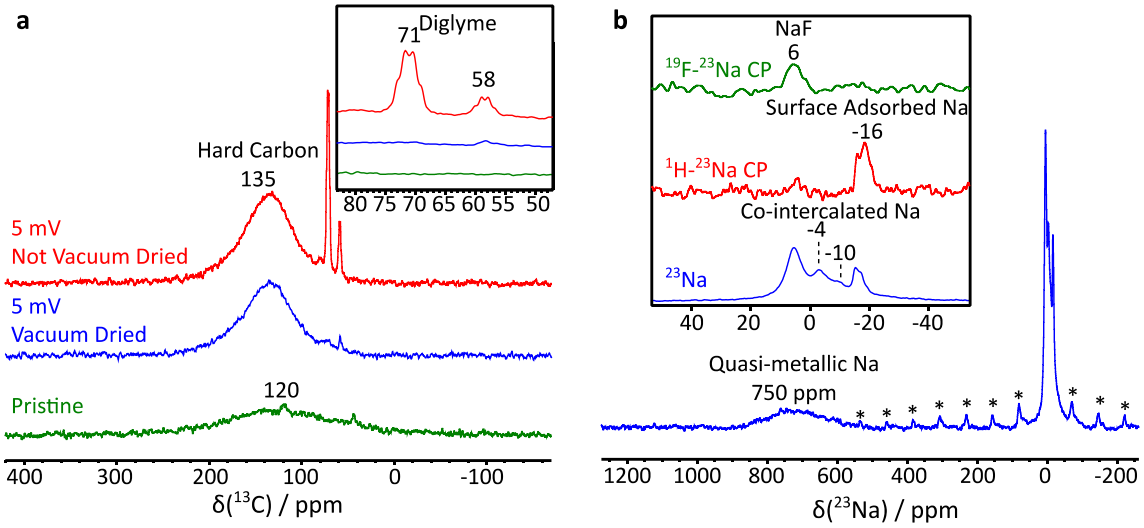

Figure 3-10: (a) ^{13}C MAS SSNMR spectra of a pristine hard carbon electrode (green trace) as well as hard carbon electrodes fully sodiated to 5 mV with a 1 M $NaPF_6$ in diglyme electrolyte, either vacuum dried (red trace) and not vacuum dried (blue trace). All spectra were collected at a MAS speed of 25 kHz. (b) A ^{23}Na MAS SSNMR spectrum of a hard carbon fully sodiated to 5 mV with a 1 M $NaPF_6$ in diglyme electrolyte, that was vacuum dried (blue trace) with ^{1}H-^{23}Na (red trace) and ^{19}F-^{23}Na (green trace) CP MAS SSNMR spectra of the same sample highlighted in the inset, all collected at a MAS speed of 10 kHz. The contact times used for the CP experiments were 5750 μs for ^{1}H-^{23}Na and 6500 μs for ^{19}F-^{23}Na.. The asterisks in the ^{23}Na spectrum indicates spinning sidebands that correspond to the peak at 6 ppm.

A ^{23}Na SSNMR spectrum was also collected for the fully sodiated, vacuum dried hard carbon (Figure 3-10 (b)). This spectrum has a prominent broad signal centred around 750 ppm, which is assigned to quasi-metallic Na species that form in the pores of the hard carbon and is at the same chemical shift observed for hard carbon sodiated with a carbonate electrolyte. This suggests that the co-intercalation of diglyme molecules into the hard carbon structure does not interfere or prevent the formation of quasi-metallic Na clusters at lower voltage, the co-intercalated diglyme is likely being stored between the carbon layers at this point. The diamagnetic region is highlighted in the inset figure, where four peaks are observed at 6 ppm, –4 ppm, –10 ppm and –16 ppm, which are similar to the peaks observed in the ^{23}Na spectrum of sodiated graphite. The ^{19}F-^{23}Na CP spectrum (Figure 3-10 (b), green trace) shows a single peak at 6 ppm, which is again assigned to NaF, a typical SEI component. The ^{1}H-^{23}Na CP spectrum (Figure 3-10 (b), red trace) has signals around –16 ppm, which are assigned to surface adsorbed Na-diglyme complexes. The remaining signals at –4 ppm and –10 ppm coalesce into a single peak when cooled down to –20 °C (Figure 3-11 (a)) are assigned to co-intercalated Na-diglyme complexes, with the two peaks corresponding to different environments in disordered hard carbon,

compared to ordered graphite. A ^{23}Na MAS SSNMR spectrum was also collected for fully sodiated hard carbon, that had been washed with DMC before being vacuum dried (Figure 3-11 (b), red trace). There are similar peaks at 7, –4 and –16 ppm. The peak at –16 ppm can be highlighted with a ^{1}H-^{23}Na CP experiment (Figure 3-11 (b), blue trace). However, the lower intensity in the ^{23}Na spectrum indicates that most of the surface adsorbed, Na-diglyme can be removed, leaving behind NaF and co-intercalated Na.

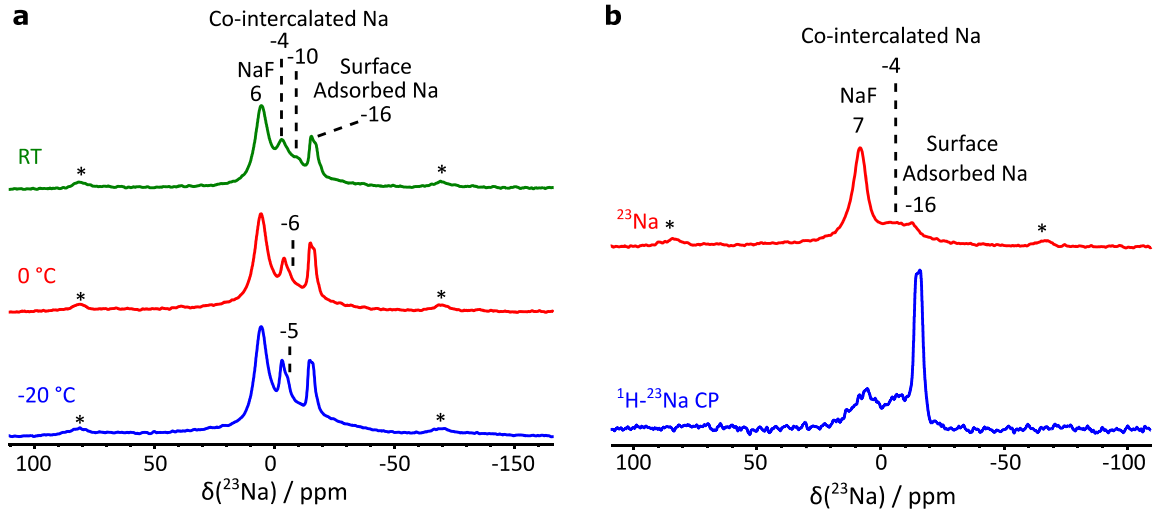

Figure 3-11: (a) VT ^{23}Na MAS SSNMR spectra of a hard carbon electrode fully sodiated to 5 mV with a 1 M $NaPF_6$ in diglyme electrolyte, dried under vacuum at room temperature (green trace), 0 °C (red trace) and – 20 °C (blue trace). Collected at a MAS speed of 10 kHz and the asterisks indicate spinning side bands that correspond to the peak at 6 ppm. (b) ^{23}Na (red trace) and ^{1}H-^{23}Na CP (blue trace) MAS SSNMR spectra of a hard carbon electrode fully sodiated to 5 mV with a 1 M $NaPF_6$ in diglyme electrolyte, washed with DMC and dried under vacuum. A MAS speed of 10 kHz was used and the "" indicates spinning side bands that correspond to the 7 ppm peak. A contact time of 10000 μs was used for the CP experiment.*

SSNMR spectra were also collected for a hard carbon electrode after one full cycle (desodiated to 2 V), that was not dried under vacuum. The ^{13}C SSNMR spectrum (Figure 3-12 (a)) shows a broad hard carbon signal at 130 ppm, and diglyme signals at 73 ppm and 60 ppm. Compared to the spectrum of the fully sodiated sample, the hard carbon signal not returned to the shift of pristine (120 ppm) and has broadened slightly. This suggests that, similarly to graphite, there is an irreversible expansion on the first sodiation-desodiation cycle, which could be is probably due to a small amount of Na-diglyme complexes becoming trapped in hard carbon. The diglyme signals at 73 ppm and 60 ppm are still relatively intense and narrow; however, resolved coupling multiplets are not observed, further indicating that some (physically constrained) diglyme remains on desodiation. The ^{23}Na SSNMR spectrum (Figure 3-12 (b)) does not have a broad peak at 750 ppm, indicating that the quasi-metallic Na is removed from the pores in hard carbon. In the diamagnetic region, shown in the inset, there are multiple overlapping signals with two main peaks at 7 and –8 ppm. The 7 ppm signal remains at similar intensity to the fully sodiated sample, consistent with its assignment to NaF, which is likely formed

from degradation of $NaPF_6$. The prominent side band manifold indicate a strongly quadrupolar environment, which could be explained by NaF being in a nanocrystalline environment. The peak at about –8 ppm can again be assigned to surface adsorbed electrolyte and there is a notable absence of a peak at –4 ppm which indicates that there is minimal co-intercalated Na in this sample.

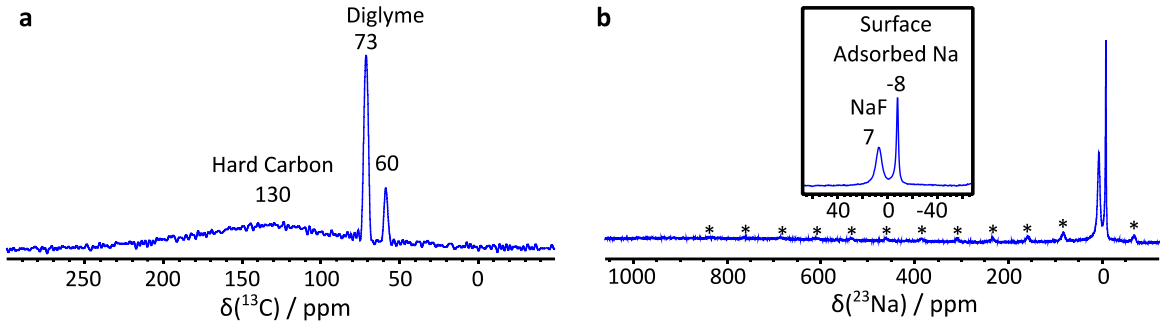

Figure 3-12: (a) ^{13}C and (b) ^{23}Na MAS SSNMR spectra of hard carbon electrodes after one full cycle that were desodiated to 2 V with a 1 M $NaPF_6$ in diglyme electrolyte and not dried under vacuum. Both spectra were collected at a MAS speed of 10 kHz and the asterisks indicates spinning side bands that correspond to the peak at 7 ppm.

^{23}Na SSNMR spectra (Figure 3-13 (b)) were collected without vacuum drying at the intermediate SOCs highlighted in Figure 3-13 (a). In the spectrum for the sample sodiated to 60 mV (i.e., half-way along the plateau region), there is a broad signal at approximately 550 ppm, for fully samples fully sodiated to 5 mV this signal appears at 750 ppm. This indicates that the Na species in the pores of the hard carbon become increasingly metallic as more Na is added and a greater amount of electron density is transferred from the carbon sheets. These signals are not present for the samples sodiated to 600 mV and 200 mV, demonstrating that pore filling only occurs along the plateau. This agrees with mechanism previously reported for the sodiation of hard carbon with carbonate electolytes.[31,33, 110]

The inset in Figure 3-13 (b) shows an expanded view of the diamagnetic regions, which contains several overlapping signals including peaks at 7 ppm and –9 ppm. These peaks are similar to those observed in the spectra of graphite, where co-intercalation is known to occur. Additionally, for the samples sodiated to 600 mV and 200 mV (the sloping region) there are broad signals at lower chemical shifts (–23 ppm and –12 ppm, respectively). Similar signals have also been observed in the ^{23}Na NMR spectra for hard carbon sodiated with carbonate electrolytes, where they are assigned to the Na between the carbon layers and at defect sites.[31] To probe the identity of these species, further spectra were collected for a hard carbon electrode sodiated to 200 mV that was dried under vacuum, as this should remove any diglyme that is not co-intercalated, such as surface adsorbed diglyme. The ^{13}C SSNMR spectrum (Figure 3-13 (c)) has a very broad graphitic peak at 130 ppm and two sharper diglyme peaks at 72 ppm and 59 ppm, with very low intensities, which indicates that some co-intercalated

diglyme remains after drying under vacuum. The ^{23}Na spectrum (Figure 3-13 (d)) ^{19}F-^{23}Na and ^{1}H-^{23}Na CP experiments (Figure 3-13 (d), dark yellow and grey traces) did not show signals at –20 ppm, and therefore, consistent with the assignment of this peak to un-coordinated Na^{+}-ions between the carbon layers.

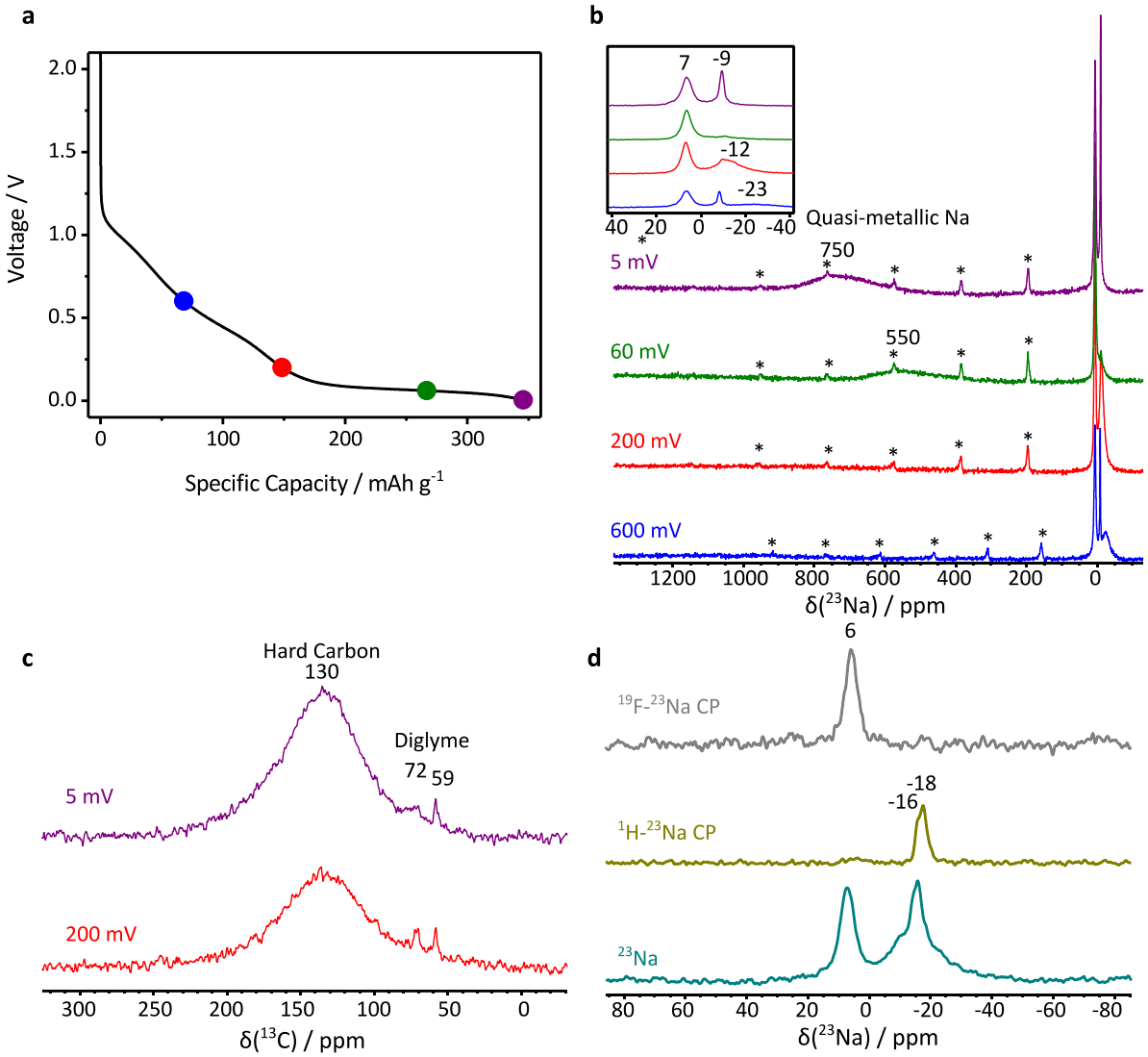

Figure 3-13: (a) Voltage profile of a hard carbon electrode sodiated with in a half-cell with a 1 M $NaPF_6$ in diglyme electrolyte, with four SOCs highlighted.(b) ^{23}Na MAS SSNMR spectra at the highlighted SOCs, without vacuum drying that were collected with a MAS speed of 25 kHz and the asterisks indicates spinning side bands that correspond to the peak at 7 ppm. (c) ^{13}C MAS SSNMR spectra of vacuum dried hard carbon electrodes, sodiated to 200 mV (red trace) and 5 mV (purple trace) with a 1 M $NaPF_6$ in diglyme electrolyte, collected at a MAS speed of 25 kHz. (d) ^{23}Na (teal trace), ^{1}H-^{23}Na CP (dark yellow trace) and ^{19}F-^{23}Na CP (grey trace) MAS SSNMR spectra for a hard carbon electrode partially sodiated to 200 mV and dried under vacuum, collected at a MAS speed of 10 kHz with CP contact times of 5750 μs for ^{1}H-^{23}Na and 2750 μs for ^{19}F-^{23}Na.

The ^{23}Na SSNMR spectra at all the four SOCs were deconvoluted using peaks with similar chemical shifts for both hard carbon and graphite; 7 ppm (NaF), –4 ppm (co-intercalated Na) and –10 ppm (surface adsorbed electrolyte), as well as an additional broad peak at about –20 ppm (un-

coordinated, intercalated Na), as shown in Figure 3-14 (a). From the mass normalised integrals (Figure 3-14 (b)), the intensity of the signal corresponding to NaF appears to grow on increased sodiation as does that of the co-intercalated Na (although the intensity is much lower, indicating only a small amount of Na is co-intercalated). The intensity of the signal for surface adsorbed diglyme does not appear to correlate with SOC and the signal for uncoordinated, intercalated Na grows along the slope and disappears on the plateau.

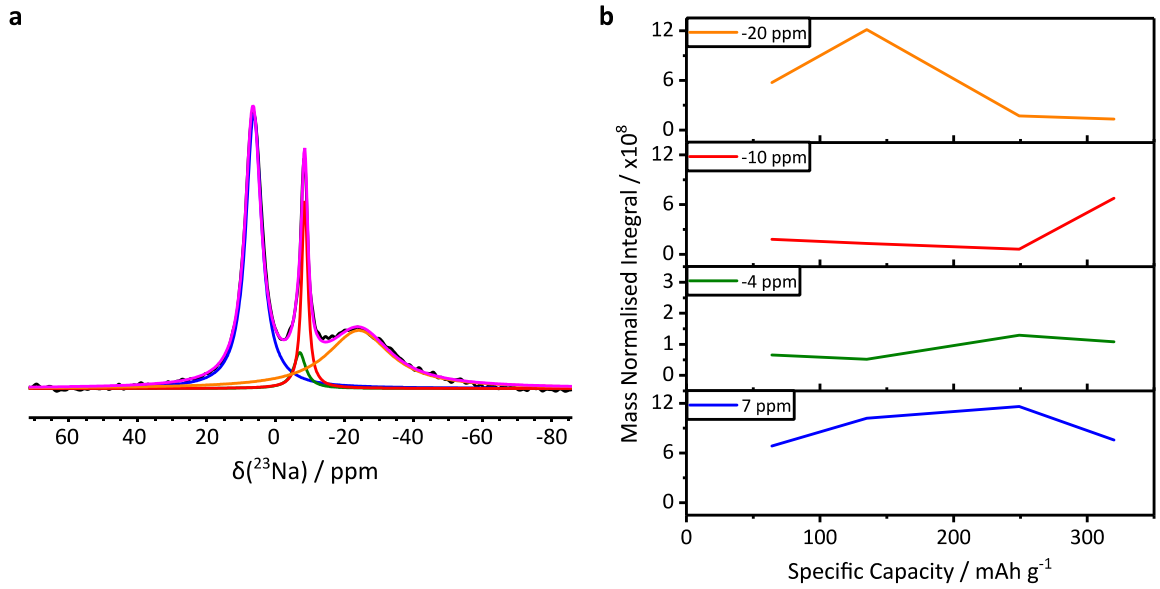

Figure 3-14: (a) A ^{23}Na MAS SSNMR spectrum of a hard carbon electrode partially sodiated to 600 mV with a 1 M $NaPF_6$ in diglyme electrolyte, not dried under vacuum, collected at a MAS speed of 25 kHz (black trace). Overlaid with a simulated spectrum (purple trace) consisitng of four signals (blue, green, red and orange traces). (b) Mass normalised intensities of the four deconvoluted peaks at different SOCs.

3.5 Discussion

When hard carbon and graphite electrodes are sodiated with an electrolyte consisting of 1 M $NaPF_6$ in diglyme, several differences are observed in the electrochemistry. For graphite, the specific capacity for the first sodiation is 170 mAh g^{-1} and three regions are observed in the voltage profile, a sloping region from 1.0 V to 0.6 V, a plateau at 0.6 V and a slope from 0.6 V to just above 0 V. This corresponds a staged mechanism of sodiation and it is notably different to when an electrolyte of 1 M $NaPF_6$ in EC:DMC is used and the specific capacity is only 10 mAh g^{-1}, indicating that intercalation does not occur. When hard carbon is sodiated with a 1 M $NaPF_6$ in diglyme electrolyte, the specific capacity is much higher at 340 mAh g^{-1} and two regions are observed in the voltage profile, a sloping region from 1.1 V to 0.1 V and a plateau from 0.1 V to just above 0 V, these regions correspond to intercalation of Na between the carbon layers and the formation of quasi-metallic Na in the pores of hard carbon. This is much more similar to the performance when 1 M $NaPF_6$ in EC:DMC is used as an electrolyte, and the only difference is that for diglyme there is a larger feature on the slope between 0.6 V and 0.1 V, which could correspond to the co-intercalation of diglyme.

Figure 3-15 (a) shows ^{13}C SSNMR spectra for both sets electrodes after full sodiation in a 1M $NaPF_6$ in diglyme electrolyte. The graphite and hard carbon signals show the expansion of the carbon electrodes on sodiation, as the graphite and hard carbon signals sharpen on increased sodiation due to the decreased diamagnetic susceptibility, although the signals for sodiatied hard carbon signals at ~120 ppm are broader, reflecting the range of carbon environments. Both electrodes also saw a shift in the position of the graphite/hard carbon electrodes on sodiation, but in different directions, with the graphite signal shifting to a lower chemical shift and hard carbon shifting to a higher chemical shift.

This suggests that multiple different interactions are occurring, as they are known to when graphite is lithiated with a carbonate electrolyte. For this system, there is an initial shift in the position of the graphite peak in ^{13}C NNMR to a higher frequencies, this is then followed by a more significant shift to lower chemical frequencies on increased lithiation. The initial shift to higher frequencies is a result of a change in the contribution of chemical shift to the lineshape. The shift to lower frequencies is due to a contribution from the Knight shift that becomes more prominent as more Li is added and more electron density is added to the conduction band of graphite. When graphite is sodiated with a diglyme electrolyte, there is a slight shift to lower frequencies. Despite being in the opposite direction to that observed for lithiated graphite, this shift is likely still an effect changes in the chemical anisotropy. A more significant Knight shift to lower frequencies is not observed as the steric hinderance of the co-intercalated diglyme molecules means not as much charge is stored in the same volume of graphite and consequently, less electron density is added to the conduction bands of graphite.[111]

Due to the range of carbon environments and the increased amount of defects in hard carbon, the overall trends observed in the ^{13}C NNMR for hard carbon are likely to be more complex than those for graphite. For example, due to the presence of curved carbon sheets, the conduction bands of hard carbon are not pure p_z-orbitals like they are in graphite and are likely to have more character from the *s*-orbitals. The slight shift in the peak to a higher frequency upon sodiation still mirrors that of lithiated graphite and is likely due to changes in the contribution from chemical shift; however, no subsequent shift to lower frequencies occurs on increased sodiation. This is because most Na is being stored as quasi-metallic Na the pores of hard carbon, which requires the transfer of charge from the hard carbon to reduce the Na^+ to metallic Na. This charge transfer results in less electron density in the conduction band of the carbon, meaning there is a reduced contribution from Knight shift in the ^{13}C NMR spectra for sodiated hard carbon.

Diglyme signals are also present in the ^{13}C spectra for both samples and grow with increased sodiation. For graphite, these are quite broad and *J*-couplings are not observed, indicating diglyme is in a more physically restrained environment. Whereas for hard carbon, coupling multiplets are present indicating diglyme is less physically constrained, which suggest diglyme is more mobile in hard carbon, possibly due to a larger spacing between the carbon sheets in hard carbon, compared to graphite. For

fully sodiated graphite, dried under vacuum, the peak integral ratio between the graphite and diglyme methyl peaks is approximately 5:1. Whereas, for fully sodiated hard carbon dried under vacuum, the ratio of peak integrals between the hard carbon and the methyl groups of diglyme is approximately 100:1, which is about 20 times less than that of graphite. This indicates that less diglyme co-intercalates into hard carbon, with a lot of the capacity still responding to other processes, such as pore filling, or that diglyme is less tightly bound and can be more easily removed under vacuum.

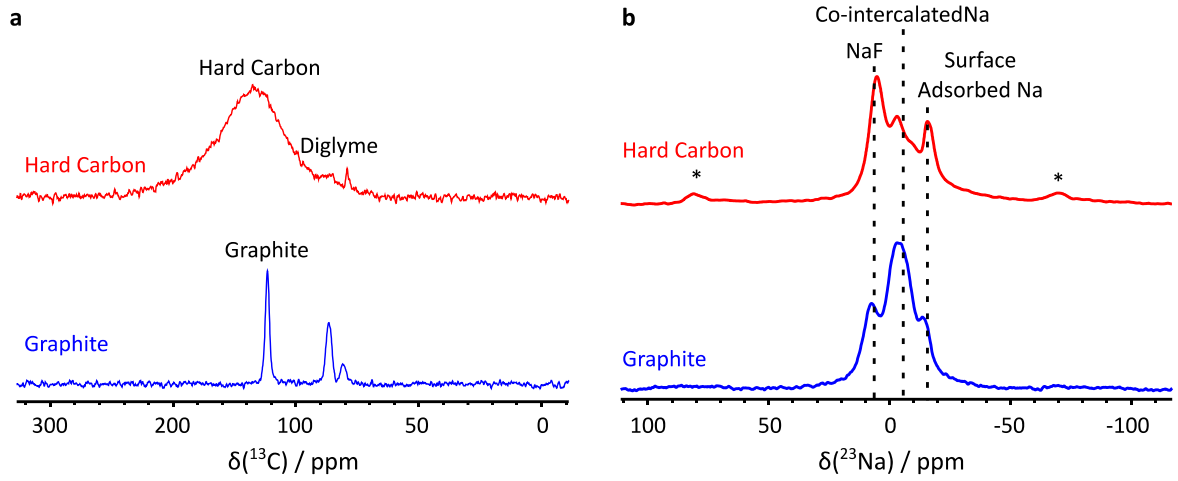

Figure 3-15: (a) ^{13}C and (b) ^{23}Na MAS SSNMR spectra of hard carbon (red traces) and graphite (blue traces) electrodes fully sodiated to 5 mV and 10 mV, respectively with a 1 M $NaPF_6$ in diglyme electrolyte and not dried under vacuum. ^{13}C spectra were collected at a MAS speed of 20 kHz and ^{23}Na spectra wre collected at a MAS speed of 10 kHz and the asterisks indicates spinning side bands.

^{23}Na SSNMR spectra were collected for both electrodes, as demonstrated by Figure 3-15 (b), which shows spectra for fully sodiated graphite and hard carbon electrodes. Both electrodes appeared to give similar signals in the diamagnetic region, with a peak at 7 ppm and several overlapping signals at –4 and –14 ppm. By comparing the intensity of the signals at several SOCs, including desodiation, as well using more advanced experiments such as CP, it was determined that the 7 ppm signal corresponds to NaF, the signal at –14 ppm corresponds to surface adsorbed Na coordinated to diglyme and the signal at –4 ppm is co-intercalated diglyme. Additionally, for hard carbon there are broad signals at around –20 ppm for partial sodiation (along the sloping region) and 750 ppm (full sodiation, along the plateau). The latter of these corresponds to quasi-metallic Na.

Based on these results, it appears that some co-intercalation of diglyme does occur for hard carbon, although not all the Na that intercalates into hard carbon does so with diglyme, a significant amount still corresponds to quasi-metallic Na in the pores of hard carbon. This is evidenced by hard carbons having a similar capacity with carbonate and diglyme electrolytes. It is likely that the co-intercalated diglyme only responds to Na intercalated between the carbon layers, in similar environments to those found in graphite, this is demonstrated in Figure 3-16 below.

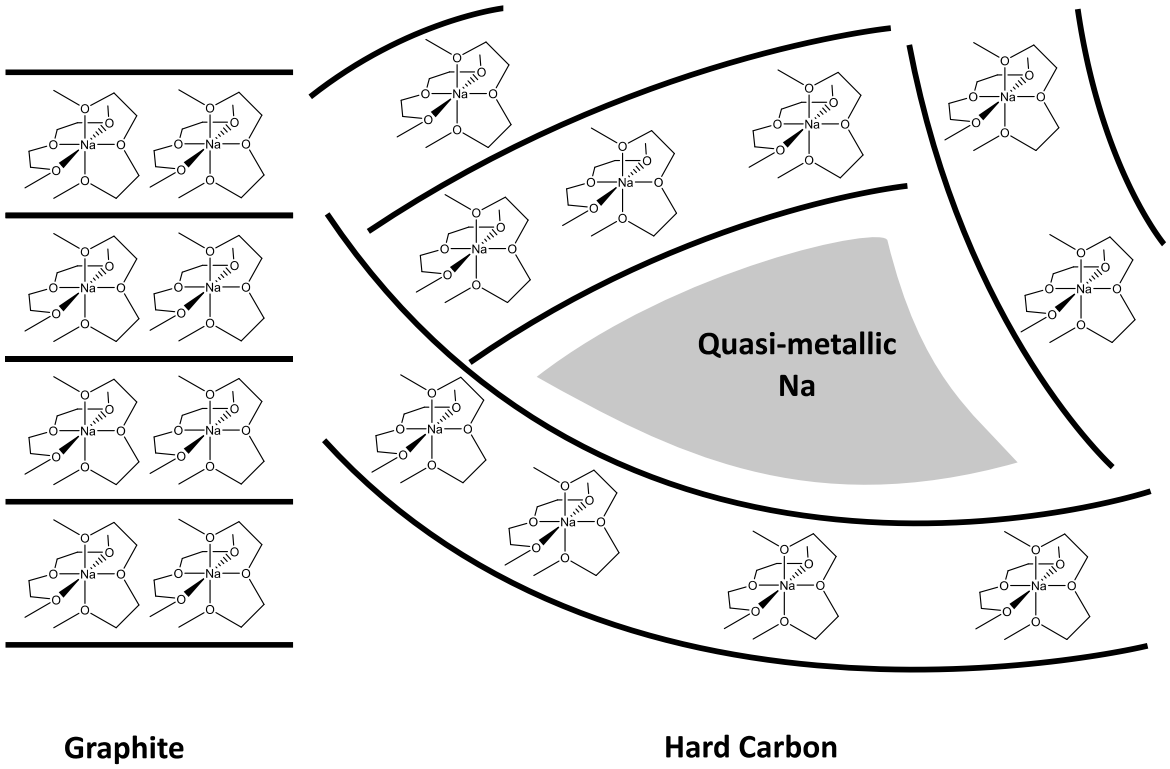

Figure 3-16: Schematics showing the intercalation of Na-diglyme complexes into graphite and hard carbon.

3.6 Conclusion

In this study, we have shown that whilst graphite does not intercalate Na with normal carbonate electrolytes, a significant capacity of approximately 170 mAh g^{-1} can be achieved when diglyme is used as an electrolyte solvent. It is thought that this is because diglyme co-intercalates with Na^+ ions into graphite and shields Na^+ ions from unfavourable interactions with graphite. Evidence for this is provided by SSNMR. ^{13}C SSNMR spectra show that graphite expands on sodiation and that diglyme remains in a physically restricted state, even after vacuum drying, as expected for co-intercalated Na-diglyme complexes. Additionally, in ^{23}Na SSNMR signals were observed for co-intercalated Na, NaF and surface-adsorbed Na diglyme species, as confirmed by CP experiments. By performing peak fitting, it can be seen that the intensity of the co-intercalated species and NaF increases with increased sodiation.

Furthermore, by performing similar SSNMR studies on hard carbon electrodes sodiated with a diglyme-based electrolyte we have provided evidence that diglyme also co-intercalates into hard carbon. From ^{13}C SSNMR, it can be determined that hard carbon also expands on sodiation and diglyme molecules have relatively limited motion, although not as limited as that of diglyme in graphite. Additionally, diglyme can be more easily removed from hard carbon by drying under vacuum, and both of these effects could be due to the larger spacing between carbon sheets in hard carbon, the Na^+ ions accommodating more weakly bound diglyme molecules in their local coordination shells. ^{23}Na SSNMR also provided evidence for environments that correspond to NaF, surface adsorbed Na and co-intercalated diglyme. However, it is notable that a smaller amount of diglyme co-intercalates into hard

carbon compared to graphite and it exists in multiple environments, which is probably due to the range of defect sites present in hard carbon. Whilst we have provided evidence for the co-intercalation of diglyme into hard carbon, further studies will be required to understand the motion of diglyme in hard carbon and how it compares to that of graphite.

4 Probing the Dynamics of Co-intercalated Diglyme in Hard Carbon

4.1 Abstract

When diglyme is used as an electrolyte solvent for NIBs with hard carbon anodes, an improved rate performance can be achieved when compared to standard carbonate electrolytes. In the previous chapter, we provided evidence that this could be due to diglyme molecules co-intercalating with Na^+ ions into hard carbon, in a similar way to graphite, albeit it to a lesser extent. In this chapter, we set out to study the dynamics of co-intercalated diglyme using a combination of static variable temperature ^2H SSNMR and simulations. The dynamics of diglyme are then used to probe the structure of hard carbon. The motion of diglyme can be described by simulating a molecular rotation of diglyme with a lognormal distribution of rotation rates, which is indicative of the range of different sites that Na-diglyme complexes can occupy in hard carbon. The motion of diglyme increases on sodiation, possibly indicating that hard carbon expands on sodiation, giving diglyme more space to rotate. Furthermore, by comparing hard carbons with different capacities, where the plateau corresponds to a greater proportion of the capacity for the higher capacity hard carbons, it was found hard carbons with higher capacities had less mobile diglyme, possibly reflecting the more ordered structure of high-capacity hard carbons.

4.2 Introduction

As previously discussed, Na does not normally intercalate into graphite.[23] However, if diglyme is used as an electrolyte solvent, a good electrochemical performance can be achieved for NIBs with graphite anodes as diglyme co-intercalates with Na^+ ions into graphite.[42,99] Recently Zhu *et al.*[103] reported that if diglyme is used as an electrolyte solvent for NIBs with hard carbon anodes, an improved electrochemical performance can be achieved with long-lasting reversible capacity at high rates, which the authors ascribed to reduced electrochemical polarization and the formation of a thinner SEI. In the previous chapter, we provided evidence that diglyme co-intercalates into hard carbon in a similar way to graphite, albeit to a lesser extent, which could possibly explain the better performance at high rates. To investigate if this is the case, a more detailed understanding about the dynamics of diglyme co-intercalated into hard carbon is needed.

Information about the structure and dynamics of diglyme co-intercalated with Na into graphite has previously been obtained by Gotoh *et al.*[102] Elemental analysis was first used to show that two diglyme molecules coordinate to each Na^+ ion. The dynamics of these complexes was then studied using SSNMR as it is sensitive to subtle differences in the local environment of a nucleus. Specifically, variable temperature (VT) static ^2H SSNMR was used to study the dynamics of deuterated diglyme (diglyme-d_{14}) co-intercalated into graphite. ^2H SSNMR is particularly sensitive to different types of motion and the rates at which they occur, hence it has been used to study dynamics in several different systems including metal organic frameworks (MOFs)[112] and crown ethers.[113] Furthermore, the small quadrupole moment of ^2H (Q = 0.286 fm^2)[114] means the spectra are relatively narrow and easy to

acquire, and the low natural abundance of ^{2}H (0.0115 %)[115] means it can safely be assumed that the only ^{2}H signals present are due to diglyme-d_{14}.

^{2}H is a quadrupolar nucleus with $I = 1$. When placed in an external magnetic field, the three spin states are degenerate, giving rise to two transitions: $m_I = 1 \leftrightarrow m_I = 0$ and $m_I = 0 \leftrightarrow m_I = -1$. Due to the quadrupolar interaction, these transitions are not equivalent in energy, and when a static (i.e., not under MAS conditions) ^{2}H spectrum is collected for a powdered sample, (where all crystallites are orientated randomly with respect the external magnetic field), two powder patterns are observed. These patterns overlap to form a so-called Pake doublet,[84] which has three main components: horns, shoulders and feet. The shapes of the patterns are determined by two parameters: the quadrupole coupling constant (C_Q) and the asymmetry parameter (η_Q). To investigate the dynamics in a system, VT static SSNMR is used, and the resulting lineshapes are simulated to extract information about the modes of motions and their rates. It is then possible to propose a possible model for the motion of the diglyme molecules.

The motion observed by ^{2}H NMR spectra can be split into three motional regimes depending on the relative magnitudes of the exchange frequency between different sites (ν_{ex}) and the quadrupolar frequency ($\nu_Q = 3C_Q/(2I(2I - 1))$). The first of these is the slow-motion limit (SML) and it corresponds to when ν_{ex} is much lower than ν_Q. The intermediate motional regime (IMR) refers to when ν_{ex} and ν_Q are approximately equal, and the fast motion limit (FML) corresponds to ν_{ex} being significantly larger than ν_Q. Decreasing the rate of motion below than the SML does not change the spectrum, and increasing the rate of motion above the FML does also not alter the lineshape of the spectrum. The IMR is the most useful regime as slight changes in dynamics will vary the lineshape of the spectra significantly, which means detailed information about the type of motion present and the rate it is occurring at can be obtained.

Gotoh *et al.*[102] used VT ^{2}H SSNMR to investigate graphite that was sodiated with a diglyme based electrolyte. At low temperatures, diglyme is rigidly coordinated to Na^+ through all three O atoms, and the only motion present is the rotation of the terminal methyl groups. At higher temperatures, there is a narrowing of the powder patterns and the changes in the spectra could be explained by considering a model in which diglyme coordinates more weakly to Na through one O atom resulting in molecular rotation of diglyme about an axis that is collinear with the central O-Na bond. The authors suggest that the good rate performance observed when diglyme is used as a solvent might be explained by the high mobility of diglyme, enabling the rapid Na diffusion through graphite and that the flexible structure of the Na-diglyme complex could also enable intercalation into graphite without exfoliation of the graphite sheets.

In this chapter, the dynamics of the co-intercalated diglyme molecules in hard carbon were examined using static VT ^{2}H SSNMR. It was found that at low temperatures, the motion of diglyme is restricted, with only methyl group rotation occurring. As the temperature is increased, the motion of

diglyme in hard carbon can be modelled by simulating diglyme molecules rotating about an axis that is collinear with the bond between the central O atom and the Na^+ ion with a lognormal distribution of rotation rates, However, for graphite this distribution of rates is not required. We postulate that the disordered nature of the hard carbons gives rise to a distribution of the rates of motion of the diglyme molecules and that the larger spacings between the carbon sheets in the graphitic domains allows for larger amplitude motions that are activated at lower temperatures. Furthermore, comparing the dynamics of co-intercalated diglyme at intermediate SOCs provides evidence for the expansion of hard carbon on sodiation. Hard carbons with different capacities were also compared, and here it was found that as the capacity of hard carbon is increased the motion of diglyme decreases, possibly because higher capacity carbons are more graphitic which means there is less space for diglyme to move in.

4.3 Experimental

4.3.1 Sample Preparation

The hard carbons used in this chapter came from three different sources, the first of these (**A**) is a low-capacity hard carbon prepared by Au *et al.*[33] from hydrothermal carbonisation of glucose followed by pyrolysis at 1000 °C. The second hard carbon (**B**) is a commercially available hard carbon (Carbotron P(J), Kureha Corporation). The third hard carbon (**C**) is a high-capacity carbon prepared by C. Zhao *et al.*[116] from charcoal derived from wood that was first heated at 800 °C under flowing Ar. After cooling to room temperature, the sample was washed with dilute hydrochloric acid (30%) and deionized water. Then sample was then heated again at 1900 °C under flowing Ar.

Electrodes of **A** were prepared by mixing a slurry of the active material (90 wt%) with sodium carboxymethyl cellulose (M_w = 250000, Sigma Aldrich) (10 wt%) in water and then cast onto Al foil. Electrodes of **B** were prepared in a similar way by mixing the active material (90 wt%) with poly(vinylidene fluoride-co-hexafluoropropylene) (PVDF-HFP, Kynar, 5 wt%) and Super P (Timcal, 5 wt%) into a slurry with *N*-methyl-2-pyrrolidone (NMP, Sigma-Aldrich), which was cast on Cu foil. Electrodes of **C** were prepared by mixing the active material (90 wt%) with poly(vinylene fluoride) (PVDF, 5 wt%) with carbon black (5 wt%) into a slurry with NMP then casting onto Al foil. All electrodes were subsequently dried at 120 °C *in vacuo* prior to use.

Coin cells were prepared from these electrodes using 2032 coin cell components in an Ar glovebox (O_2 < 1 ppm, H_2O < 1 ppm). Na metal (Sigma-Aldrich) was used as a counter electrode, 150 μL of 1 M $NaPF_6$ (Acros Organics) in deuterated diglyme-d_{14} (Cambridge Isotope Laboratories) was used as an electrolyte and borosilicate glass fibre (Whatman, GF/B) was used as the separator. $NaPF_6$ was dried at 120 °C *in vacuo* prior to use.

The half-cells were sodiated galvanostatically to either 5 mV (fully sodiation), 60 mV, 200 mV or 600 mV using a Biologic MPG2 battery cycler at a rate of *C*/20. This corresponds to theoretical

capacities of 250 mAh g^{-1}, 300 mAh g^{-1} and 450 mAh g^{-1} in 20 hours based on the mass of active material of **A**, **B** and **C**, respectively

4.3.2 SSNMR Experiments

SSNMR experiments were performed on electrodes that had been cycled in coin cells. After cycling, the cells were transferred to an Ar glovebox where they were opened, the hard carbon electrodes were removed and dried under vacuum for 15 minutes in the glovebox prechamber or a Büchi B-585 drying oven, unless specified that SSNMR spectra were collected without vacuum drying. The electrodes films were then scraped off the current collectors and packed into rotors.

All SSNMR spectra were collected on a Bruker Advance III HD console, equipped with a 11.7 T Bruker magnet, except for one ^{23}Na spectrum that was collected with a 16.4 T magnet. For the ^{2}H SSNMR spectra, a Bruker double-channel static probe was used with a custom-made 5 mm coil. A quadrupolar echo was used with a pulse length of 2 μs and an inter-pulse delay (i.e., between the 90° and 90° pulse) of 16 μs. For the ^{23}Na SSNMR either a 2.5 mm or 1.3 mm Bruker double-channel MAS probe was used. A single pulse experiment was used with a 90° pulse length of 3.66 μs and a recycle delay of 1 s. Temperature calibrations were performed using the temperature-dependent chemical shift of $Pb(NO_3)_2$,[104,105] the shifting signals are given in Figure A1 and the resulting temperatures are given in Table A2. The NMR spectra were processed by left shifting the free induction decay (FID) to the top of the echo, followed by the application of 1000 Hz of exponential apodization. The chemical shifts were referenced to D_2O with $\delta_{iso}(^2H) = 4.8$ ppm. Simulations of the spectra taking into account different models for the dynamics were carried out using EXPRESS.[117] This software simulates a spectrum resulting from a motionally averaged NMR interaction tensor using a model consisting of discrete jumps between different sites at a given rate.

4.4 Results

4.4.1 Fully Sodiated Hard Carbon

To investigate the dynamics of co-intercalated diglyme molecules, hard carbon electrodes were fully sodiated to 5 mV in half-cells with a 1 M $NaPF_6$ in diglyme-d_{14} electrolyte. Static ^{2}H SSNMR spectra were then collected for these samples at a range of temperatures and simulations of the resulting spectra were performed to understand the dynamics of co-intercalated diglyme. These experiments were first performed on **B** as it is a commercially available hard carbon that has been previously studied with other techniques,[119,120] has a reasonably well understood structure, and it was the hard carbon used in the previous chapter. Furthermore, the specific capacity for the first sodiation of **B** is ~330 mAh g^{-1}, with the low voltage plateau corresponding to ~160 mAh g^{-1} (Figure 4-1), is typical of other commercial hard carbons.

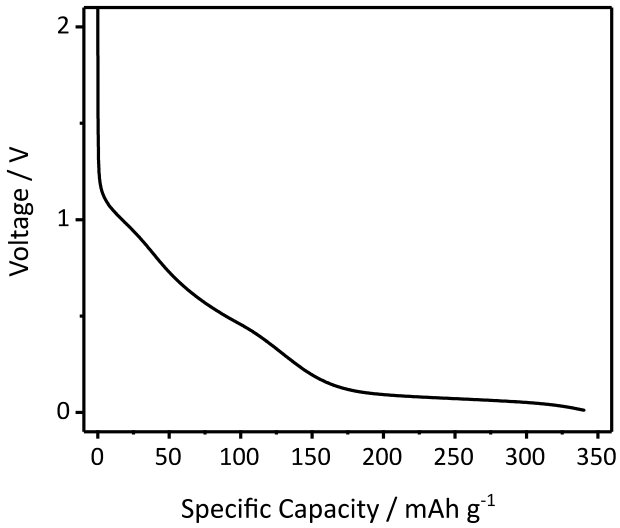

*Figure 4-1: Voltage profile of the first sodiation of **B** in a half-cell with a 1 M $NaPF_6$ in diglyme-d_{14} electrolyte, at a rate corresponding to C/20.*

Static VT ^{2}H NMR spectra of **B** are shown in Figure 4-2 (a). The low-temperature spectra consist of two overlapping powder patterns arising from the two different chemical environments in the diglyme molecule. Simulations of the low-temperature spectrum (183 K) enabled the determination of C_Q and η_Q, which were used as starting points for the simulation of the dynamics (*vide infra*). The narrower site was simulated with C_Q = 48(4) kHz and η_Q = 0.00(5) and is assigned to the deuterons in the terminal methyl groups (CD_3), as shown in Figure 4-2 (b) and (c). This relatively small value of C_Q is due to rotation of the methyl groups partially averaging out the quadrupole interaction. Simulation of the broader site was accomplished with C_Q = 170(5) kHz and η_Q = 0.00(5) and is assigned to the deuterons in the methylene groups (CD_2). Changing the temperature between 183 K and 227 K results in spectra that are all similar showing the typical ^{2}H Pake doublets and no changes in lineshape. This suggests that any additional (i.e., on top of the methyl group rotation which occurs with rates in the FML at this temperature) motion is either not happening or is occurring at rates in the SML. It is also worth noting that as the melting point of diglyme is 209 K,[63] so it is likely that the signal corresponds to diglyme in a constrained environment as free diglyme would appear as a sharp peak for all temperatures above 209 K. The spectra collected between 249 K and 337 K have a sharp peak around 0 ppm as well as the Pake doublets, the latter decreasing in relative intensity as the temperature is increased, indicating that the molecular motion is occurring with rates in the IMR to FML, where small changes in the rate of the motion have a drastic effect on the appearance of the powder pattern. Finally, the spectrum collected at 359 K consists of a single, sharp peak around 0 ppm, indicating that the molecular motion is occurring with rates in the FML, where any further increases in the rate of motion do not result in any further changes to the powder pattern.

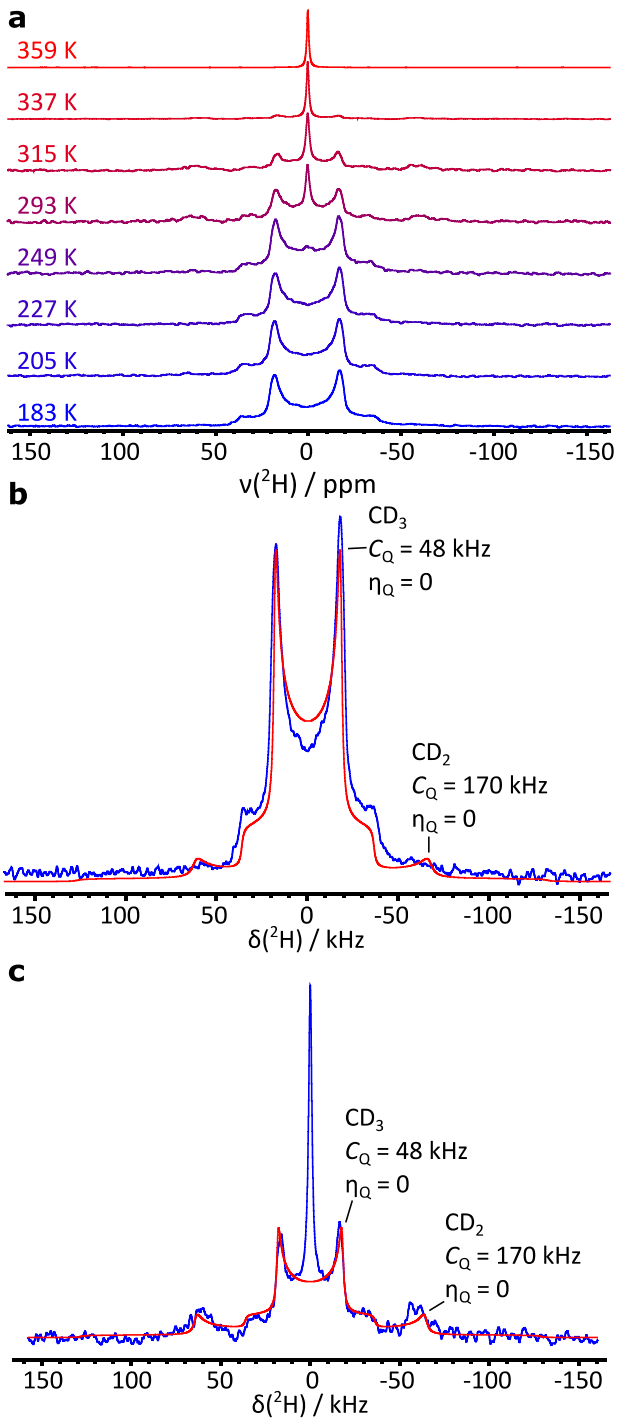

*Figure 4-2: (a) VT static ^2H SSNMR spectra of a **B** electrode fully sodiated (to 5 mV) with a 1 M $NaPF_6$ in diglyme-d_{14} electrolyte, dried under vacuum at temperatures ranging from 183 K to 359 K. Simulated spectra (red) overlaid of on the experimental spectra blue collected at (b) 183 K and (c) 315 K.*

To understand the temperature-dependent changes in the ^2H spectra, simulations of the dynamics of the diglyme molecules were undertaken. Due to a low sample mass and broad signals, there are low signal-to-noise ratios for the powder patterns corresponding to the CD_2 groups, making the simulation of the dynamics of these environments difficult; therefore, the simulations will focus on determining the dynamics of the terminal methyl groups. As methyl group rotation about the C_3 axis is

known to be fast in the solid state at relatively low temperatures,[121] the larger amplitude motions can be treated by manipulating the motionally averaged EFG tensor (V^{eff}) resulting from this motion. Figure 4-3 (a) shows the largest component of V^{eff} (V_{33}^{eff}) is co-linear with the C-O bond connecting the methyl group to the adjacent O atom.

As a first attempt to simulate the motion of diglyme, the model proposed by Gotoh *et al.*[102] was used. This model assumes that diglyme molecules coordinate to Na^+ through the central O atom and molecular rotation occurs about an axis that is colinear with the bond connecting the Na^+ ion and the central O of the diglyme (R_{mol}). A cone angle, β, is then defined as the angle between the R_{mol} and V_{33}^{eff}, as shown in Figure 4-3 (b). This motion is equivalent to modelling jumps between N sites on a cone. We note that using this model with rates in the FML for any $N > 3$ will result in the same motionally-averaged ^{2}H SSNMR powder pattern. This is demonstrated in Figure 4-3 (c) where three static ^{2}H spectra were simulated with N values of 4, 6 and 8, all with β = 70° and $\nu_{ex} = 10^9$ Hz (which corresponds to rates in the FML), and all three spectra are identical despite the different values of N.

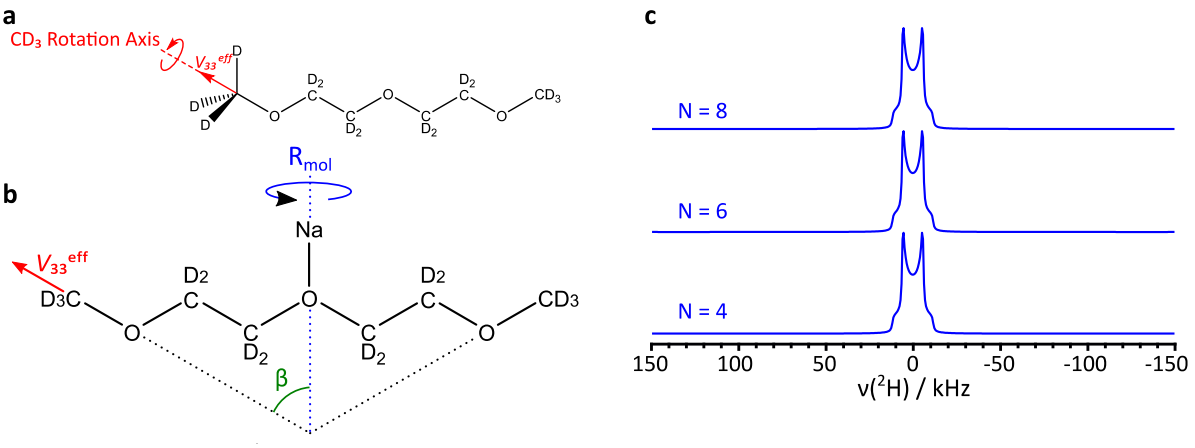

Figure 4-3: Schematic diagrams demonstrating (a) the orientation V_{33}^{eff} from methyl group rotation in relation to the rest of the diglyme molecule and (b) that β represents the angle between V_{33}^{eff} and R_{mol} . (c) Simulated ^{2}H spectra with constant values for ν_{ex} of 10^9 Hz and β of 70°, whilst N is varied between 4, 6 and 8.

In Gotoh's model, the value of β used for the methyl groups was 57.1°; this was derived by assuming linear diglyme molecules are rotating perpendicular to the molecular long axis, with an additional tilting angle of 10° between the C-O axis and the molecular rotation axis. Figure 4-4 (a) shows a simulated spectrum using β = 57.1°, N = 6 and $\nu_{ex} = 10^9$ Hz. This results in a relatively narrow Pake doublet, where the splitting of the horns is 10 kHz. This differs from the ^{2}H SSNMR spectra collected for **B**, where the spectrum collected at 359 K (motion with rates in the FML) has no discernible features of a Pake doublet and a single sharp peak is observed. It was therefore attempted to adapt Gotoh's model by modelling different values of β. This is shown in Figure 4-4 (b), where simulations were performed with N = 6 and $\nu_{ex} = 10^9$ Hz. As β is increased from 45°, the simulated patterns narrow, until the spectrum simulated with β = 55° gave a single sharp peak that matched well with the shape of

the room temperature experimental spectrum (as shown in Figure 4-4 (c)). Increasing β beyond 55° results in spectra that broaden again such that the features of the Pake-doublet pattern are clearly visible.

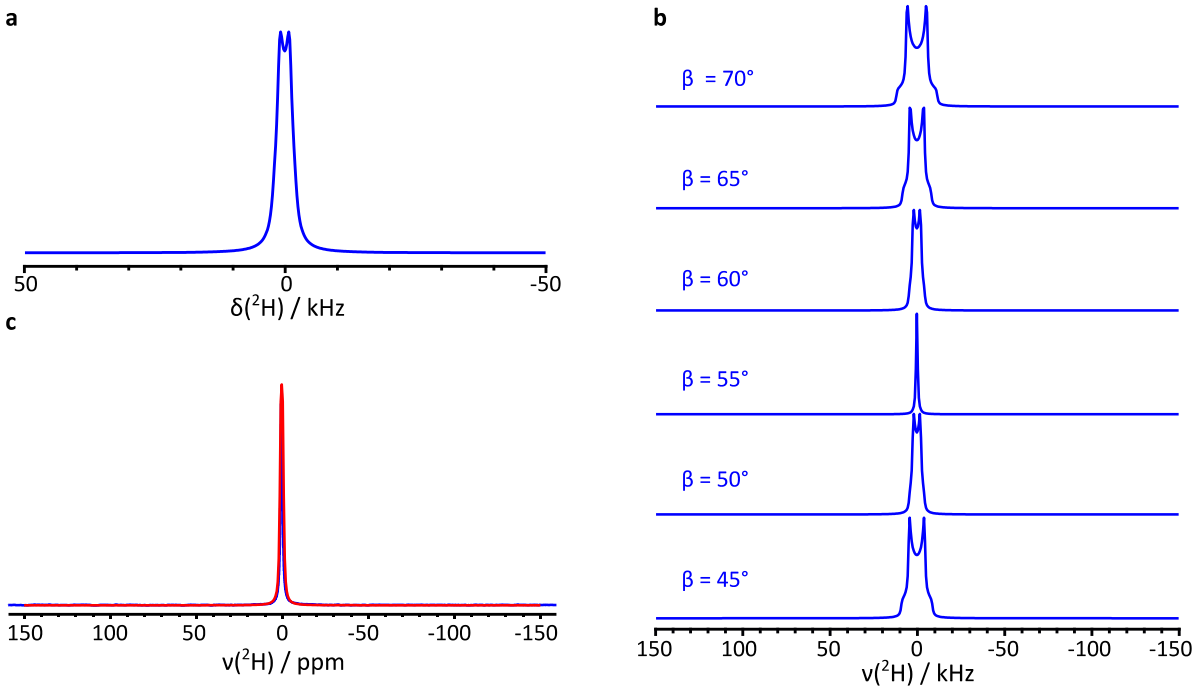

Figure 4-4: (a) A simulated static ^2H SSNMR spectrum with N = 6, $v_{ex} = 10^9$Hz and β = 57.1°, (b) simulated ^2H spectra with a constant values for v_{ex} (10^9 Hz) and N (6), whilst β is varied between 45° and 70° and (c) a simulated ^2H NMR spectrum (β = 55° and $v_{ex} = 10^9$ Hz) (red trace) overlaid on the experimental spectrum collected at 359 K (blue trace)..

Whilst this model simulates the motion of the terminal methyl groups, it does not consider the motion of the CD_2 groups, the horns of which would still be expected to be seen in the spectrum collected at 359 K if molecular rotation is occurring according to Gotoh's model as the cone angle for these groups will not be the same as for the methyl groups. However, these horns are not observed at 359 K, which suggests that the motion of diglyme molecules within the hard carbon is isotropic. The effect of isotropic motion on the appearance of ^2H power patterns can be approximated for the methyl groups using a simple rotational model with β = 55° (which is close to the magic angle). This simplifed model was used to fit the ^2H powder patterns for the methyl groups at all temperatures in order to extract information about the rates of motion. To simulate the spectrum collected at 293 K, the rate of rotation was decreased to between 5×10^4 Hz and 8×10^4 Hz (Figure 4-5 (a)). While the simulated spectra show the same features as the experimental pattern (i.e., a sharp central peak and a set of horns), the relative intensities of these features do not match those of the experimental data. This suggests that at 293 K, the isotropic motion cannot be approximated by molecular rotation with a *single* rate. Therefore, a lognormal distribution of v_{ex} centred on 1.8×10^4 Hz, with a full width half maximum (FWHM) = 4 orders of magnitude (as shown in Figure 4-5 (b)) was considered. The resulting intensities of the features in the simulated spectrum, Figure 4-5 (c), now coincide with the experimental spectrum. To validate that this model is representative of the motions occurring at other temperatures, a similar pattern was

modelled for the spectrum collected at 315 K (which also corresponds to motion in the IMR) (Figure 4-5 (d)). For this spectrum, a good fit was achieved with a similar lognormal distribution of ν_{ex} centred on 3.0×10^4 Hz with a width at FWHM of 4 orders of magnitude. We note that whilst this is a simplified model, it reasonably approximates the more complex motion that is likely occurring for diglyme molecules intercalated in hard carbon.

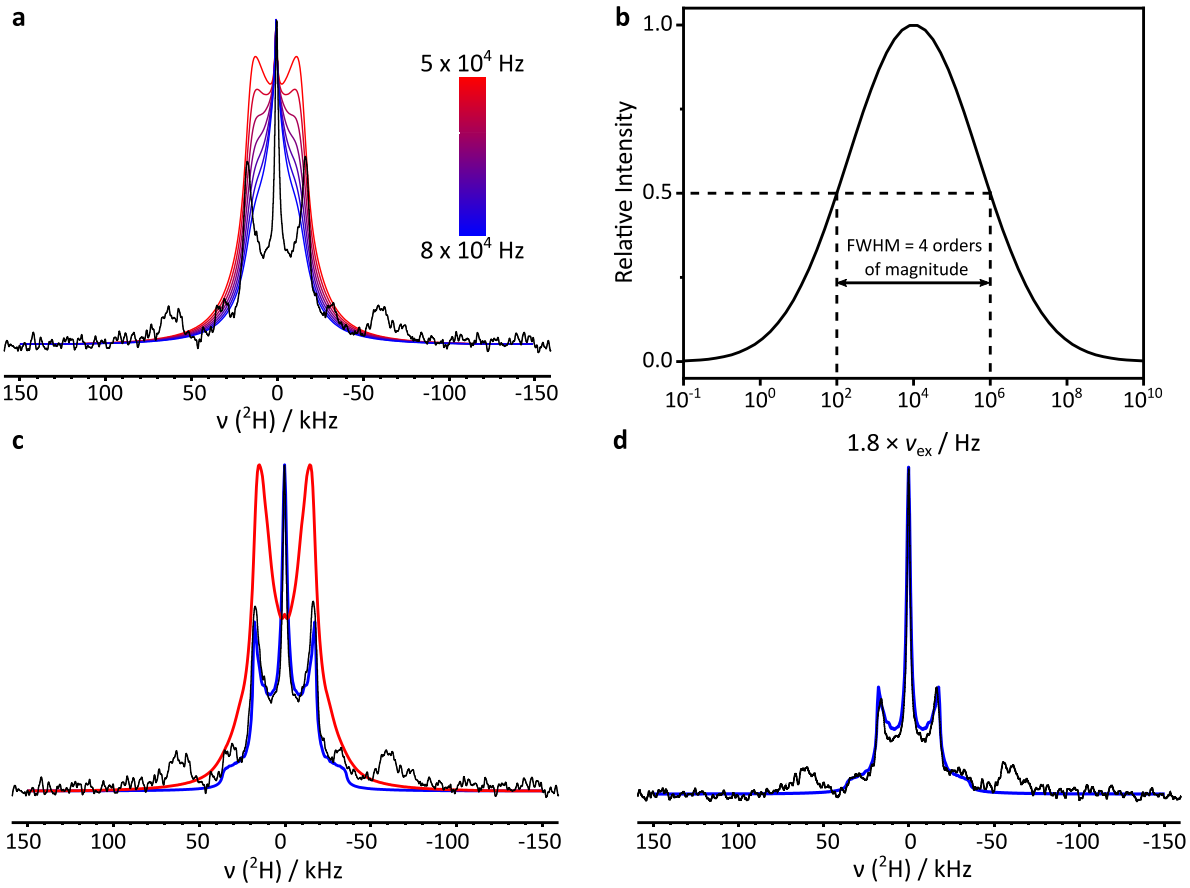

*Figure 4-5: (a) Simulated static ^{2}H SSNMR spectra with a constant β of 55° and ν_{ex} varied between 5×10^4 Hz and 8×10^4 Hz (red to blue) overlaid over the real static ^{2}H SSNMR spectrum collected for **B** at 293 K (black). (b) A lognormal distribution of ν_{ex} centred on 1.8×10^4 Hz with a width at FWHM of 4 orders of magnitude. (c) Simulated static ^{2}H SSNMR spectra with β = 55° and a constant $\nu_{ex}^{rot} = 1.8 \times 10^4$ Hz (red) or a lognormal distribution of ν_{ex} (centred on 1.8×10^4 Hz, with a width at FWHM of 4 orders of magnitude) (blue), overlaid on the experimental static ^{2}H SSNMR spectrum of **B** collected at 293 K (black). (d) A simulated static ^{2}H SSMR spectrum with β = 55° and a lognormal distribution of ν_{ex} (centred on 3.0×10^4 Hz, with a width at FWHM of 4 orders of magnitude) (blue), overlaid on the experimental static ^{2}H SSNMR spectrum of **B** collected at 315 K.*

4.4.2 Intermediate States of Charge

To investigate the behaviour of co-intercalated diglyme molecules at intermediate SOCs, VT ^{2}H SSNMR data sets were collected for **B** electrodes that were sodiated to 600 mV, 200 mV and 60 mV. These SOCs are shown in Figure 4-6 (a), 600 mV (blue) corresponds to halfway along the sloping voltage region, 200 mV (red) corresponds to the bottom of the slope and 60 mV (green) is roughly halfway along the low voltage plateau.

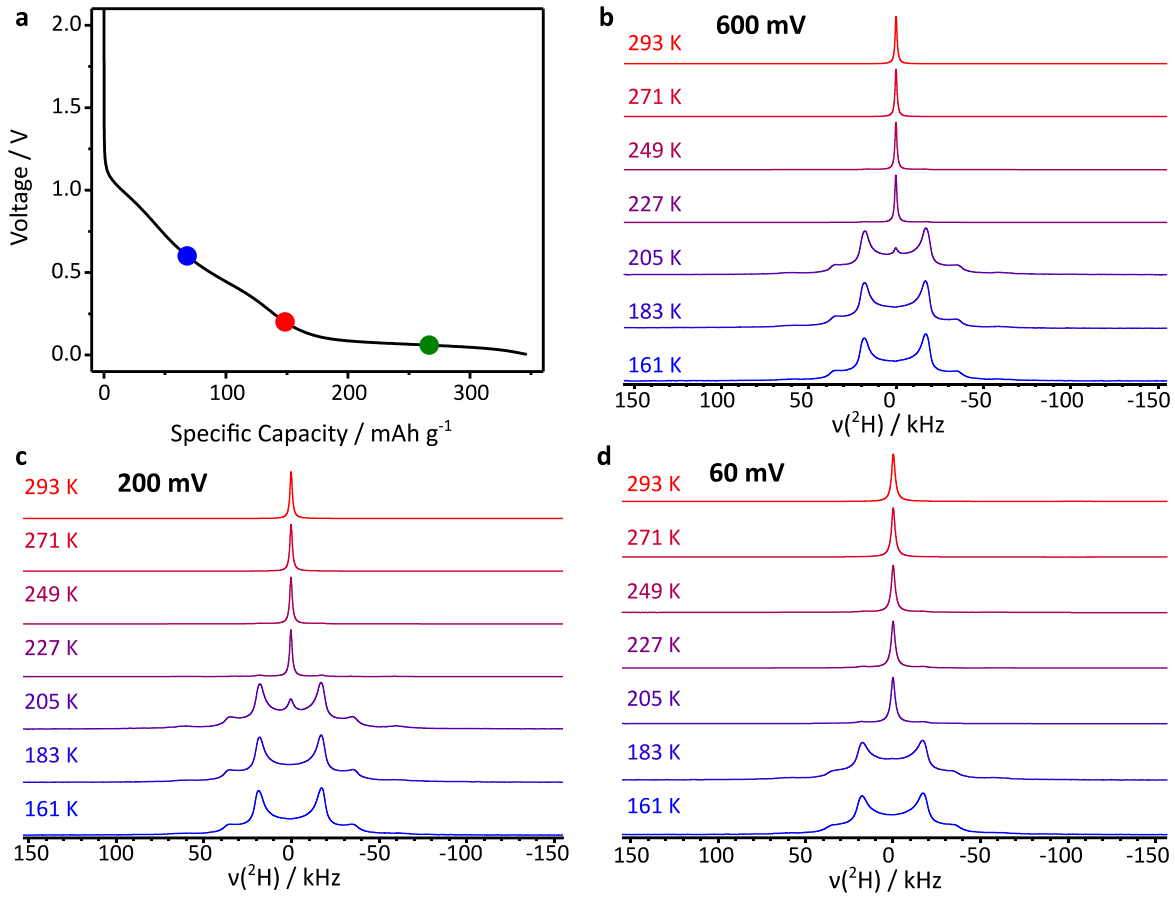

*Figure 4-6: (a) A voltage profile for the first sodiation of a **B** in a half-cell sodiated to 5 mV, with a 1 M $NaPF_6$ in diglyme-d_{14} electrolyte, at a rate corresponding to C/20, with 600 mV (blue), 200 mV (red) and 60 mV (green) highlighted, and a comparison of the VT ^2H SSNMR data sets for **B** electrodes sodiated to (b) 600 mV, (c) 200 mV and (d) 60 mV with a 1 M $NaPF_6$ in diglyme-d_{14} electrolyte. All three samples were dried before acquiring the spectra.*

The full ^2H SSNMR data sets for hard carbon electrodes sodiated to 600 mV, 200 mV and 60 mV are given in Figure 4-6 (b), (c) and (d), respectively. As before, the low temperature spectra (161 K) consist of overlapping Pake doublets from the CD_3 and CD_2 groups, and the large-amplitude motions of the diglyme molecules is occurring with rates in the SML. As the temperature is increased, a central, sharp peak begins to emerge, which corresponds to fast moving diglyme molecules, and eventually becomes the dominant feature of the spectra. For the samples sodiated to the slope (600 mV and 200 mV), this transition occurs between 205 K and 227 K, whereas for the sample sodiated to 60 mV (on the plateau), this transition occurs between 183 K and 205 K, which indicates a greater degree of mobility for diglyme in this sample.

To confirm this trend, the spectra were fitted with the same model previously described for fully sodiated hard carbon electrodes (example simulations of ^2H spectra collected at 205 K are given in Figure 4-7). The resulting central frequencies of the lognormal distributions of ν_{ex} are given in Table 4-1. The motion is occurring at rates in the SML at 161 K, where all spectra can be fitted with a lognormal distribution of ν_{ex} centred on 1.0×10^2 Hz, and at 293 K all motion is in the FML, which can

be fitted with a lognormal distribution of ν_{ex} centred on 1.0×10^7 Hz. For the intermediate temperatures, the rate of rotation increases for all samples as temperature increases. However, the 600 mV and 200 mV samples undergo a noticeable transition from motion on the order of 10^2 Hz to 10^5 Hz between 205 K and 227 K, whereas this transition occurs at a lower temperature of between 183 K and 205 K for the 60 mV sample. This indicates that the motion of diglyme is significantly higher when hard carbon has been sodiated to the plateau, possibly indicating an expansion of hard carbon structure (i.e., an increase in the spacing between the graphene sheets).

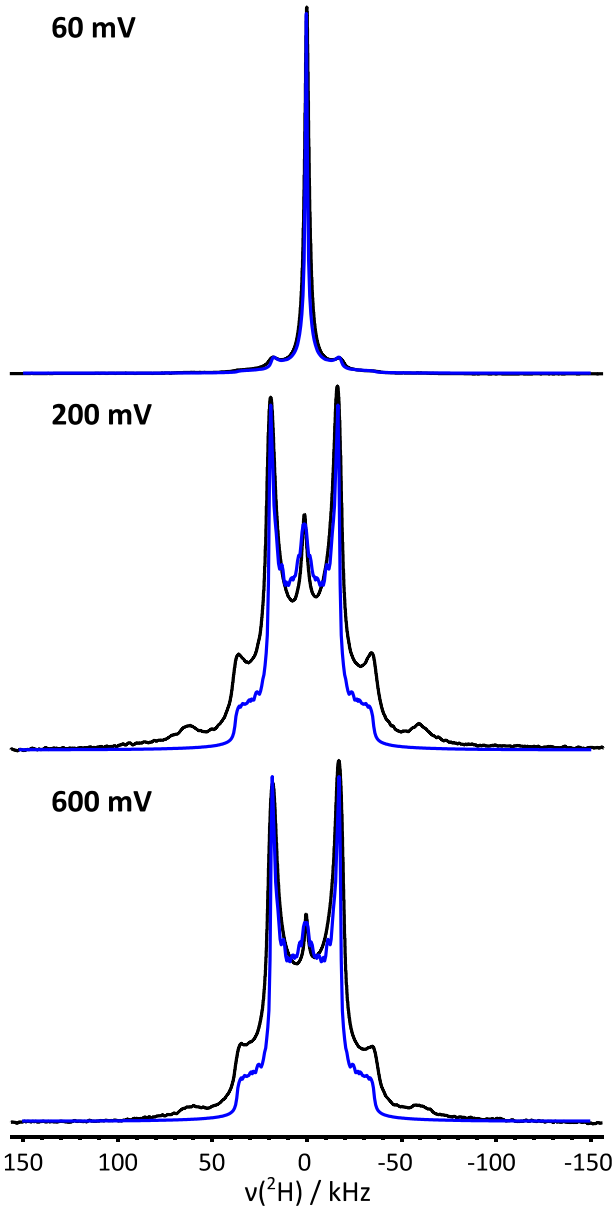

Figure 4-7: Simulated static ^{2}H SSNMR spectra (blue) overlaid on the experimental static ^{2}H SSNMR spectra (black) for hard carbon sodiated to 60 mV, 200 mV and 600mV colleceted at 205 K.

*Table 4-1: Centre frequencies the lognormal distributions of ν_{ex} used to fit the VT static ^2H SSNMR spectra of **B**, sodiated to 600 mV, 200 mV and 60 mV. The data showing the increased mobility of the 60 mV sample over the 600 and 200 mV samples is highlighted in blue.*

Temperature / K	Centre Frequency / Hz		
	600 mV	**200 mV**	**60 mV**
293	1.0×10^7	1.0×10^7	1.0×10^7
271	1.0×10^7	1.0×10^7	1.0×10^7
249	5.0×10^5	5.0×10^5	3.0×10^5
227	3.0×10^5	2.0×10^5	2.0×10^5
205	4.0×10^2	5.0×10^2	1.0×10^5
183	1.0×10^2	1.0×10^2	4.0×10^2
161	1.0×10^2	1.0×10^2	1.0×10^2

As these data sets were collected on samples that were not vacuum dried, care must taken when comparing to the results for **B** fully sodiated (to 5 mV), as this electrode was dried under vacuum, which could remove any weakly adsorbed (and possibly more mobile) diglyme. However, Figure 4-8 shows spectra from all four SOCs collected at 205 K, as this temperature displays the greatest difference between the spectra**.** All spectra appear to show two overlapping features, a Pake doublet and a sharp central peak (and for the 200 mV and 600 mV spectra, horns corresponding to the -CD_2- groups are also visible at approximately ± 60 kHz). Whilst the spectra collected for 600 mV (blue trace) and 200 mV (red trace) are similar, albeit with a slightly higher intensity central peak for 200 mV, indicating more motion, there is a significant change to 60 mV (green trace) where the central peak dominates the spectrum. This suggests that on increased sodiation, diglyme becomes increasingly more mobile. The spectrum for the sample sodiated to 5 mV consists only of a Pake doublet, without a central sharp peak, indicating reduced mobility of diglyme. Whilst this is likely due to vacuum drying removing more mobile diglyme, it is also possible that mobility reduces at full sodiation due to steric hinderance from the increased amount of diglyme and Na within the hard carbon.

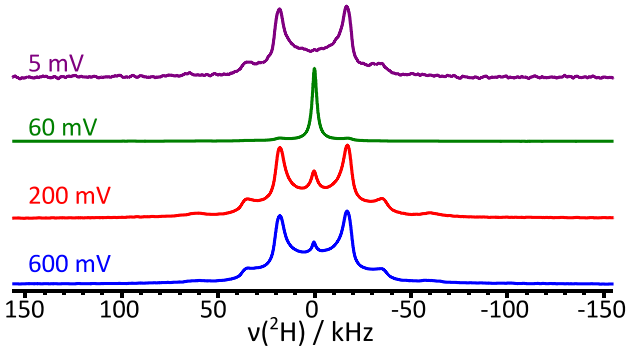

*Figure 4-8: Static ^2H SSNMR spectra collected at 205 K for electrodes of **B** sodiated to 600 mV (blue trace), 200 mV (red trace) and 60 mV (green trace), with a 1 M $NaPF_6$ in diglyme-d_{14} electrolyte that were not vacuum dried.*

4.4.3 Hard Carbons with Different Specific Capacities

To relate the motion of diglyme to the capacity of the hard carbon, two other hard carbons were analysed in a similar way to **B**. These carbons were fully sodiated (to 5 mV) and dried under vacuum prior to analysis. The first of these, **A**, has a low capacity (the first sodiation has a specific capacity of ~280 mAh g^{-1}, where the low voltage plateau corresponds ~80 mAh g^{-1}) and the second, **C**, has a higher first cycle specific capacity of ~450 $mAhg^{-1}$, where the low voltage plateau corresponds to ~350 mAh g^{-1}. Voltage profiles of the first sodations of these materials are given in Figure 4-9 (a). Structural information about these carbons has been provided using several different techniques:[33,116] **A** is relatively disordered with minimal long-range order. A combination of small angle neutron scattering (SANS) and small angle X-ray scattering (SAXS) showed it has a relatively large interlayer spacing (d_{002} = 3.9 Å) and small pores (~1 nm in diameter).[33] Conversely, it was shown using a combination of X-ray diffraction (XRD) and Raman spectroscopy that **C** has higher amount of order and increasingly graphitic domains that enable the material to have larger pores.[116] This effect is shown in Figure 4-9 (b), which shows MAS ^{23}Na SSNMR for **A**, **B** and **C** fully sodiated to 5 mV. For **A** there is no quasi-metallic peak, **B** has a broad quasi-metallic peak at 750 ppm that indicates pore filling has occurred and **C** has a broad peak at 1100 ppm that aligns with the expected shift of Na metal, indicating larger (and hence more metallic) pools of Na metal form in the pores of the carbon.

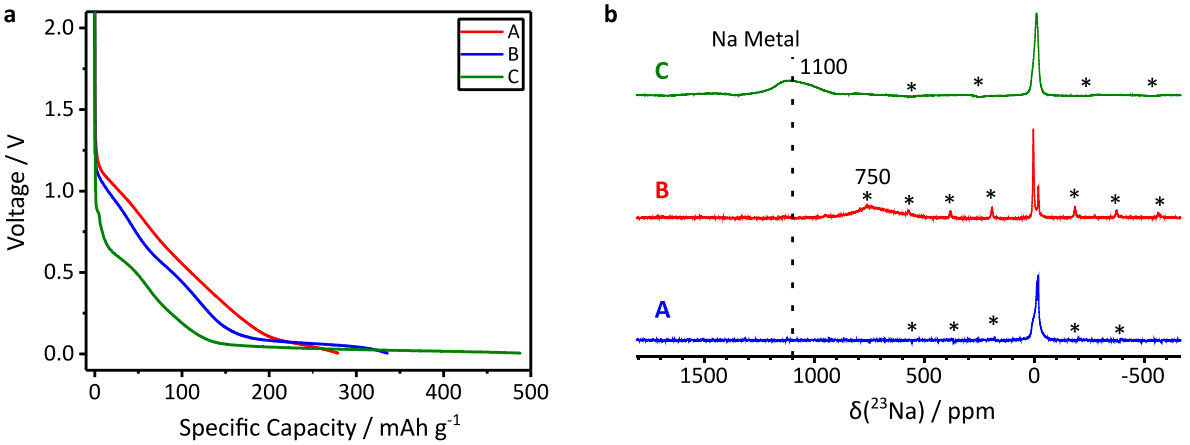

*Figure 4-9: (a) Voltage profiles corresponding to the first sodiations of **A** (red trace), **B** (blue trace) and **C** (green trace) in half-cells with a 1 M $NaPF_6$ in diglyme-d_{14} electrolyte, at rates corresponding to C/20. ^{23}Na MAS SSNMR of hard carbons **A** (blue trace), **B** (green trace) and **C** (red trace) fully sodiated to 5 mV. **A** and **B** were sodiated with a 1 M $NaPF_6$ in diglyme electrolyte and spectra were collected at 25 kHz MAS with a 11.7 T magnet. **C** was sodiated with 1 M $NaPF_6$ in EC:DMC electrolyte and the spectrum was collected at 50 kHz MAS with a 16.4 T magnet.*

The full VT ^{2}H SSNMR data sets for fully sodiated electrodes of each hard carbon are given in Figure 4-10. All spectra show Pake doublets at low temperatures (183 K and 205 K), and a single sharp peak forming at 359 K. However, the intermediate temperatures show that as the capacity of the hard carbon increases, the motion of diglyme decreases. For example, all spectra show Pake doublets for the

low temperatures (183 K and 205 K), but for **A**, the central peak begins to emerge at 227 K, compared to 249 K for **B** and **C**.

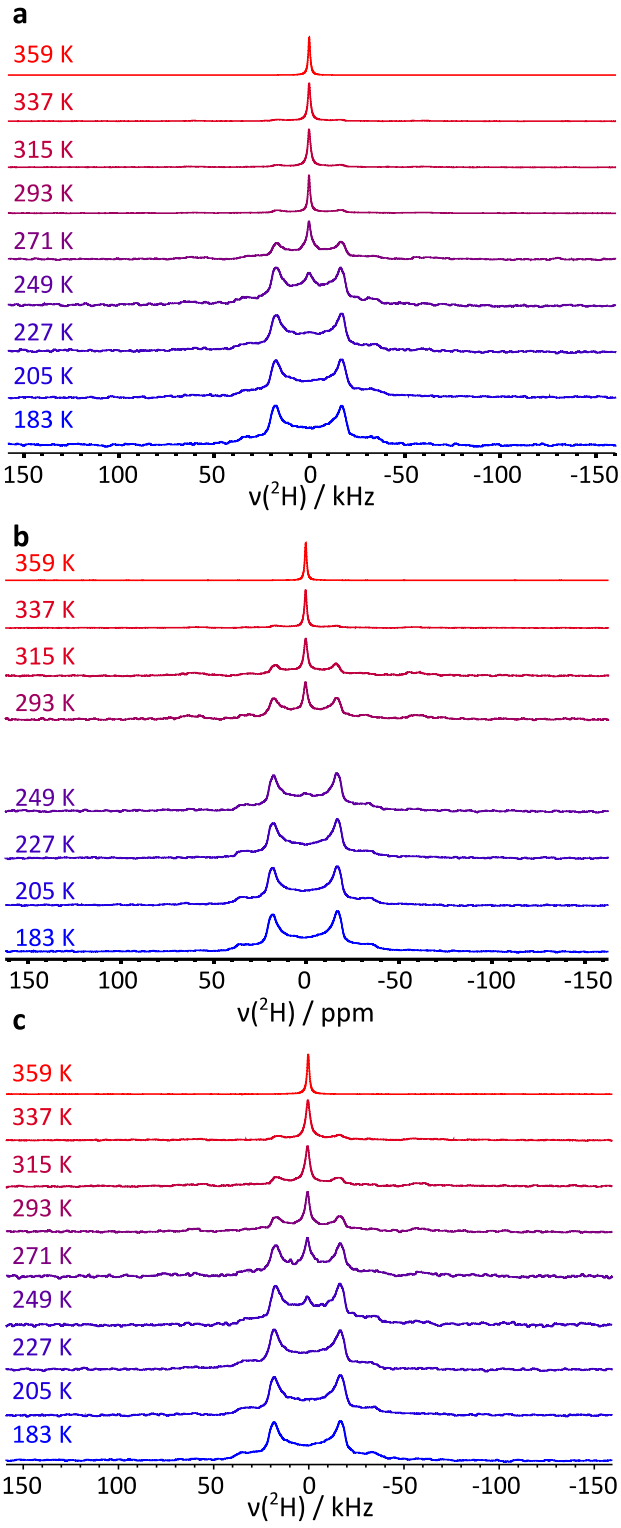

Figure 4-10: A comparison of the VT ^{2}H SSNMR data sets for carbons A, B and C, (a), (b) and (c), respectively, all fully sodiated to 5 mV with a 1 M $NaPF_6$ in diglyme-d_{14} electrolyte.

This effect is highlighted in Figure 4-11, which shows static ^{2}H SSNMR spectra for all three carbons collected at 293 K. In this figure, the central sharp peak (which corresponds to fast moving diglyme) dominates the spectrum for **A**, whereas for **B** and **C** the intensity of the horns (which corresponds to slow moving diglyme molecules) is higher, indicating that diglyme is moving more slowly for these samples. This was verified by simulating spectra using the model outlined above for **B**. The resulting centre frequencies of the lognormal distributions of rates are given in Table 4-2 (example simulations of ^{2}H spectra collected at 293 K are given in Figure 4-12). For the spectra collected at 359 K, where motion is exclusively at rates in the FML, all spectra can be fitted with lognormal distributions of ν_{ex} centred on 1.0×10^{8} Hz. Likewise, at 183 K when all motion is exclusively at rates in the SML, all spectra can be fitted with lognormal distributions of ν_{ex} centred on 5.0×10^{1} Hz. For the intermediate temperatures, when ν_{ex} distributions are at least partly in the IMR, the motion of **A** is significantly higher than **B**, which is roughly equal to that of **C**.

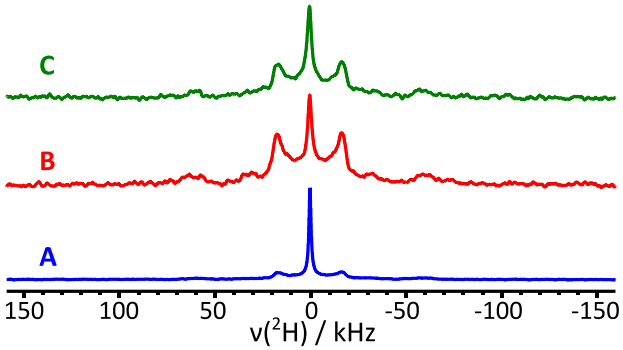

*Figure 4-11: Static ^{2}H SSNMR spectra collected at 293 K for electrodes of **A** (blue), **B** (red) and **C** (green), fully sodiated to 5 mV with a 1 M $NaPF_6$ in diglyme-d_{14} electrolyte that were dried under vacuum.*

*Table 4-2: Centre frequencies the lognormal distributions of ν_{ex} used to fit the VT ^{2}H SSNMR spectra of **A**, **B** and **C** fully sodiated to 5 mV. The data showing the increased mobility of **A** over **B** and **C** is highlighted in blue.*

Temperature / K	**Centre Frequency / Hz**		
	A	**B**	**C**
359	1.0×10^{8}	1.0×10^{8}	1.0×10^{8}
337	1.5×10^{5}	6.0×10^{4}	1.0×10^{4}
315	6.0×10^{4}	3.0×10^{3}	4.0×10^{3}
293	2.0×10^{4}	1.8×10^{3}	2.5×10^{3}
271	2.0×10^{3}	-	1.1×10^{3}
249	7.0×10^{2}	3.0×10^{2}	5.5×10^{2}
227	3.0×10^{2}	1.0×10^{2}	1.5×10^{2}
205	1.5×10^{2}	5.0×10^{1}	5.0×10^{1}
183	5.0×10^{1}	5.0×10^{1}	5.0×10^{1}

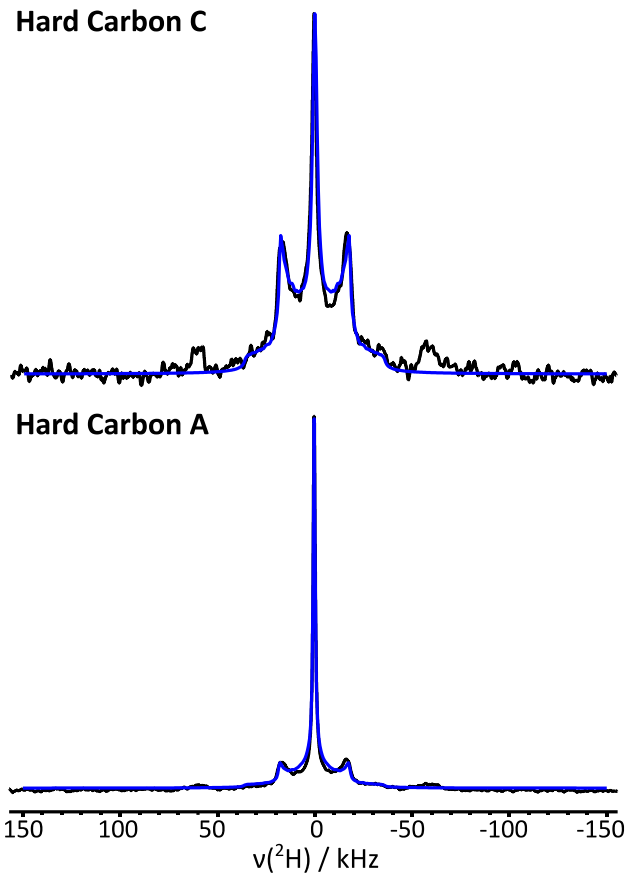

*Figure 4-12: Simulated static ^2H SSNMR spectra (blue) overlaid on the experimental static ^2H SSNMR spectra (black) for hard carbons **A** and **C** fully sodiated to 5 mV collecteted at 293 K.*

4.5 Discussion

VT SSNMR ^2H spectra of diglyme chemically co-intercalated into graphite were previously reported by Gotoh *et al.*[102] At low temperatures (123 K and 173 K) these spectra show powder patterns that indicate that there is no motional averaging. For both spectra, there are two components with C_Q values of 50 kHz and 165 kHz, which correspond to the CD_3 and CD_2 groups, respectively. A C_Q value of 50 kHz is narrower than expected for a C-D bond, which indicates that these deuterons are not static and the spectral narrowing is due to methyl group rotation. For the CD_2 groups, a C_Q of 165 kHz is typical for C-D bonds in alkyl groups, so there is no additional motion for these groups. This indicates that the diglyme molecules are rigidly coordinated to the Na^+ ion. As the temperature is increased to 293 K, significant narrowing of the powder patterns occurs, but the features of the Pake doublets are still resolved. In this model, diglyme is tightly coordinated to diglyme though all three O atoms at low temperatures and the only motion present is rotation of the terminal methyl groups. As the temperature is increased diglyme, becomes more loosely bound to Na and it begins to rotate around the central O-Na^+ bond (the molecular rotation axis).

When hard carbon electrodes are sodiated with a standard carbonate electrolyte, two regions are commonly observed in the electrochemical voltage profiles: a slope and a plateau near 0 V. The sloping process is assigned to Na^+ ions being stored at defects, between the carbon layers, and on pore surfaces. The plateau process is assigned to pore filling where quasi-metallic Na clusters are formed, the size and shape of which is determined by the pore structure of the hard carbon.[39] When hard carbon is sodiated with a diglyme electrolyte, similar regions are observed in the voltage profile, indicating that similar electrochemical processes are occurring; for example, it is known from the ^{23}Na SSNMR in the last chapter that pore filling still occurs as quasi-metallic Na species are observed. However, a small, but not insignificant, amount of Na that intercalates into hard carbon with diglyme and the dynamics of these species can be analysed by SSNMR.

For fully sodiated (to 5 mV) hard carbon (**B**), the low temperature (183 K – 227 K) ^2H SSNMR spectra also show relatively broad powder patterns, again indicating that diglyme is rigidly held to Na^+. As the temperature is increased, the horns of the Pake doublets start to decrease in intensity and by 249 K, a sharp peak is observed in the centre of the spectrum. This peak then becomes more prominent such that by 359 K it is the only feature of the spectrum. It was attempted to simulate this motion using the model proposed by Gotoh *et al.*[102] It was found that the single sharp peak at 359 K could be fitted by using a modified version Gotoh's model where the angle between the rotating methyl groups and the molecular rotation axis 55° (as opposed to 57.1°). It was then attempted to model the motion of the terminal methyl groups at intermediate temperatures (293 K and 315 K), and it was found that to achieve a good fit, the molecular rotation model had to be adapted by adding a lognormal distribution of rotation rates, which is indicative of the greater degree of disorder in hard carbon compared to graphite, and the range of different sites that Na-diglyme complexes can occupy in hard carbon. Whilst this model describes the motion of the terminal methyl groups well, it does not work for the CD_2 groups. It is therefore likely that isotropic motion of diglyme is occurring, but the motion of the terminal methyl groups can be approximated by modelling molecular rotation of diglyme, with a lognormal distribution of rotation rates. The assumption of isotropic motion of the diglyme molecules is reasonable as compared to graphite, hard carbons have larger spacings between the carbon sheets, as well as pores of varying sizes and shapes, which means there is greater amount of space for diglyme to move in.

It was next attempted to investigate the behaviour of intercalated diglyme at intermediate SOCs. To do this, a series of static VT ^2H SSNMR spectra were also collected for **B** electrodes sodiated to 600 mV, 200 mV and 60 mV. As these samples were not vacuum dried, they will have more unconstrained diglyme molecules which are more mobile at lower temperatures, this diglyme could be surface adsorbed or possibly intercalated into hard carbon and only partially bound to Na^+. However, a trend is still observed for these electrodes. The diglyme co-intercalated into electrodes sodiated to the slope (600 mV and 200 mV) have a broadly similar degrees of motion, there is then a significant increase in the motion of diglyme for 60 mV (part way along the plateau). This suggests that when hard carbon is

sodiated to the plateau, diglyme molecules have more space to move; this could be due to hard carbon expanding or by diglyme molecules migrating to the pores of the material.

Whilst the fully sodiated sample was dried and may not be directly comparable, as some co-intercalated diglyme could be removed under vacuum, it does appear to show a decrease in the mobility of diglyme. One explanation for this could be that at full sodiation, there is an increase in steric hinderance limiting the motion. This could be because there is more co-intercalated diglyme between the carbon layers or because the pores are now filled with quasi-metallic Na, reducing the available space for large amplitude motion of the diglyme molecules, these effects are illustrated in Figure 4-13 below.

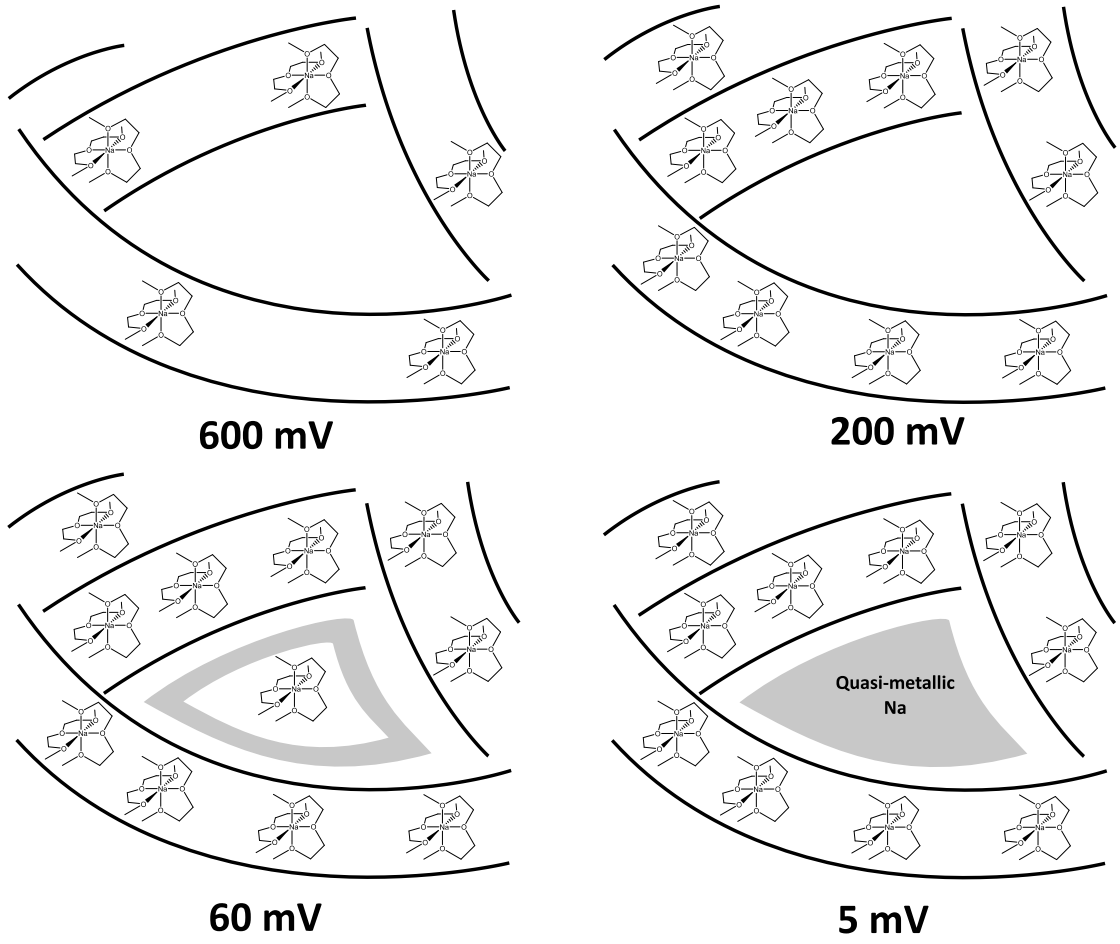

Figure 4-13: Schematics showing possible changes that occur during the co-intercalation of Na-diglyme into hard carbon at different SOCs.

Hard carbon **B** was also compared to two other hard carbons: **A** and **C**. **A** is a relatively disordered hard carbon, with a low specific capacity, where there is minimal contribution from the plateau close to 0 V. Due to its disorder, it has a greater distribution of environments for intercalation, with a larger interlayer spacing and limited porosity. The latter of these is evidenced by ^{23}Na SSNMR where a quasi-metallic signal is not observed for a fully sodiated **A** electrode, which indicates that there

is minimal pore filling. **C** is a more graphitic (and therefore less disordered) hard carbon, it has a higher specific capacity and a greater proportion of the capacity corresponds to the plateau. It has larger pores as evidenced by ^{23}Na SSNMR which shows that the quasi-metallic peak has shifted to that expected for more metallic Na species.

VT ^{2}H SSNMR spectra were collected for all hard carbons at full sodiation (5 mV). It was found that the intercalated diglyme had higher mobility for **A**, whereas **B** and **C** were roughly equal. One explanation for this could be that for fully sodiated **B** and **C** the interlayer spacing is limited and the pores are filled with quasi-metallic Na, together these effects mean there is limited space for diglyme to move, hence low mobility. Whereas **A**, is a lower capacity carbon, with fewer internal pores that Na can occupy and larger interlayer spacings that accommodate Na-diglyme complexes, this differences are highlighted in Figure 4-14 below. This means overall less Na intercalates into the material but there is greater mobility the diglyme that is intercalated. Therefore, the dynamics of co-intercalated diglyme molecules can therefore be used an indirect probe of the structure of different hard carbons.

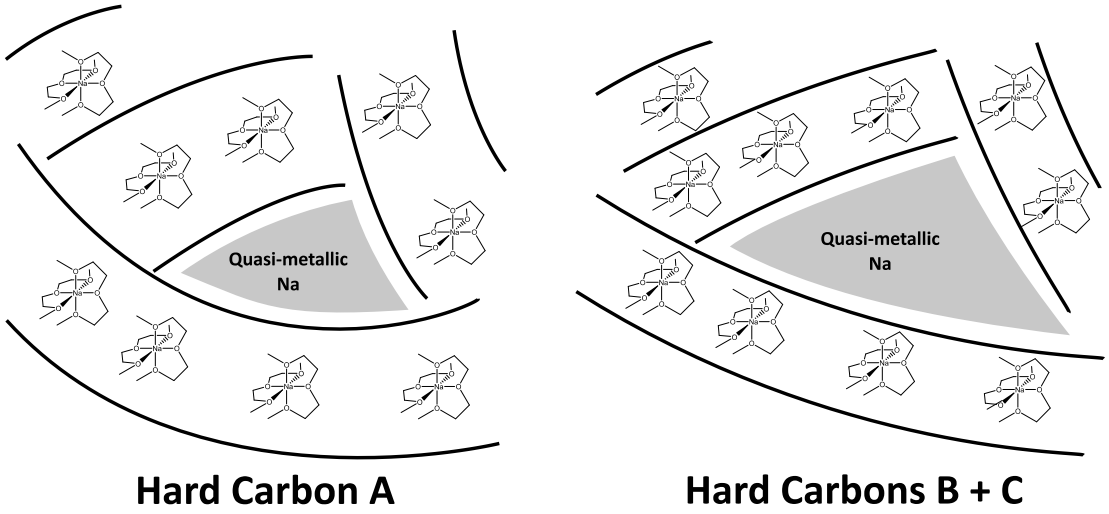

*Figure 4-14: Schematics showing the differences between hard carbon **A** with hard carbons **B** and **C**.*

4.6 Conclusion

We have studied the dynamics of diglyme co-intercalated into different hard carbons. For **B** (which has a first cycle capacity of ~350 mAh g^{-1}), the static VT ^{2}H NMR spectra collected showed three different motional regimes. At low temperatures from 183 K to 227 K Pake doublets from the terminal methyl groups are observed, which do not narrow with increasing temperature, which indicates that molecular motion is occurring with rates in the SML, however intramolecular motion, such as methyl group rotation is still probably occurring in the FML. For spectra collected between 249 and 337 K, the Pake doublets begin decrease in intensity with increasing temperature and a single isotropic signal is observed in the centre of the spectrum. This suggests that a distribution of rates for molecular motion is present, with some motion in the FML and some in the SML, with some motion possibly in

the IMR. Finally, at 359 K a single, isotropic signal is observed, which suggests that all motion is in the FML. Due to a limited signal to noise ratio, only the motion of the CD_3 groups was modelled. The molecular motion of diglyme was first modelled as six-fold rotation around a cone, where the rotation axis is co-linear with the Na-O bond. At 359 K, this simple rotational model provided a good fit for the data, however for lower temperatures this model did not provide a good fit. Therefore, some additional motion is required to fit the spectra and it was found that a lognormal distribution of jump rates produced a good fit. Whilst this is a simplistic model, it captures the more complex (probably isotropic) motion of diglyme that is actually occurring. By collecting ^2H SSNMR spectra at intermediate SOCs, it was found that as the degree of sodiation was increased, the mobility of diglyme increases on the slope indicating that diglyme has expanded or that diglyme has migrated to the pores of the material. Additionally, when different hard carbons were compared, it was found that as the capacity of the hard carbon used increased, the motion of diglyme increased, which is indicative of the higher capacity carbons becoming increasingly graphitic.

We therefore have shown that co-intercalated diglyme can be used as an indirect probe of the hard carbon structure, which could lead to a better understanding of the improved rate performance exhibited by using ether-based electrolytes.

5 Characterising the SEI formed in Full- and Half-Cells

5.1 Abstract

The SEI is of crucial importance to the performance of a NIB, yet its structure and composition are not fully understood. Previous studies to analyse the SEI formed on hard carbon in NIBs often use half-cells where Na metal is the counter electrode, as opposed to full-cells where a high voltage cathode such as a transition metal oxide is used, even though Na metal is a strong reducing agent and will reduce the electrolyte itself and likely influence the SEI formed via cross-talk reactions. This study sets out to analyse the differences in the SEI formed on hard carbon anodes in full- and half-cells. Three techniques were used to study these electrodes: SSNMR, XPS and solution NMR. SSNMR revealed that NaF is a major component of the SEI and that it is more prominent for half-cells, especially on initial cycling. The surfaces of the electrodes were studied in more detail using XPS, it was found that along with NaF, $NaPO_2F_2$ is an SEI component and that there is considerably more organic or polymeric SEI formed on hard carbon in half-cells, compared to full-cells. Solution NMR found that whilst all cells contained some electrolyte degradation products such as Na ethylene dicarbonate (NEDC), there was more electrolyte degradation for half-cells, especially after long term cycling, with species such as Na ethylene monocarbonate (NEMC) being the more dominant soluble degradation product.

5.2 Introduction

As a NIB (or LIB) is cycled, a solid layer builds up from electrolyte degradation products at the interface between the anode and the electrolyte. This layer is called the solid electrolyte interphase (SEI) and it is of crucial importance to the performance of the battery as it prevents further electrolyte degradation (and therefore capacity loss) by being an electronic insulator. However, the SEI needs to be an ionic conductor to allow for the diffusion of Na^+ ions. It is also important that the SEI is insoluble in the electrolyte, otherwise continual addition and removal of SEI would expose the active surface of the electrode, leading to further parasitic reactions, continual electrolyte degradation (consuming Na^+ if the degradation products precipitate out as salts) and ultimately, capacity loss and a poor electrochemical performance.

Techniques often used to study the SEI in LIBs include X-ray photoelectron spectroscopy (XPS),[122] scanning electron microscopy (SEM),[123] Fourier-transform infrared spectroscopy (FTIR),[124] X-ray absorption spectroscopy (XAS)[125] and surface enhanced Raman spectroscopy (SARS).[126] To study soluble electrolyte degradation products, solution NMR is commonly used.[127] Of these techniques, XPS and FTIR are the most commonly employed and using them Peled *et al.*[73] proposed the "mosaic" model of the SEI. In this model, there is a layer of crystalline inorganic components, such as LiF, Li_2O and Li_2CO_3, closer to the surface of the electrode and a second, more diffuse layer of organic or polymeric species, such as polyolefins and semicarbonates, closer to the electrolyte. It is also known that for full-cells, transition metal oxide dissolution occurs from the cathode (positive

electrode).[128] This results in transition metals from the cathode being deposited in the SEI formed on the anode which is also thought to lead to capacity loss. A similar process of transition metal dissolution has been reported for NIB full-cells as well.[129]

Compared to the SEI formed in LIBs, the SEI in NIBs has not been studied to the same extent, and the SEI studies that have been performed for NIBs tend to focus on the SEI formed in half-cells, where Na metal is present. For example, Pan *et al.*[130] combined XPS and FTIR to study the SEI produced in Na half-cells with an electrolyte of 1 M $NaPF_6$ in ethylene carbonate (EC) and diethylene carbonate (DEC) (1:2 v/v%). The authors were able to confirm that the SEI was composed mainly of Na ethylene dicarbonate (NEDC) and NaF, with smaller amounts of Na alkyl carbonates, Na carboxylates ($NaCO_2R$), Na carbonate (Na_2CO_3) and various Na fluorophosphates (i.e., $Na_xPF_yO_z$). Furthermore, as the signals for the hard carbon electrode were not observed after 25 cycles, it was determined that the SEI was at least as thick as the XPS penetration depth (~10 nm). Similarly, Fondard *et al.*[131] utilised XPS to investigate the SEI formed on hard carbon anodes in half-cells after extended cycling (135 cycles) with electrolytes consisting of 1 M $NaPF_6$ or Na bis(trifluoromethanesulfonyl)imide (NaTFSI) in EC:DMC (1:1 v/v%), with and without additives such as fluoroethylene carbonate (FEC) and fluorinated dimethyl carbonate. For cells with the best capacity retention (1 M $NaPF_6$ in EC:DMC with 3% FEC), the was SEI mainly composed of NEDC and NaF, whereas cells with poorer capacity retention had an SEI mainly consisting of NaF and Na_2CO_3.

As Na salts are known to be more soluble than their Li equivalents,[61] it is thought that the Na SEI is more soluble than the equivalent SEI formed in LIBs. This was investigated by Mogensen *et al.*[74] who used synchrotron-based hard X-ray photoelectron spectroscopy (HAXPES) to determine that SEI formed on hard carbon in half-cells undergoes dissolution occurs at a faster rate in NIBs than LIBs, leading to a greater amount of self-discharge. Similarly, Ma *et al.*[132] also investigated the SEI formed in Na half-cells. It was found that the electrolyte solvent, salt and additives all influence SEI dissolution. For example, more SEI dissolution occurred for an electrolyte with propylene carbonate (PC) as the solvent than EC:DEC. The authors suggest that this could be due to inorganic SEI components such as NaF and Na_2CO_3 being more soluble in PC than EC:DEC. However, SEI dissolution (and therefore capacity loss) could be minimised by pre-saturating the electrolyte with inorganic SEI components.

Despite the work done in these studies, it is not known if these components are produced from, or due, to the presence of metallic Na. In this chapter, the SEI formed on hard carbon is compared for full- and half-cells after various amounts of cycling, using three different analysis techniques. The insoluble SEI will be studied by SSNMR, in conjunction with the more surface specific XPS and the soluble SEI and electrolyte degradation products will be analysed by using solution NMR.

5.3 Experimental

5.3.1 Sample Preparation

Mass balanced hard carbon anodes and transition metal oxide cathodes were provided by Faradion. These electrodes were prepared by mixing the active materials with PVDF and a conductive carbon additive before being cast onto Al foil. The transition metal oxide is a mixed-phase O3/P2 material with the general composition $Na_x[Ni/Mn/Mg/Ti]O_2$.[55]

Coin cells were prepared from these electrodes using 2032 coin cell components in a Ar glovebox (O_2 < 1 ppm, H_2O < 1 ppm). For full-cells, hard carbon anodes and transition metal cathodes were provided by Faradion. For the half-cells, the same hard carbon electrodes were used with Na metal (Sigma-Aldrich) as a counter electrode. For all cells, the electrolyte used was 1 M $NaPF_6$ (prepared in house, to ensure a higher purity, using a synthesis method previously outlined by Ould *et al.*[133]) in EC:DMC (1:1 v/v%. Solvionic, 99.9 % chemical purity) and borosilicate glass fibre (Whatman, GF/B) was used as the separator. All electrodes and $NaPF_6$ were dried at 120 °C *in vacuo* prior to use.

The coin cells were that were cycled, were done so galvanostatically (between 1.0 V and 4.2 V for the full-cells and between 2.00 V and 0.01 V for the half-cells) using a Biologic MPG2 battery cycler at a rate of *C*/10, based on the theoretical capacities of 130 mAh g^{-1} for the full-cells and 250 mAh g^{-1} for the half-cells. Both full- and half-cells were cycled 1, 8 or 25 times. Other electrodes were either not assembled into cells (pristine) or assembled into cells that were rested for 3 days, without cycling, before being disassembled in an Ar glovebox in a similar way to the cycled cells.

5.3.2 SSNMR

SSNMR experiments were performed on either pristine, uncycled or cycled hard carbon electrodes. The electrodes assembled into cells were transferred to an Ar glovebox (O_2 < 1 ppm, H_2O < 1 ppm) where they were opened and the hard carbon electrodes were removed. The electrodes films were then scraped off the current collectors and dried *in vacuo* for 15 minutes in the glovebox prechamber before being centre packed into rotors with KBr that had been dried at 120 °C *in vacuo* prior to use.

All SSNMR spectra were collected on a Bruker Advance III HD console, equipped with a 11.7 T Bruker widebore magnet. Experiments were conducted using a 2.5 mm Bruker double-channel MAS probe. Rotor synchronised Hahn echo experiments were used for ^{19}F, ^{23}Na and ^{31}P. The chemical shifts were referenced to LiF (s) ($\delta_{iso}(^{19}F)$ = –204.0 ppm), NaCl (s) ($\delta_{iso}(^{23}Na)$ = 7.2 ppm) or ammonium dihydrogen phosphate (s) ($\delta_{iso}(^{31}P)$ = 1.0 ppm). Further experimental details are given in Table A3.

5.3.3 XPS

After cycling, the coin cells were opened in an Ar glovebox (O_2 < 1 ppm, H_2O < 1 ppm). The hard carbon electrodes were removed and washed with three 1 mL aliquots of DMC to remove as much

residual surface electrolyte as possible and then dried *in vacuo*. The electrodes were affixed to a sample stub using Cu tape, as were the reference samples, and then transferred to the spectrometer using an air sensitive sample holder.

Experiments were conducted using an Escalab 250XI spectrometer from Thermo Fisher Scientific (West Sussex, UK). The instrument was operating in constant analyser energy mode. A monochromatic Al-K_α source (1486.74 eV) with a 900 μm spot size. For the electrodes charge compensation was not used, but for the reference powders charge compensation was provided by a flood gun. Survey spectra were acquired using pass energy of 100 eV, 3 scans were recorded using 0.10 eV steps and a dwell time of 50 ms. The detailed spectra had a pass energy of 20 eV, step size of 0.05 eV and a dwell time of 50 ms. Most detailed spectra were acquired with 10 scans, although for the transition metal cathode the Ni2*p* and Mn2*p* spectra had 20 scans, Mg2*s* spectrum had 25 scans and Ti2*p* spectrum had 30 scans, along with the P2*p*, Si2*p* spectra of the hard carbon anodes. The energetic position of the C1*s* emission line (binding energy of 284.6 eV) was chosen to calibrate the energy scale of the spectra. CASA XPS software was used to analyse each spectrum, using Lorentzian Asymmetric curve fitting and U2 Tougaard background.

5.3.4 Solution NMR

After cycling, the coin cells were opened in an Ar glovebox (O_2 < 1 ppm, H_2O < 1 ppm). The glass fibre separators were removed from the cells and soaked in 0.75 mL of deuterated dimethyl sulfoxide (DMSO-d_6) (Sigma-Aldrich, 99.96 atom % D, 99% chemical purity) or deuterated tetrahydrofuran (THF-d_8) (Fluorochem, 99.5 atom % D, 99.5 % chemical purity). The resulting solutions were then transferred to an airtight J Young NMR tube and NMR spectra were collected using a Bruker Advance III HD console, equipped with a 11.7 T Bruker magnet using a BBO probe**.** ^{1}H spectra were internally referenced to DMSO-d_6 (δ (^{1}H) = 2.50 ppm), ^{19}F and ^{31}P were internally referenced to $NaPF_6$ ((δ (^{19}F) = –72.7 ppm and δ (^{31}P) = –146.1 ppm)

5.4 Results

5.4.1 Electrochemistry

The voltage profile for a hard carbon half-cell over 25 cycles is given in Figure 5-1 (a). The voltage profile has two distinct regions, a slope and plateau, and these regions each correspond to about half of the capacity. There is a significant drop in capacity after the first discharge from approximately 300 mAh g^{-1} to 250 mAh g^{-1}, which is accompanied by the loss of a feature at around 0.5 V, which is highlighted by the differential capacity plot for the first two cycles in Figure 5-1 (b). This is assigned to initial SEI formation. Figure 5-1 (c) shows that on subsequent cycling, there is a continual capacity loss to approximately 130 mAh g^{-1} after 30 cycles. This significant capacity loss could be assigned to further SEI formation and/or electrolyte degradation, possibly due to the presence of Na metal or the hard carbon becoming less active on prolonged cycling.

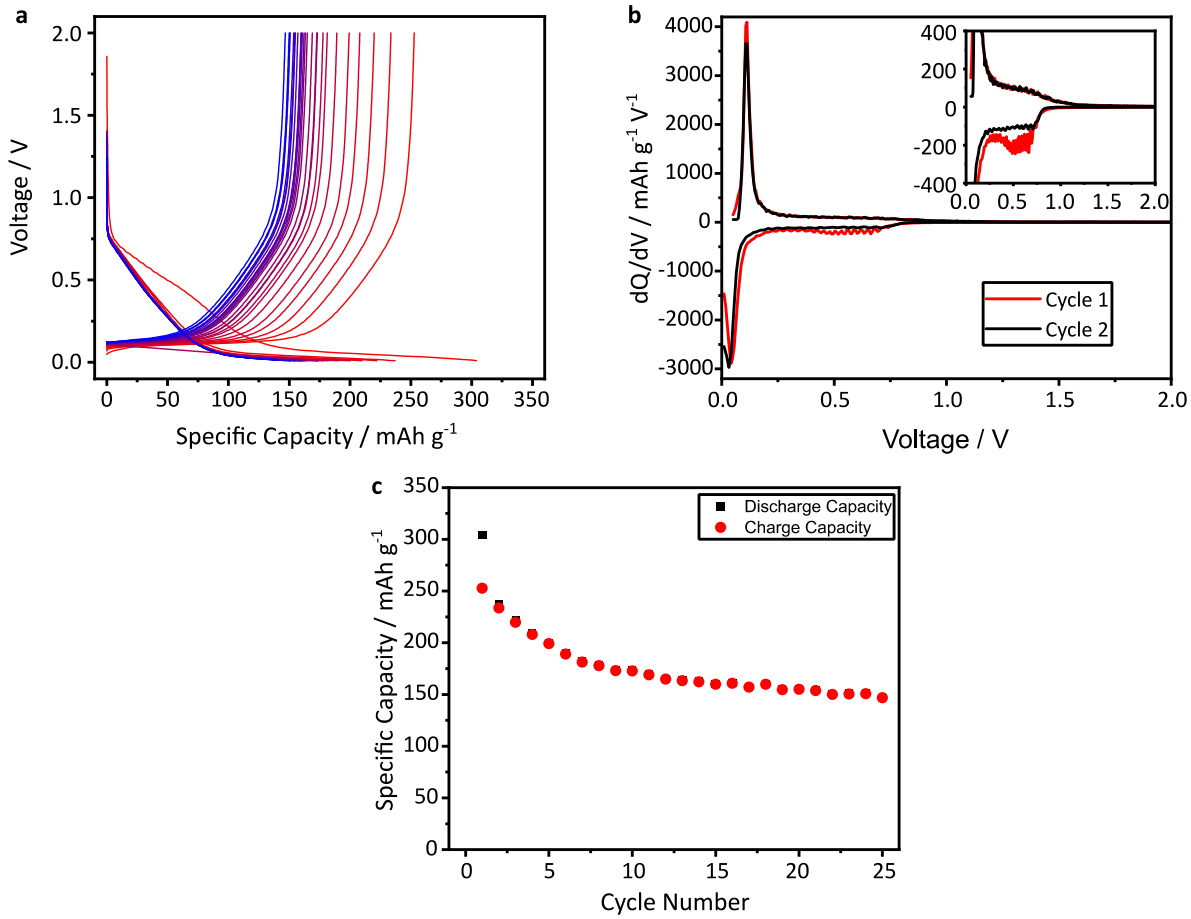

Figure 5-1: (a) Voltage profile, (b) differential (c) capacity plot and capacity verus cycle plot for a half-cell cycled 25 times, with a 1 M $NaPF_6$ in EC:DMC electrolyte at a rate corresponding to C/10. For (a) the 1st cycle is red and 25th cycle is blue, in (b) the red trace corresponds to the first cycle and the black trace corresponds to the third cyle and for (c) the black squares correspond to disharging and red circles correspond to charging.

For the full-cell (Figure 5-2 (a)), the voltage profile consists mainly of a sloping region from about 2.2 V to 4.0 V, followed by a shallower slope to 4.2 V, which is a combination of the voltage profiles of both hard carbon and transition metal cathode half-cells (the voltage profile for the first cycle of a transition metal cathode in a half cell is given in Figure 5-2 (b)). Figure 5-2 (d) shows that whilst there is a significant capacity loss for the full-cell after the first cycle, from approximately 170 mAh g^{-1} to 120 mAh g^{-1} possibly due to SEI formation, there is a smaller capacity fade on longer time cycling, to approximately 90 mAh g^{-1} after 30 cycles. This suggests that the absence of Na metal means results in less capacity loss, possibly as Na metal is not degrading the electrolyte.

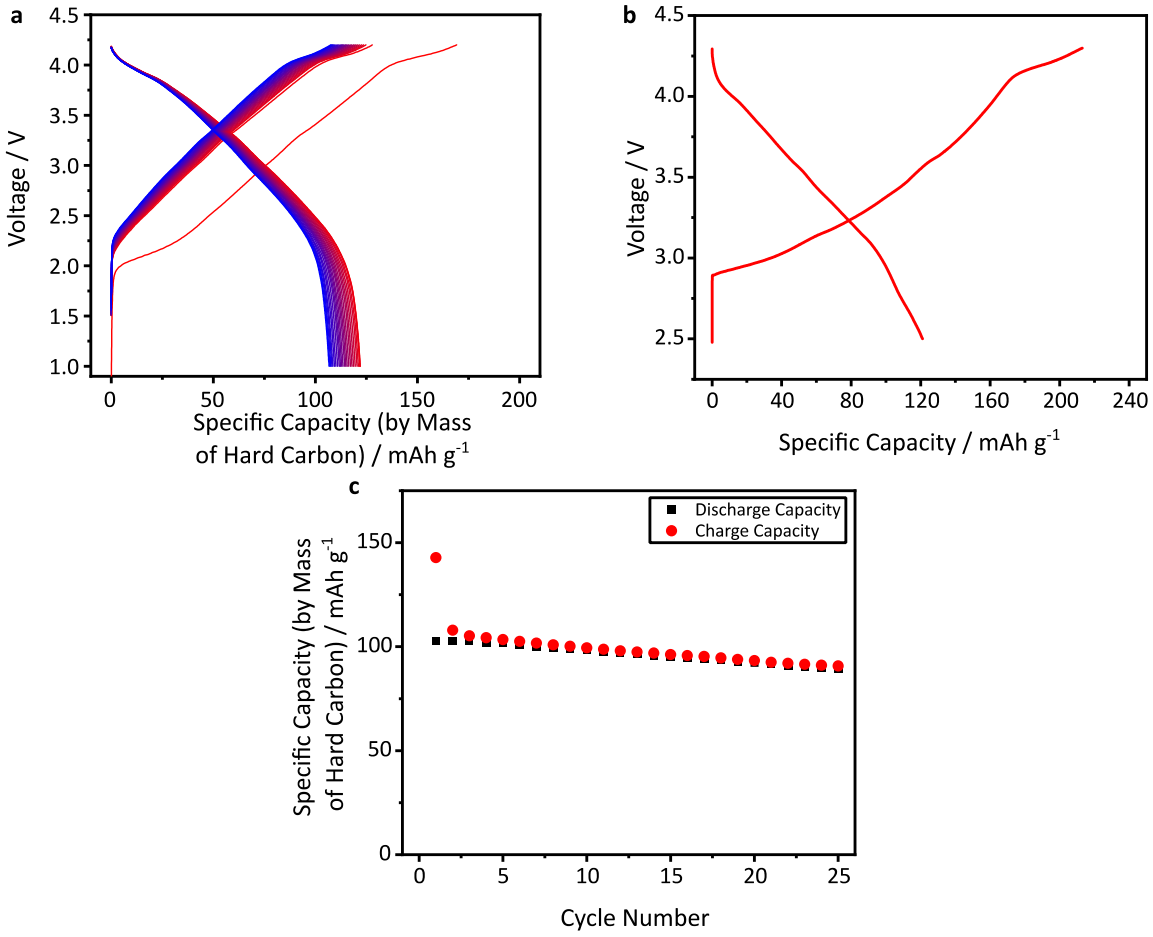

Figure 5-2: Voltage profiles for (a) a full-cell, cycled 25 times between 1.0 V and 4.2 V where the 1st cycle is red and 25th cycle is blue, as well (b) a transition metal cathode half-cell cycled between 2.5 V and 4.3 V. Both cells were cycled with a 1 M $NaPF_6$ in EC:DMC electrolyte at a rate corresponding to C/10. (c) A capacity verus cycle plot for the full-cell cycled 25 times, where black squares correspond to disharging and red circles correspond to charging.

5.4.2 Solid-State NMR

SSNMR was used to investigate the SEI formed on hard carbon electrodes for full- and half-cells. Despite not being a surface sensitive technique, SSNMR was chosen as it is very sensitive to different chemical environments and should be able to identify major components of the SEI. Figure 5-3 shows ^{19}F SSNMR spectra that were collected for all hard carbon samples, in a desodiated state, as well as pure PVDF and NaF. The spectrum for a pristine hard carbon electrode (green trace) has two overlapping peaks at –92 ppm and a corresponding spinning side band manifold, and as these peaks align with that of pure PVDF (blue trace), these signals correspond to PVDF, the binder used in the electrode preparation. For the uncycled electrode from a full-cell (purple trace), there is an additional doublet at –73 ppm ($^1J_{19F\text{-}31P}$ = 710 Hz), which is assigned to residual $NaPF_6$ as these electrodes were not washed. For all other samples, including the uncycled full-cell, there is an additional peak at –225 ppm which aligns with the signal observed in the spectrum of pure NaF. This signal grows in intensity with increased cycling and is more prominent for half-cells. This indicates that NaF is a major fluorine-

containing SEI component and NaF forms in half-cells, even without cycling, likely due to the presence of Na metal.

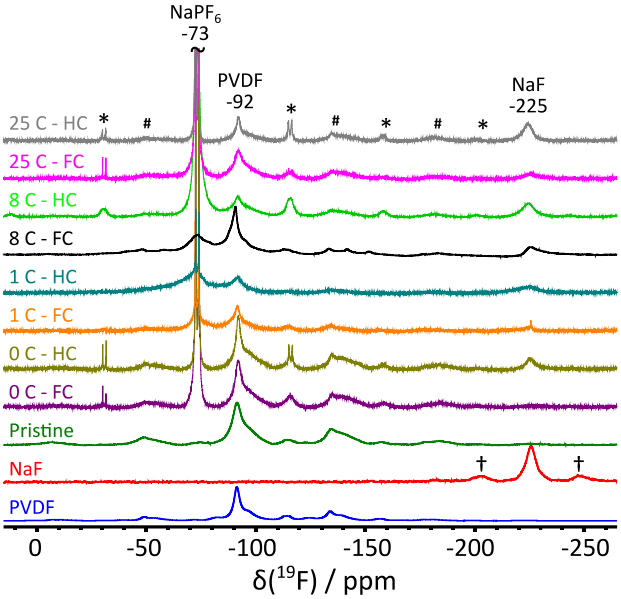

Figure 5-3: ^{19}F MAS SSNMR spectra for PVDF, (blue trace), NaF (red trace) and for all hard carbon electrodes at a MAS speed of 20 kHz. For the hard carbon samples, the number, X, in "XC" corresponds to the number of times the cells was cycled, "FC" corresponds to a full-cell and "HC" corresponds to a half-cell. "" denotes spinning side bands for the $NaPF_6$ signal at –73 ppm, "#" denotes spinning side bands for the PVDF signal at –92 ppm and "†" denotes spinning side bands for NaF at –225 ppm.*

^{23}Na SSNMR spectra were also collected for all hard carbon samples and some reference compounds (Figure 5-4 (a)). No signals are seen for the spectrum of the pristine electrode (blue trace), which is as expected as no Na-containing compounds have been added to this sample. For all subsequent cycles, there are three peaks at 5 ppm, –7 ppm and –10 ppm. The first of these aligns with the signal observed in the spectrum of pure NaF, (Figure 5-4 (b), dark yellow trace). However, the intensity does not appear to grow with increased cycling, so this peak cannot only arise from NaF. To help assign this peak, a sample of solvated $NaPF_6$ was prepared by dissolving a small amount $NaPF_6$ (14.5 mg) in EC:DMC (50 µL), and then drying it *in vacuo*. The resulting ^{23}Na SSNMR spectrum (Figure 5-4 (b), blue trace) consists of three signals at 5 ppm, –11 ppm and – 20 ppm, the latter of which is the same chemical position as due to crystalline $NaPF_6$. The peaks at 5 ppm and –20 ppm are seen in the ^{1}H-^{23}Na CP spectrum (Figure 5-4, red trace). Whilst the later of these is partially solvated $NaPF_6$, the 5 ppm signal is assigned to Na^+ ions solvated by EC:DMC. Therefore for cycled hard carbon, the signal at 5 ppm is assigned to a combination of NaF and Na^+ ions solvated with EC:DMC.

The two remaining signals at –7 ppm and –10 ppm, which do not show a trend on increased cycling or between full- and half-cells, are more challenging to assign as not many Na compounds previously reported as components of the SEI have negative chemical shifts. ^{23}Na SSNMR spectra were collected for some other components that have previously been reported as possible SEI components,[134]

Na_2CO_3 (Figure 5-4 (b), green trace) has a sharp peak at 5 ppm and a broad pattern centred around –10 ppm and $NaHCO_3$ (Figure 5-4, purple trace) has a sharp peak at –5 ppm. Whilst neither of these components aligns with the peaks align with the hard carbon spectra, one would not necessarily expect crystalline compounds in the SEI and it is possible that compounds such Na_2CO_3 or $NaHCO_3$ may be present in a slightly disordered form, or in nanoparticles that will have their chemical shift influenced by the hard carbon electrode, both of which mean making direct comparison to typical SEI components difficult. Likewise, it is also possible that these signals also correlate to Na alkyl carbonates.

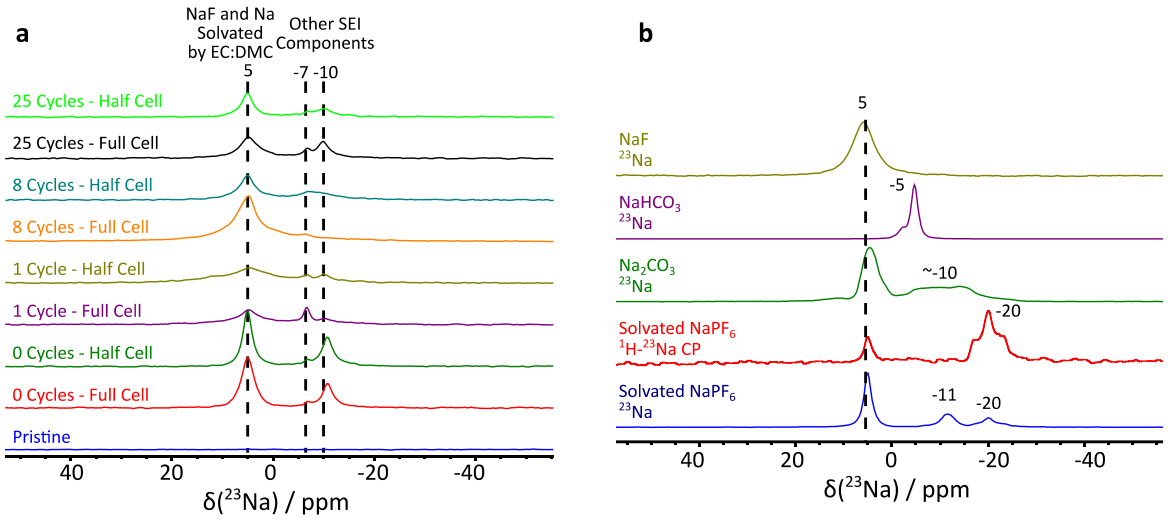

Figure 5-4: (a) ^{23}Na MAS SSNMR samples for all hard carbon samples, (b) Further ^{23}Na MAS spectra for $NaPF_6$ solvated with EC:DMC (blue trace), Na_2CO_3 (green trave, $NaHCO_3$ (purple trace) and NaF (dark yellow trace). Also a ^{1}H-^{23}Na CP MAS SSNMR spectrum of $NaPF_6$ solvated with EC:DMC (red trace). All spectra were collected at a MAS speed of 20 kHz except NaF and ^{1}H-^{23}Na CP which were collected at 10 kHz.

^{31}P SSNMR spectra were also collected for all the hard carbon samples, except pristine hard carbon (Figure 5-5). The most prominent feature for these spectra is the septet at –145 ppm ($^{1}J_{31P\text{-}19F}$ = 710 kHz) which is present for all samples and corresponds to $NaPF_6$, or solvated PF_6^- ions. There are some additional peaks at 20 ppm and 3 ppm for some samples during intermediate amount of cycling, could correspond to Na fluorophosphate species like $NaPO_2F_2$ and Na_2PO_3F. Overall, it can be stated that whilst SSNMR is able to detect SEI components, the lack of surface specificity means it cannot provide additional structural information about the SEI. Therefore, SSNMR must be used together with other techniques to gain a better understanding of the SEI.

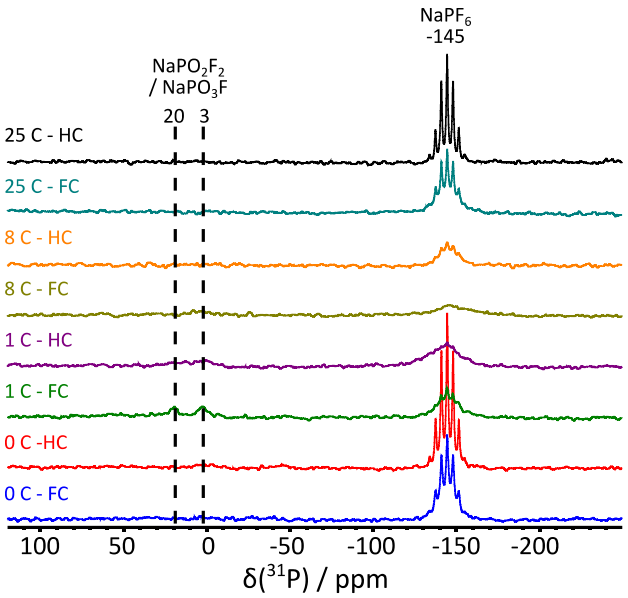

Figure 5-5: ^{31}P MAS SSNMR spectra for all hard carbon samples, except pristine electrode, at a MAS speed of 20 kHz. Samples. X, in "XC" corresponds to the number of times the cells was cycled, "FC" corresponds to a full-cell and "HC" corresponds to a half-cell.

5.4.3 XPS

5.4.3.1 Hard Carbon Anodes

To get a better understanding of surface composition of the hard carbon electrodes, XPS spectra were collected for all hard carbon samples. The survey spectra for each electrode and the elemental composition of the surface of each electrode (as determined from the survey spectra) are given in Figure 5-6 (a) and (b), respectively. The surface of the pristine (i.e. assembled but not cycled) hard carbon electrode is mainly composed of C (red trace), with smaller amounts of F (green trace) and O (grey trace). The F signals are a result of the PVDF binder, whereas the O signals come from terminal groups on the carbon sheets and defect sites There is a minimal change in the surface composition for the electrode for an uncycled full-cell, indicating minimal SEI formation has occurred. However, there is a significant change for all subsequent samples, including the electrode from an uncycled half-cell. For these samples, the relative proportion of C decreases, whilst the proportion of F, O, Na (purple trace) and P (cyan trace) increases. This is good evidence for SEI formation; the proportion of O is always higher for half-cells than full-cells after an equivalent amount of cycling, which suggests more SEI maybe present for half-cells.

The inset in Figure 5-6 (b) shows the presence of trace elements; Si (brown trace), N (blue trace) and Ti (yellow trace). The proportion of Si is random which suggests that the Si signals correspond to residual amounts of glass fibre from the coin cell separators that have not been washed off the electrodes, (although Si fluorides can form if HF attacks the separator). N decreases on increased cycling suggesting it is a trace component of the hard carbon electrodes that slowly becomes screened

by SEI. Ti is only present for full-cells and appears to increase in intensity on increased cycling. As Ti is a component of the transition metal oxide cathodes used for full-cells, it appears that some transition metal dissolution is occurring in this system. However, there is no sign of other components of the cathode: Ni, Mg or Mn.

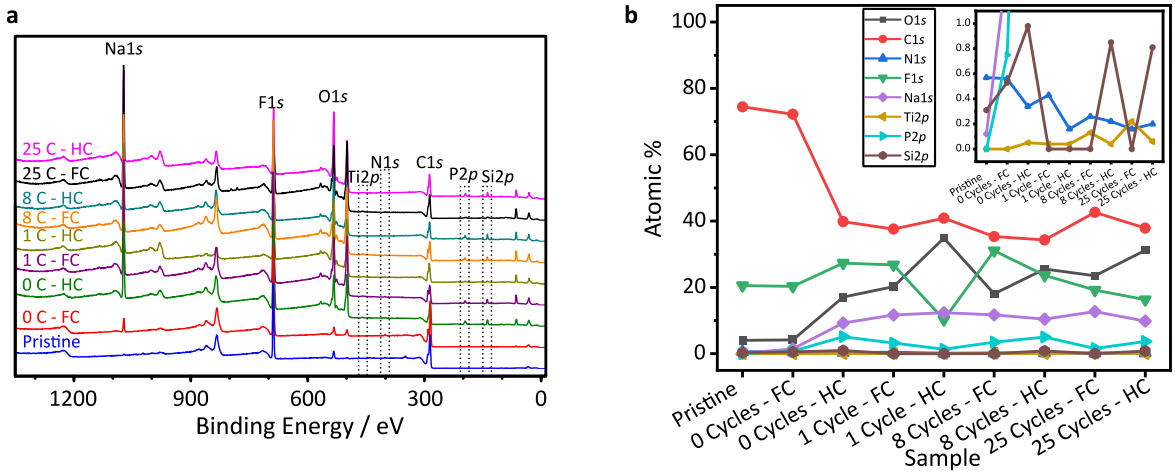

Figure 5-6: (a) Survey spectra and (b) elemental compositions for all hard carbon samples, as determined from the survey spectra, with the trace elements shown in the inset

Figure 5-7 shows the detailed XPS spectra for all hard carbon samples for the F1*s*, O1*s*, Na1*s*, P2*p* and C1*s* regions, as well as spectra of the reference compounds NaF (cyan trace), $NaPF_6$ (blue trace) and $LiPO_2F_2$ (brown trace). $LiPO_2F_2$ was used as $NaPO_2F_2$ is not commercially available, and the chemical environments of P, O and F in the anion are expected to be similar. For each element, peak fitting was carried out, and a detailed description of the results for each element are given below.

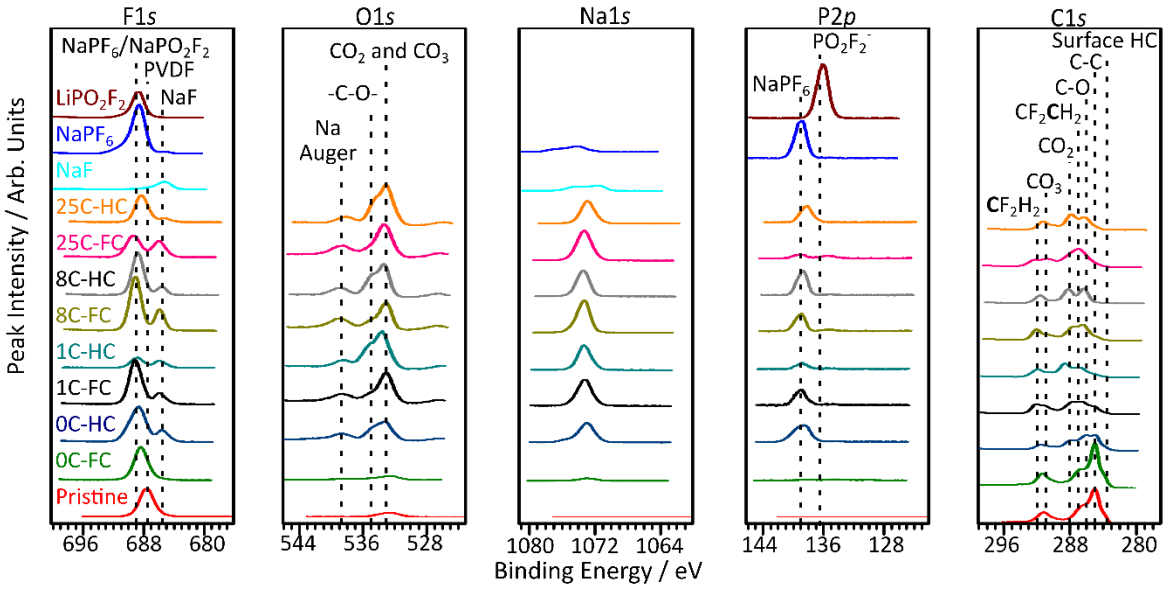

Figure 5-7: F1s, O1s, Na1s, P2p and C1s XPS spectra for all hard carbon samples as well as NaF, $NaPF_6$ and $LiPO_2F_2$. Samples. The number before C corresponds to the number of times the cells was cycled, "FC" corresponds to a full-cell and "HC" corresponds to a half-cell

For the F1*s* region, there are three different environments present, with peaks at 686 eV, 688 eV and 689 eV. An example of the fitting of a F1s spectrum consisting of three peaks is show in Figure 5-8 (a), which shows the F1*s* spectrum for the full-cell cycled once. The raw intensities of the 686 eV, 688 eV and 689 eV environments are given in Figure 5-8 (b), (c) and (d), respectively. For the pristine hard carbon electrode, only the only peak present is at 688 eV which is assigned to the CF_2 groups in the PVDF binder. On subsequent cycling, the intensity of this peak decreases as SEI is deposited on the electrode and screens the PVDF. All subsequent hard carbon samples have a signal at 689 eV which is mainly from $NaPF_6$, and the intensity of this signal is random, as expected due to inconsistencies in washing the samples. However, the binding energy of this peak also aligns with $LiPO_2F_2$, which suggests that some Na fluorophosphate species, such as $NaPO_2F_2$, could also be present, but it is not possible to pick these species out. The peak at 686 eV aligns with NaF, which is a common SEI component and was observed with SSNMR. Unlike the results from SSNMR, the intensity of this signal is more dominant for full-cells compared to half-cells. One explanation for this is that half-cells may have other components of the SEI that are screening NaF (*vide infra*).

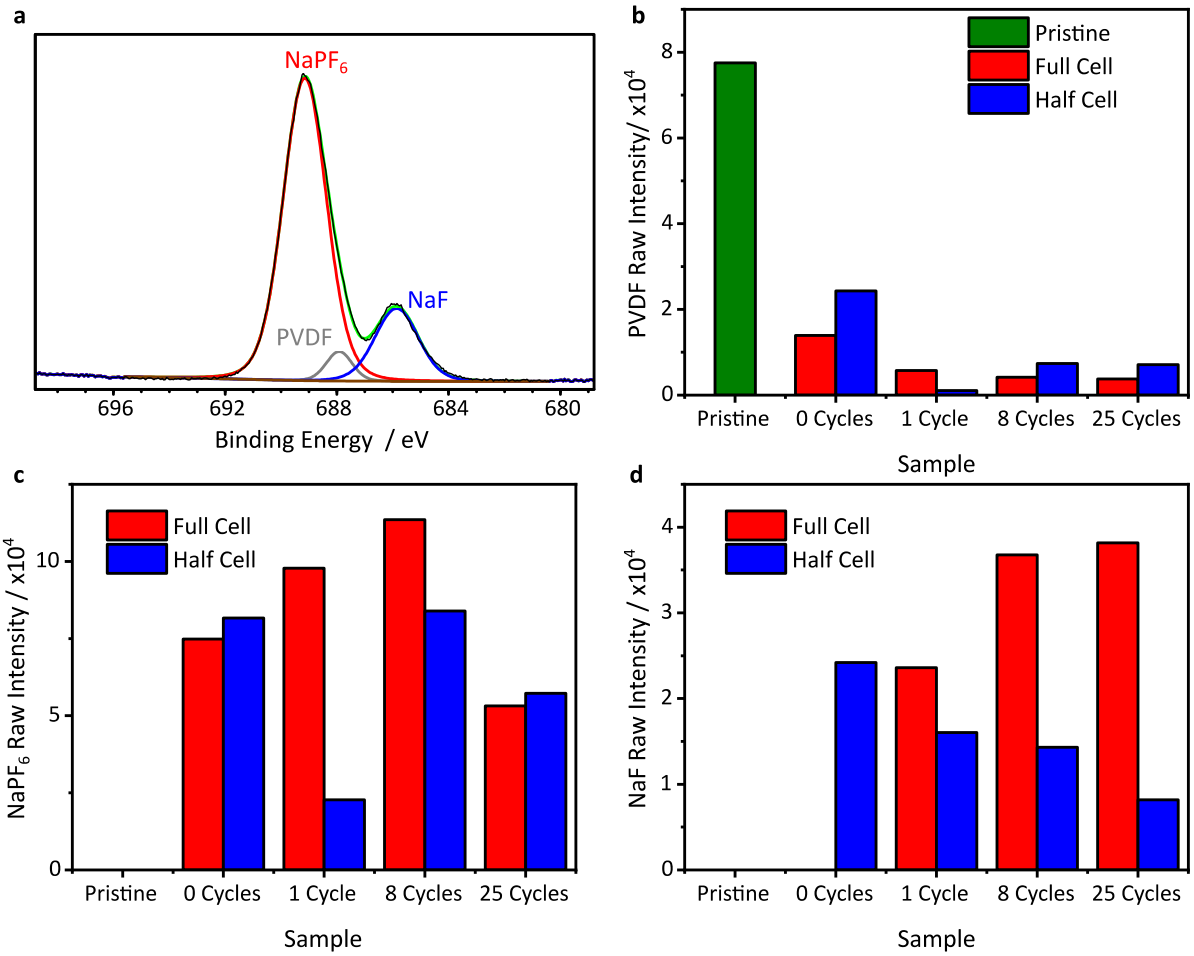

Figure 5-8: (a) Raw XPS F1s spectrum for the full-cell cycled once (black trace) and the fitted spectrum (light green trace). The peak at 686 eV is PVDF (grey trace), 688 eV is $NaPF_6$ (red trace) and 689 eV is NaF (blue trace). The intensities of the (b) PVDF, (c) $NaPF_6$ and (d) NaF environments after peak fitting are given for all samples.

For the O1*s* region, there are two oxygen signals at 533 eV and 535 eV, as demonstrated in Figure 5-9 (a), which shows the fitted O1*s* spectrum for the full-cell after one cycle, where the remaining peak 538 eV, corresponds to a Na KLL Auger peak. The raw intensities of the peaks at 533 eV and 535 eV for all samples are given in Figure 5-9 (b) and (c), respectively. For the pristine hard carbon electrode and hard carbon from an uncycled full-cell, the intensities are quite similar, indicating minimal SEI formation. There is a noticeable increase in both peaks for all other samples, which suggests that the amount of O-containing SEI species grows with cycling. The peak at 533 eV corresponds to CO_2 and CO_3 groups, which indicates that species such as Na alkyl carbonates and Na_2CO_3 are likely present. The peak at 535 eV corresponds to C-O groups that would be present for polymeric species in the SEI, such as polyethylene glycol (PEG). Additionally, the intensity of the C-O peak is always higher for half-cells than full-cells, suggesting that half-cells have a greater amount of polymeric SEI present. This agrees with the F1*s* spectra, which appeared to show NaF being screened by other SEI components in half-cells.

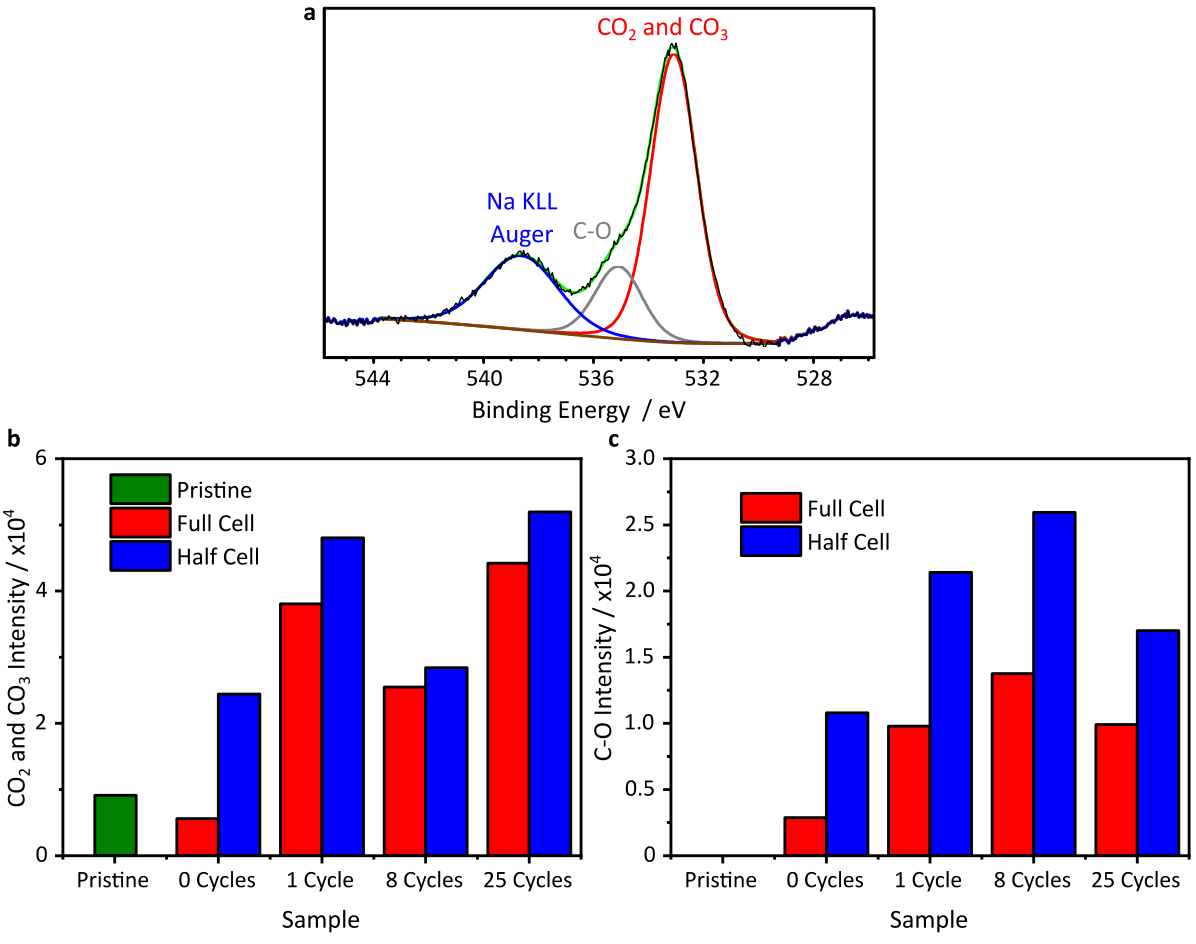

Figure 5-9: (a) Raw XPS O1s spectrum for the full-cell cycled once (black trace) and the fitted spectrum (light green trace). The peak 533 eV corresponds to CO_2 and CO_3 groups (grey trace), the peak at 535 eV is C-O groups (red trace) and the peak at 538 eV is the Na KLL Auger. The intensities of the (b) CO_2 and CO_3 and (c) C-O environments after peak fitting are given for all samples.

For the Na1*s* region, all signals appear to overlap to give one peak at 1074 eV, this is demonstrated in Figure 5-10 (a) which shows the Na1*s* spectrum fitted with one peak. The individual species cannot be identified; however, these raw intensities of these spectra (Figure 5-10 (b)) are still useful. In a similar manner to the SSNMR results, the pristine hard carbon has virtually no Na species present, as expected as no Na salts have been added at this point. The uncycled full-cell has a small amount of Na, which corresponds to residual $NaPF_6$ that is not removed on washing. There is then a significant increase for other samples, indicating SEI has formed for these sample. Furthermore, it appears that the cycled full-cells have more intense Na peaks than the cycled half-cells, and this could be explained by the increased amount of organic SEI formed in half-cells screening the inorganic salts.

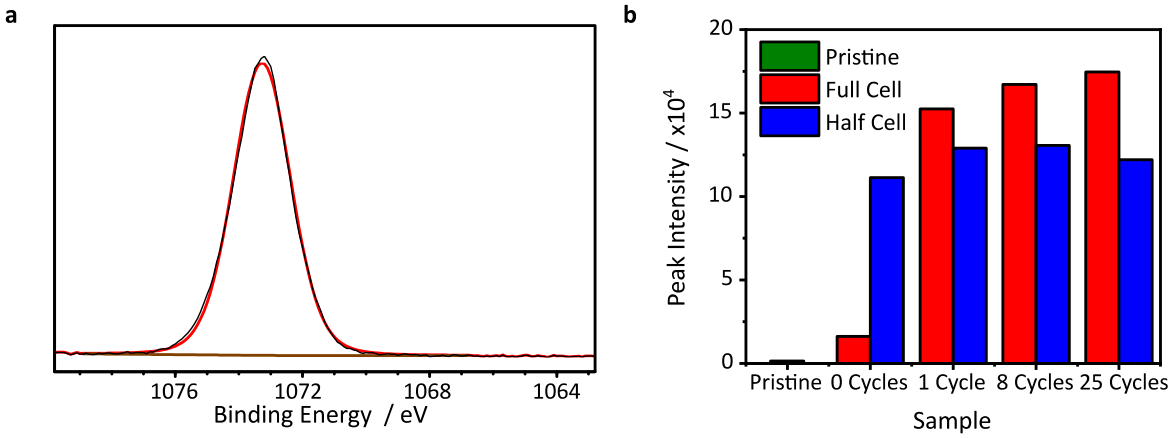

Figure 5-10: (a) Raw XPS Na1s spectrum for the full-cell cycled once (black trace) and the fitted peak (red trace). (b) The intensities of this environment after peak fitting for all samples.

For the P2*p* region, all spectra were fitted with two signals at 135 eV and 139 eV, as demonstrated by Figure 5-11 (a) which shows that the P2*p* region from the full-cell cycled one time after fitting. The intensities of these signals at 135 eV and 139 eV are given in Figure 5-11 (b) and (c), respectively, for all samples. The peak at 139 eV is assigned to $NaPF_6$ and the random variation in intensities is a result of inconsistent washing of the electrodes with DMC. The signal at 135 eV aligns closely with $LiPO_2F_2$; therefore, these signals are assigned to Na fluorophosphates, such as $NaPO_2F_2$. More of these species are observed in the spectra for full-cells suggesting that either more of these species, or that in half-cells they are screened by more organic SEI.

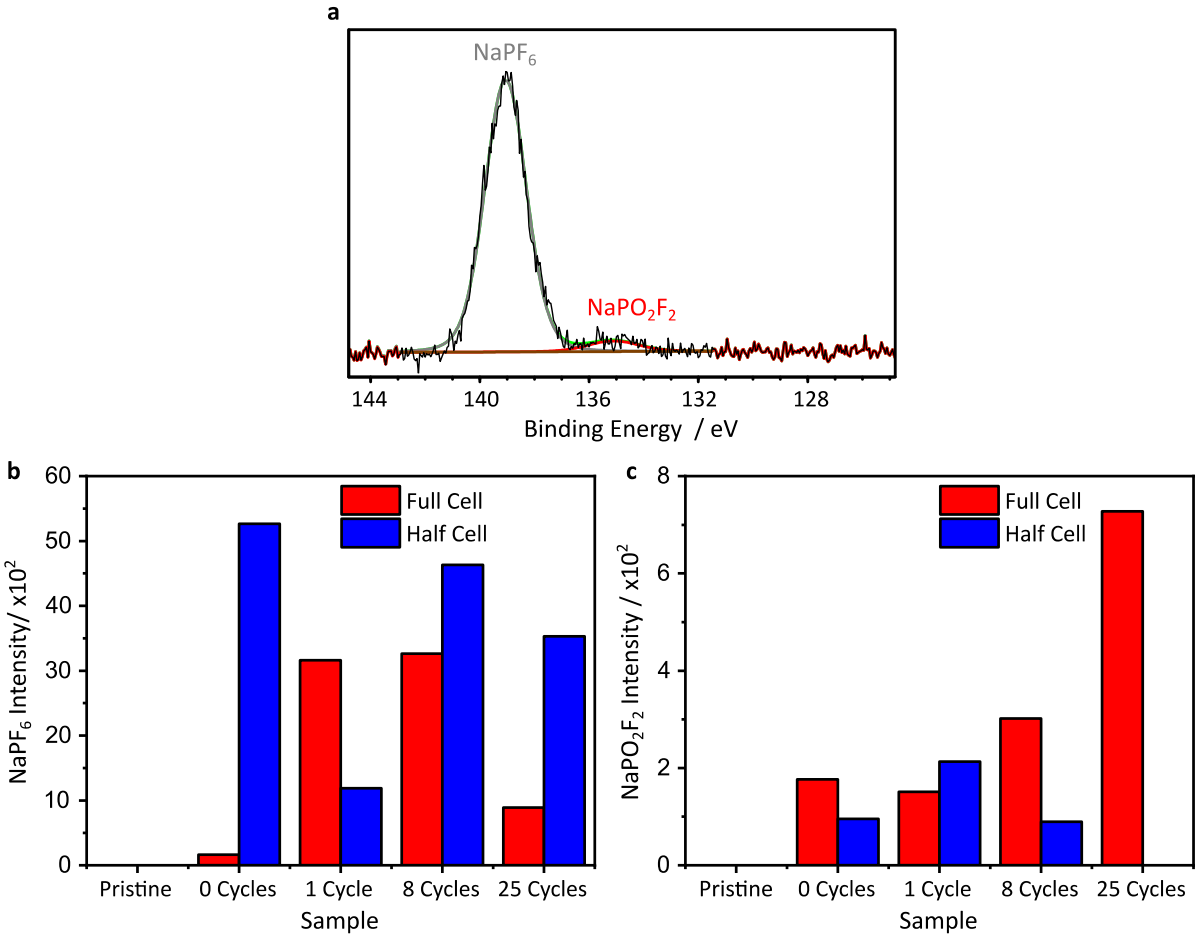

Figure 5-11: (a) Raw XPS P2p spectrum for the full-cell cycled once (black trace) and the fitted spectrum (light green trace). The peak 139 eV is $NaPF_6$ (grey trace) and the peak at 535 eV is $NaPO_2F_2$ (red trace). (b) The intensities of (b) $NaPF_6$ and (c) $NaPO_2F_2$ environments after peak fitting are given for all samples.

The C1*s* spectra are more challenging to fit as there are several overlapping peaks. Based on previously published studies,[130,131] there could be at least seven different environments present, including surface hard carbon groups, C-C/C-H, C-O, CH_2 (from PVDF), CO_2, CO_3 and CF_2 (from PVDF, with peaks at 284 eV, 285 eV, 286 eV, 287 eV, 288 eV, 290 eV and 292 eV. All C1*s* regions were fitted with these signals (as demonstrated by Figure 5-12 (a) which shows the C1*s* region of the full-cell cycled one time). The intensities of these peaks for all samples are given in Figure 5-12 (b) – (h), respectively. Whilst peak fitting with this many environments means care has to be taken, some trends can be observed. The spectra of pristine hard carbon electrode and the uncycled hard carbon electrode from a full-cell are similar, with signals mainly coming from hard carbon (surface HC groups and C-C/C-H) and the PVDF binder (CH_2 and CF_2). As the cycling increases, the relative intensities of hard carbon and PVDF signals decrease whilst those of signals from all O containing groups increases, suggesting that more SEI is formed for the cycled electrodes. Moreover, the proportion of C-O groups is generally higher for half-cells after cycling, this is consistent with more polymeric SEI being formed in half-cells compared to full-cells.

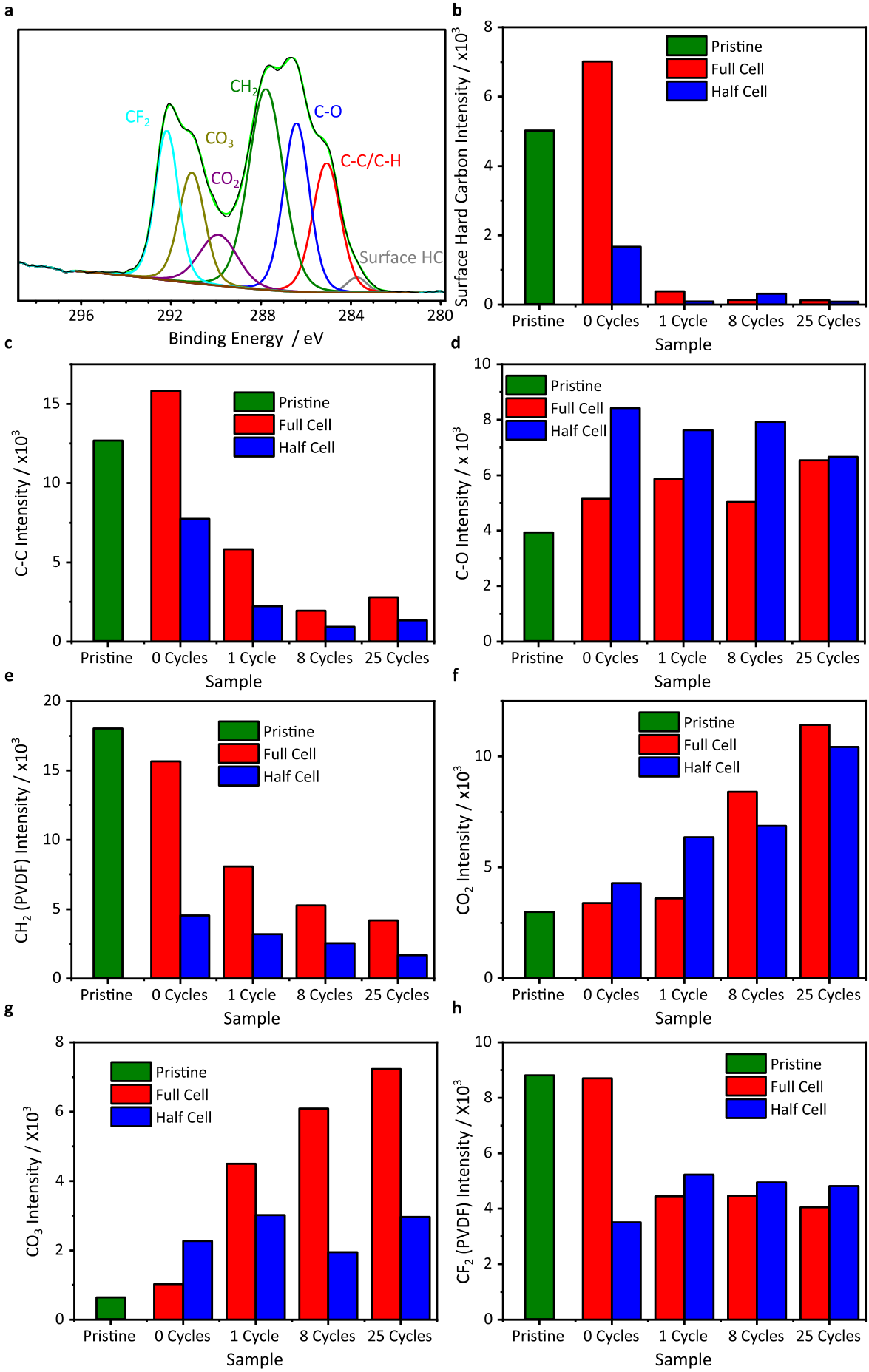
a
CF2
CO3
CH2
CO2
C-O
C-C/C-H
Surface HC
296
292
288
284
280
Binding Energy / eV
b
Surface Hard Carbon Intensity / x10^3
Pristine
Full Cell
Half Cell
Pristine
0 Cycles
1 Cycle
8 Cycles
25 Cycles
Sample
c
C-C Intensity / x10^3
d
C-O Intensity / x 10^3
e
CH2 (PVDF) Intensity / x10^3
f
CO2 Intensity / x10^3
g
CO3 Intensity / X10^3
h
CF2 (PVDF) Intensity / X10^3

Figure 5-12: (a) Raw XPS C1s spectrum for the full-cell cycled once (black trace) and the fitted spectrum (light green trace) (a). The peak at 284 eV is surface hard carbon groups (grey trace), the peak at 285 eV is C-C/C-H (red trace), the peak at 286 eV is C-O (blue trace), the peak at 287 eV is CH_2 groups from PVDF (dark green trace), the peak at 288 eV is CO_2, (purple trace), the peak at 290 eV is CO_3 and (dark yellow trace) and the peak at 292 eV are CF_1 groups from PVDF (cyan trace). The intensities of the (b) surface hard carbon, (c) C-C/C-H, (d) C-O (e) CH_2 (PVDF), (f) CO_2, (g) CO_3 and (h) CF_2 (PVDF) environments after peak fitting are given for all samples.

Detailed spectra of the Ti2*p* region were not collected, this combined with the low signal-to-noise for this signal means detailed information about the chemical state of Ti cannot be obtained. This is demonstrated in Figure 5-13, which shows a Ti2*p* signal for the full- and half-cells cycled 25 times from the survey spectra. There are appears to be a more intense signal for the full-cell, possibly indicating some Ti dissolution from the cathode has occurred. But the peaks splitting expected for Ti2*p* cannot be observed.

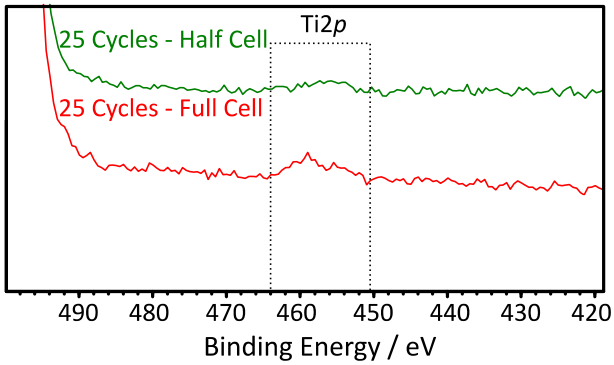

Figure 5-13: The Ti2p regions from the survey spectra for a half-cell (green trace) and full-cell (red trace) cycled 25 times.

5.4.3.2 Transition Metal Oxide Cathode

As the atomic compositions of the anodes from cycled full-cells appear to show increasing amounts of Ti on increased cycling, XPS spectra were also collected for a pristine transition metal cathode. The survey spectrum of the cathode is given in Figure 5-14 and the resulting elemental composition (as determined from the survey spectrum) is given in Table 5-1. These data show that the surface is dominated by O, C, F and Na, with only trace amounts of the transition metals Ti, Mn and Ni as well as trace amounts of N and P; notably, there are no signals from Mg present. This suggests that the cathode probably has a surface layer, such a layer of carbonate, that limits the observation of transition metals in the bulk of the material.

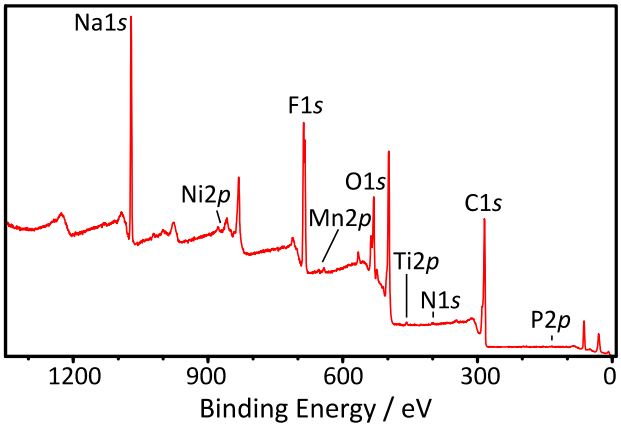

Figure 5-14: Survey XPS spectrum of the transition metal cathode.

Table 5-1: Elemental composition for the pristine transition metal cathode, as determined by XPS

O1*s*	**C1*s***	**N1*s***	**F1*s***	**Na1*s***	**Ti2*p***	**P2*p***	**Mn2*p***	**Ni2*p***
13.56	60.75	0.08	17.74	6.91	0.11	0.16	0.12	0.57

To get a better understanding of the metals in the cathode, the detailed spectra of the Mg1*s*, Mn2*p*, Ni2*p* and Ti2*p* regions were compared. As the elemental composition shows, there is no signal in the Mg1*s* region (Figure 5-15 (a)). The doublets for Mn and Ni are observed, with the Mn2*p*3 and 2*p*1 peaks (Figure 5-15 (b)) appearing at 642 eV and 654 eV, respectively, which is as expected for Mn oxides. However, the low signal-to-noise ratios in the spectrum for this sample, and the fact that different Mn oxides have been reported to have very similar binding energies for different Mn oxidation states,[135] means the oxidation state of Mn cannot be confirmed. For the Ni2*p* region (Figure 5-15 (c)), the relatively large peaks at 859 eV and 878 eV are satellite peaks of the F KLL Auger and the actual Ni2*p*3 and Ni2*p*1 peaks are at 855 eV and 873 eV, respectively, which is the expected binding energies for Ni(II) species such as NiO.[136] For Ti2*p* region (Figure 5-15 (d)), there is only one peak at 459 eV, which is where the Ti2*p*3 signal for a Ti(IV) species such as TiO_2 is expected.[137] The Ti2*p*1 signal at approximately 464 eV is not observed, which suggests that this signal may not be due to Ti. However, the only other species in this region are Ru3*d* and In3*d*, both of which are very unlikely. The Ti2*s* region (from the survey spectrum, Figure 5-15 (e)) is not useful as it overlaps with satellite peaks of O1*s*. Therefore, it is likely that there are two Ti2*p* peaks, but only the more intense one is visible due to the low signal-to-noise ratios. Due to the combination of signal-to-noise ratios and peak overlap, it is therefore hard to observe the transition metal signals for the cathodes. These effects mean it will also be hard to observe these transition metal signals for hard carbon anodes

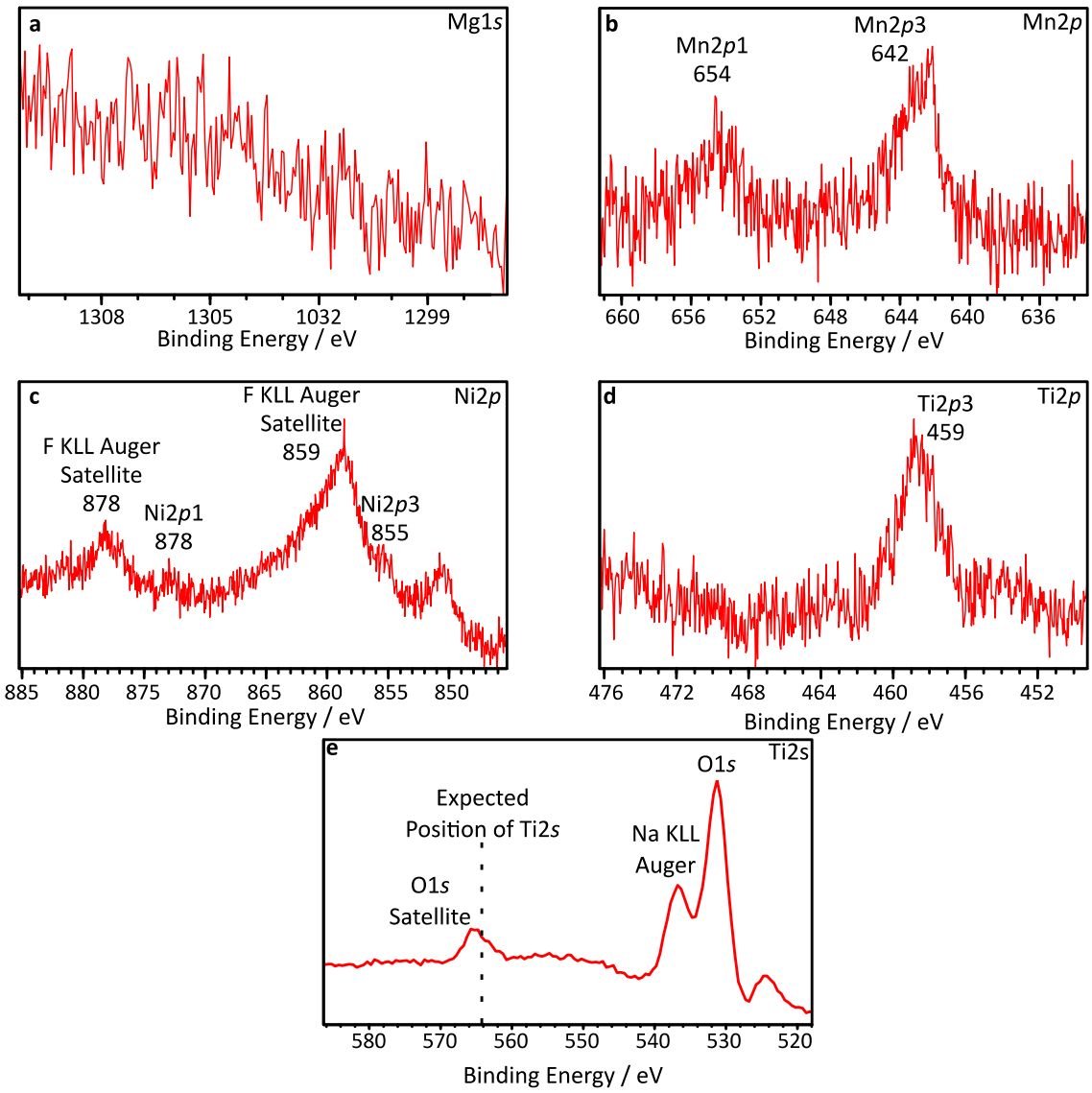

Figure 5-15: (a) Mg1s, (b) Mn2p, (c) Ni2p, (d) Ti2p and (e) Ti2s XPS spectra collected for a pristine transition metal cathode, the latter of which is from the survey spectrum.

5.4.4 Solution NMR

To study the soluble SEI components and or other soluble degradation products of the electrolyte, solution NMR was used as it is very sensitive to different chemical environments. Figure 5-16 shows ^{1}H solution NMR spectra of electrolytes for all cells. All spectra have signals for non-deuterated DMSO (2.51 ppm), DMC (3.70 ppm) and EC (4.48 ppm), as well as signals for H_2O (3.32 ppm) and HDO (3.30 ppm). The additional signal at 4.30 ppm is assigned to Na ethylene dicarbonate (NEDC), the Na equivalent of LEDC, which is commonly observed in the SEI of LIBs and is formed from by the reduction of EC. [138] For the uncycled samples (blue and red traces) and those cycled one time (green and purple traces), there are additional peaks with chemical shifts of 4.19 ppm, 4.08 ppm and 3.16 ppm, as well as several overlapping signals between 3.30 ppm and 3.60 ppm, which is where signals corresponding to polymeric species, such as PEG are expected.

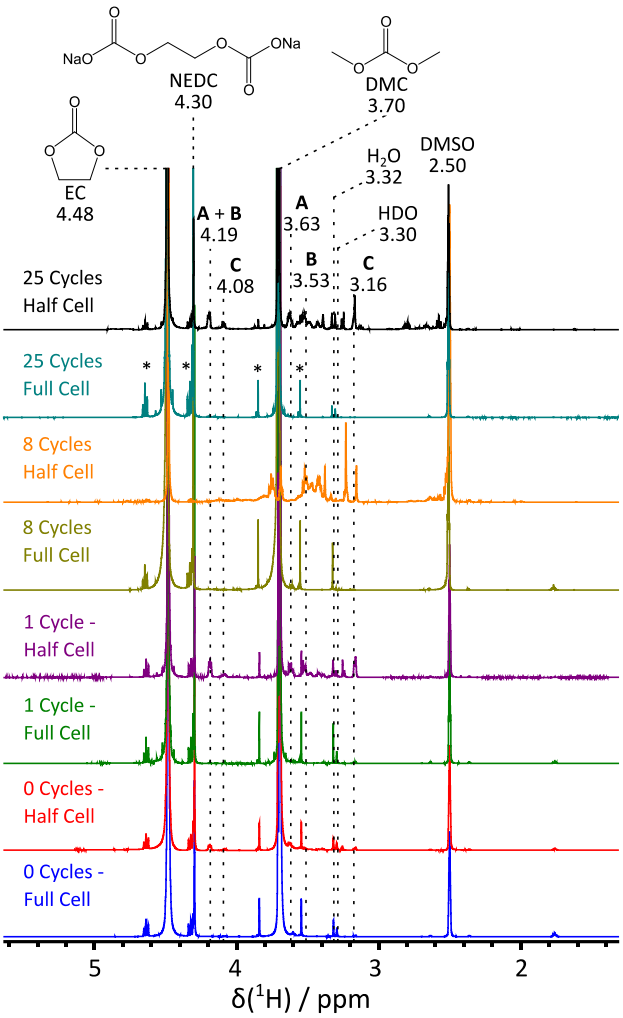

Figure 5-16: Solution NMR spectra collected for all hard carbon samples with a DMSO-d_{14} NMR solvent, satelite peaks are marked with asterisks.

To help assign these peaks, a two-dimensional ^{1}H correlation spectroscopy (COSY) spectrum was collected for the electrolyte of the half-cell after 1 cycle (Figure 5-17 (a)). From this spectrum, the 4.19 ppm peak is seen to correspond to two overlapping species with correlations to the peaks at 3.63 ppm (**A**) and 3.53 ppm (**B**), likewise the 4.08 ppm peak correlates with that at 3.16 ppm (**C**). Possible assignments could be species similar to Na ethylene monocarbonate (NEMC) (the structure of which is given in Figure 5-17 (b)) for **A** and **B** and methanol for **C**.

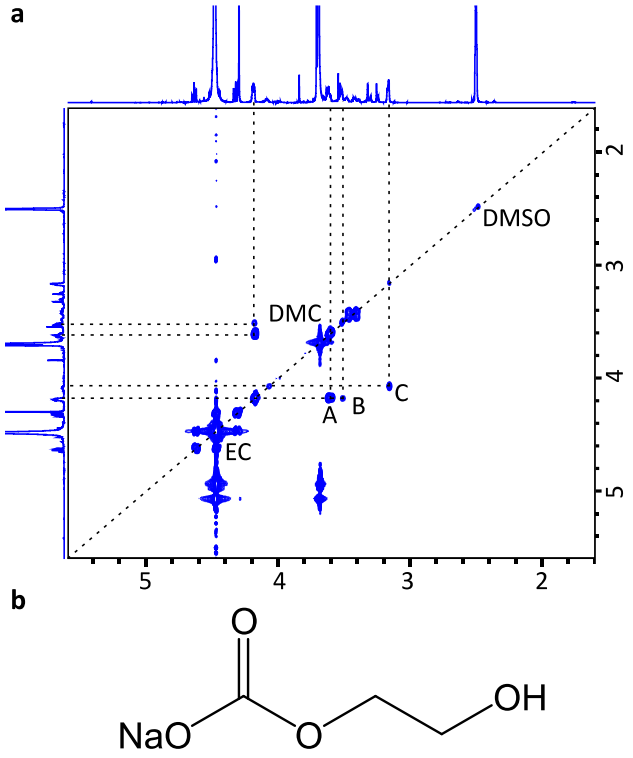

Figure 5-17: (a) ^{1}H COSY NMR spectrum for the electrolyte from a half-cell cycled one time and (b) the structure of Na ethylene monocarbonate (NEMC).

For the samples from half-cells that had longer-term cycling (8 and 25 cycles), there are significantly more degradation products, especially between 3.30 ppm and 3.60 ppm where polymeric or oligomeric species, such as PEG, are expected. However, it is known that Na metal reacts with DMSO[139] and when DMSO-d_6 was added to the separator for these samples, there was a significant reaction, releasing some smoke and discolouring the solution. It is thought this reaction is due to DMSO-d_6 reacting with Na metal dendrites embedded in the separator.

To investigate the purity of DMSO-d_6, a ^{1}H spectrum was collected for pure DMSO-d_6 (Figure 5-18, blue trace), this spectrum is dominated by the residual protons of DMSO at 2.51 ppm, with notable impurities at 3.32 ppm (H_2O), 3.30 ppm (HDO), as well as other smaller signals at 1.15 ppm and 3.70 ppm. A small amount (~25 µL) of pristine (i.e., uncycled) electrolyte was then added to DMSO-d_6. The resulting spectrum (Figure 5-18, red trace) is dominated by the signals for EC, DMC and NEDC, and there are signals from some trace components. Notably peaks at 4.19 ppm, 4.08 ppm, 3.20 ppm, 3.18 ppm (which could correspond to NEMC and methanol). These signals align with the spectrum of electrolyte from a full-cell cycled 8 times (Figure 5-18, green trace) indicating that most of these signals are not due to electrolyte degradation. The spectrum for electrolyte from a half-cell cycled 8 times (Figure 5-18, purple trace) has significantly more degradation products, particularly between 3.30 ppm to 3.60 ppm. However, it is unclear if these come from electrolyte degradation during cycling or from the reaction when DMSO-d_6 was added to the separator.

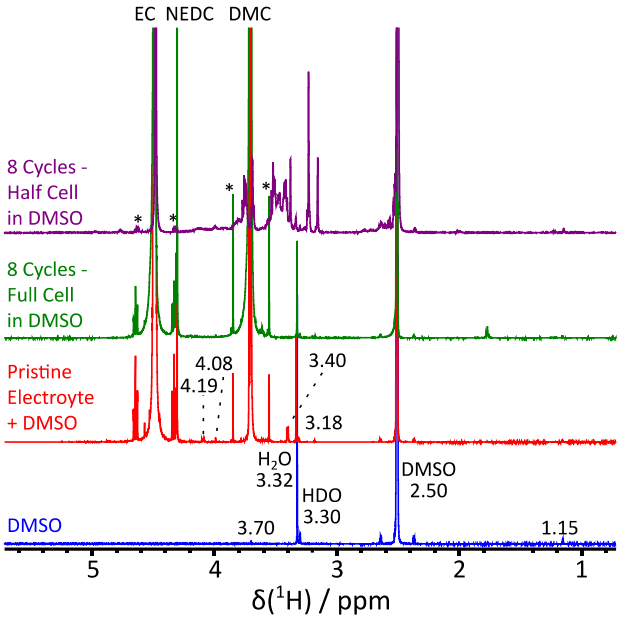

Figure 5-18: Solution NMR spectra collected for pure DMSO-d_6 (blue trace), pristine electrolyte (red trace), electrolyte from a full-cell cycled 8 times (green trace) and electrolyte from a half-cell cycled 8 times (purple trace) all with DMSO-d_6 as a NMR solvent, satellite peaks are marked with asterisks.

To probe if degradation products were coming from reactions with DMSO-d_6, THF-d_8 was also used as an NMR solvent instead. THF-d_8 was chosen as it still a polar solvent, but it is more stable with respect to Na metal. The pristine spectrum for THF-d_8 (Figure 5-19, blue trace), is dominated by the signals for THF at 1.76 ppm and 3.62 ppm. However, there are notably more signals for impurities at 1.33 ppm, 2.56 ppm, 3.26 ppm, 3.31 ppm and 4.44 ppm. The spectrum for the pristine electrolyte (Figure 5-19, red trace) is quite similar to that of the full-cell cycled 8 times (Figure 5-19, green trace), with signals mainly from EC, DMC and NEDC. Although there are additional peaks at 2.87 ppm and 2.90 ppm for the pristine electrolyte and 2.76 ppm and 2.79 ppm for the cycled electrolyte from the full-cell. This further indicates that limited electrolyte degradation occurs for full-cells. For the spectrum of electrolyte from a half-cell cycled 8 times there are noticeably fewer signals, than the equivalent DMSO-d_6 spectrum, however there are some at 4.19 ppm and 5.40 ppm, the first of these could be partially explained by a NEMC-type species. This indicates that most species in the cycled DMSO-d_6 spectra are due to reactions of DMSO with Na metal. Therefore, it can be stated that whilst increased electrolyte degradation does occur for half-cells, the choice of NMR solvent used is crucial.

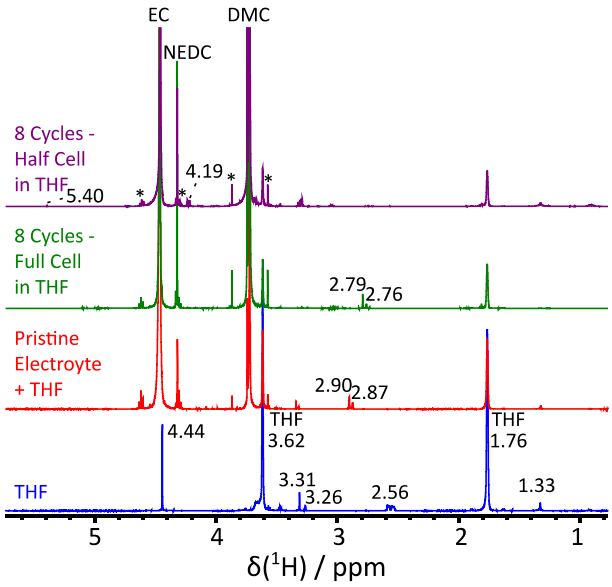

Figure 5-19: Solution NMR spectra collected for pure THF-d_8 (blue trace), pristine electrolyte (red trace), electrolyte from a full-cell cycled 8 times (green trace) and electrolyte from a half-cell cycled 8 times (purple trace) all with THF-d_8 as a NMR solvent, satelitte peaks are marked with asterisks.

^{19}F and ^{31}P solution NMR spectra were also collected for the electrolyte from the cells (Figure 5-20 (a) and (b) respectively). The ^{19}F spectra are dominated by doublets at –72.7 ppm ($^1J_{19F\text{-}31P}$ = 710 kHz), that correspond to $NaPF_6$. However, for the samples cycled 25 times there are some additional signals. For the half-cell there is a doublet at –80.9 ppm ($^1J_{19F\text{-}31P}$ = 950 kHz) that is likely due to $NaPO_2F_2$ and the full cell cycled 25 times there is a singlet at -81.2 ppm which is probably a similar species. The ^{31}P spectra are of limited use and only show septets at –146.1 ppm ($^1J_{31P\text{-}19F}$ = 710 kHz) that correspond to $NaPF_6$.

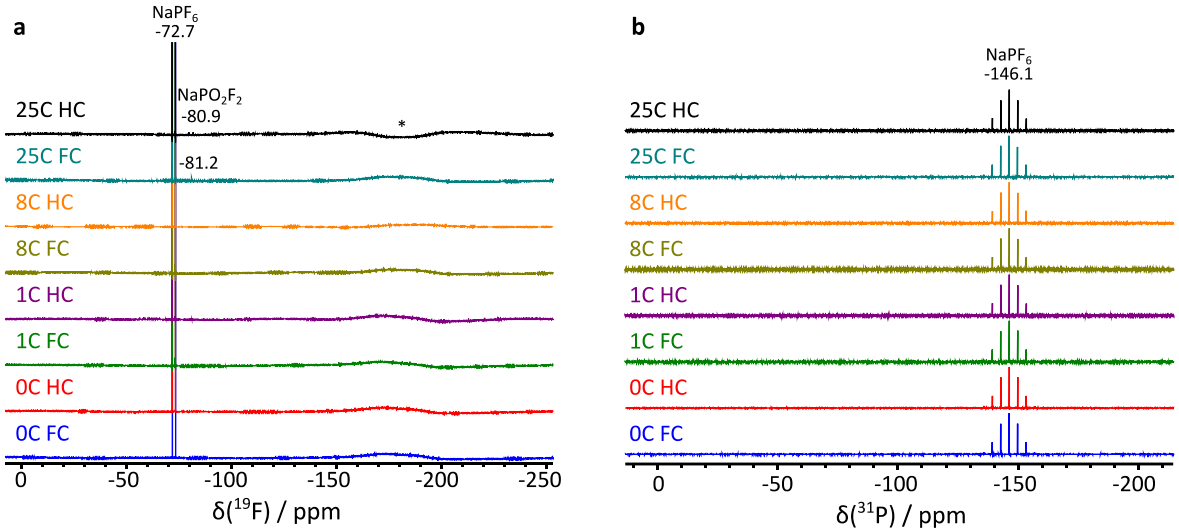

Figure 5-20: (a) ^{19}F and (b) ^{31}P solution NMR spectra for all hard carbon samples, except pristine electrode. X, in "XC" corresponds to the number of times the cells was cycled, "FC" corresponds to a full-cell and "HC" corresponds to a half-cell. The broad features at about ~ –170 in (a) ppm denoted an asterisk come from the PTFE spinner.

5.5 Discussion

In this chapter we have shown that there are notable differences between both the cycling performance and SEI composition for full- and half-cells. The electrochemical data shows that both types of cell had an initial capacity loss for the first half-cycle, which is assigned to SEI formation. However, there was substantially more capacity loss over 25 cycles for the half-cell, compared to the full-cell, possibly indicating a greater amount of SEI formation and/or electrolyte degradation occurs for half-cells.

SSNMR shows that whilst NaF is a major component of the SEI in both full- and half-cells after electrochemical cycling, it is not present for uncycled full-cells despite being present for uncycled half-cells. This indicates that the presence of Na metal has a strong influence on the amount and composition of the SEI formed. However, whilst SSNMR is able to detect SEI components, its lack of surface specificity means it must be used together with other techniques to gain a better understanding of the SEI.

Similarly, XPS spectra showed that the surface of uncycled hard carbon from full-cells was very similar to that of a pristine electrode, unlike uncycled electrodes from half-cells which appeared to show SEI formation. This suggests that there is minimal SEI formation for uncycled full-cells, where Na is not present. For the cycled cells however, all samples show SEI formation and NaF is a common SEI component. It was also observed that Na fluorophosphates, such as $NaPO_2F_2$, Na alkyl carbonates (such as NEDC) and Na_2CO_3 are minor SEI components. Although more NaF and Na fluorophosphates are observed for full-cells, which could be due to these species being screened by other SEI components in half-cells. It is highly likely that these additional SEI components are for more organic or polymeric in nature as more of these are observed for half-cells. For example, in the O1*s* spectra there is an increased amount of C-O groups, which is expected for polymeric SEI components. The C1*s* spectra also show a similar trend although it is harder to confirm this trend as to more C environments being present, which means there is significantly more peak overlap. XPS provides some evidence that transition metal dissolution occurs for full-cells as Ti2*p* signals are observed for the cycled full-cells and not for cycled half-cells. However, due to a combination of low signal intensity and peak overlap for Mn2*p* and Ni2*p* regions, it is not possible to say if these metals also undergo dissolution.

Likewise, solution NMR shows that there is minimal electrolyte degradation and/or soluble SEI formation for full-cells, even after cycling up to 25 times. For half-cells there is significantly more electrolyte degradation, with species such as NEMC becoming more prominent on extended cycling. However, care must be taken when preparing samples for solution NMR as DMSO-d_6 reacts with any Na metal imbedded in the separator between the electrodes. Despite this, even when an NMR solvent

more stable to Na metal, such as THF-d_8, more electrolyte degradation products are observed for half-cells.

Therefore, a model similar to the mosaic model suggested for LIBs can be proposed that for SEIs formed in cycled full and half Na cells, which is illustrated in Figure 5-21. The SEIs formed in both types of cell appear to have a more inorganic layer closer to the surface of the electrode that consists salts such as NaF, with other species such as $Na_2PO_2F_2$ and Na_2CO_3 present. The full cell has likely has a thin organic SEI consisting mainly of Na alkyl carbonates such as NEDC, as well as some polymeric species. It is likely that there are some transition metal species, Ti based ones The half cell has a thicker organic SEI layer, with an increased amount of polymers as well as additional species, such as NEMC present.

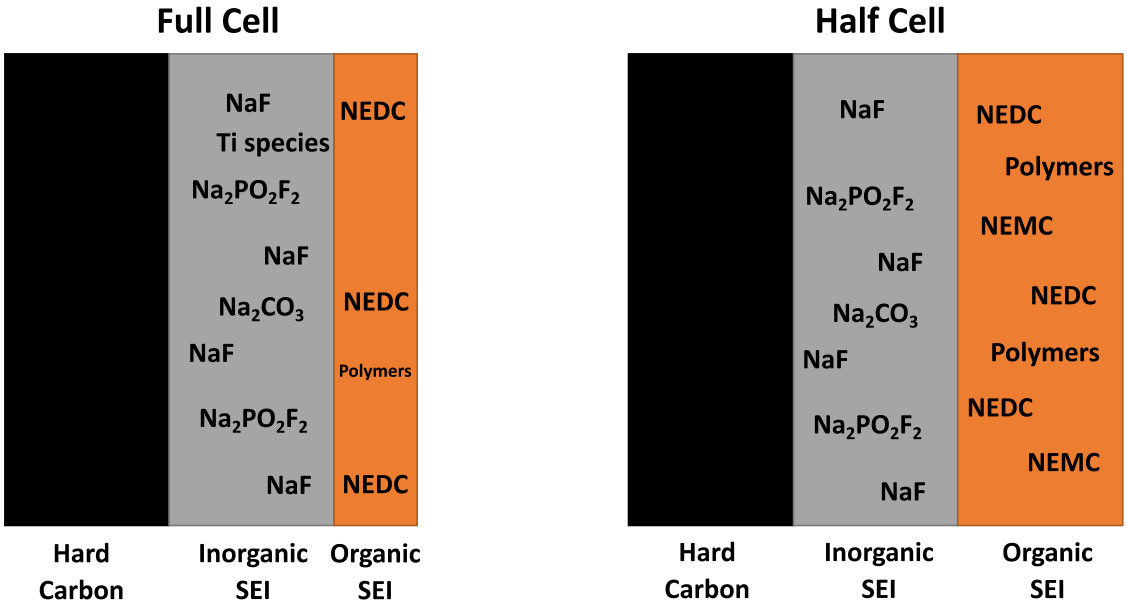

Figure 5-21: Schematic illustrations demonstrating the differences between the SEIs formed in full and half cells.

5.5.1 Formation of SEI Species

Inorganic species such as NaF and $NaPO_2F_2$ are known to form from the decomposition of $NaPF_6$ in the presence of H_2O[140], as shown in Equations (5.1) and (5.2). As more NaF is observed for uncycled half-cells than full-cells, it is likely that the HF produced in these reactions reacts with Na to generate more NaF. As uncycled were analysed after three days, it is unclear if HF formation in half cells is spontaneous or occurs gradually over several days.

$$NaPF_6 + H_2O \rightleftharpoons NaF + POF_3 + 2HF \quad (5.1)$$

$$POF_3 + H_2O \rightleftharpoons PO_2F_2^- + HF + H^+ \quad (5.2)$$

NEDC probably forms in a similar manner to that reported for LEDC.[141] This proceeds via a two-step reaction, as shown in Figure 5-22 (a), in the first step EC undergoes a two-step reaction, the

first step is a ring opening reduction to form a radical species, and two of these radical species combine to form NEDC and ethene gas (although as NEDC is also observed for the pristine electrolyte, it is possible that a similar reaction occurs in the absence of Na metal). However, the radical intermediate could enable other reactions to occur. For example, the radical could initialise anionic polymerisation,[142] by either attacking EC directly or by losing CO_2 to form a smaller radical species that goes onto attack EC. Either way, these types of reactions would explain the observation of oligomeric and polymeric PEG-type species observed in XPS and solution NMR. Both the formation of NEDC and anionic polymerisation would be expected to be accelerated by Na metal as it is a strong reducing agent, which could accelerate the formation of the radical species.

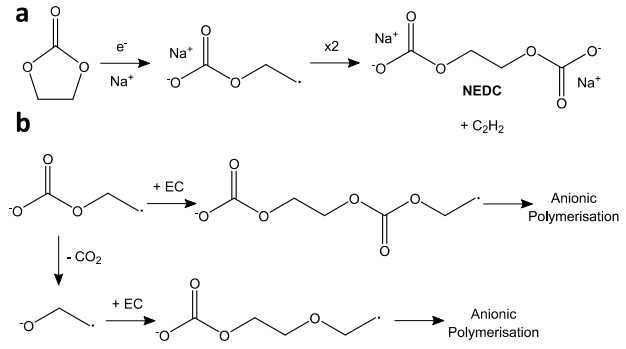

Figure 5-22: Possible reaction pathways for (a) the formation of NEDC by reductive ring opening of EC or (b) anionic polymerisation of EC.

NEMC is also observed in greater quantities for half-cells. It has previously been reported that the Li equivalent forms by base driven hydrolysis of either EC, which continues to form ethylene glycol and CO_2 (Figure 5-23 (a)) or NEDC which also forms $NaHCO_3$ (Figure 5-23 (b)).[138] It therefore makes sense that these reactions could be occurring at a faster rate in the presence of Na metal as it is more likely to form OH^- from any trace moisture in the electrolyte.

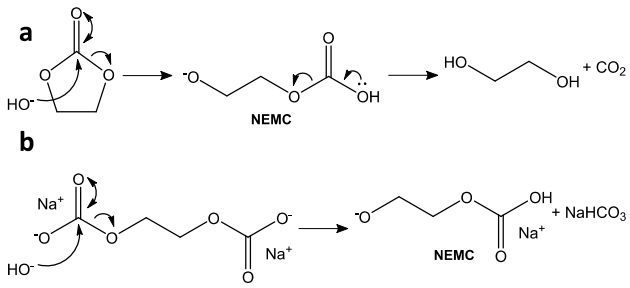

Figure 5-23: Possible reaction pathways for the base-driven hydrolysis of (a) EC or (b) NEDC to form NEMC

5.6 Conclusion

In this chapter, we have studied the SEI formed in half-cells and full-cells using a variety of techniques. The electrochemical data showed that whilst both full- and half-cells showed capacity loss on extended cycling, there was more capacity loss for the full-cell, possibly indicating a greater amount

of electrolyte degradation and/or SEI formation. All three analysis techniques have shown that there is minimal SEI formation on hard carbon for an uncycled full-cell, but an uncycled half-cell does have some SEI/electrolyte degradation products, indicating that Na metal does influence the SEI formed. SEI is then present for cycled electrodes and appears to increase on subsequent cycling.

SSNMR and XPS show that NaF is a major component of the SEI in both full- and half-cells on extended cycling, XPS is also shows that other species such as Na alkyl carbonates, $NaPO_2F_2$ and Na_2CO_3 are also present in the SEI. However, the signals for NaF and $NaPO_2F_2$ are screened in half-cells by the increased amount of organic or polymeric SEI. This is supported by solution NMR, which shows the presence of an increased amount of organic electrolyte degradation products for half-cells, especially on extended cycling. Furthermore, XPS provides some evidence that transition metal dissolution occurs for these cells as Ti is observed in the SEI of hard carbon cycled in full-cells. Peak overlap means that it is hard to tell dissolution also occurs for Ti and Mn, but it is possible that Ti might be closer to the surface of the cathode than the other metals leading to more dissolution. The insights gained about the SEI could enable improved electrolytes to be designed, with additives that enable the formation of a more stable SEI that has better capacity retention, and overall electrochemical performance.

6 Conclusions

Energy storage is set to become increasingly important in the modern world, especially for large-scale applications such as grid storage of renewable energy. Whilst LIBs are currently the state-of-the-art system for energy storage, there are concerns relating to their cost, as well as the environmental and ethical issues associated with extracting their raw materials. Therefore, research efforts have focused on developing alternatives to LIBs. One of these alternatives is NIBs which have the potential to be a cheaper and more environmentally friendly way of storing energy. Due to the parallels between the systems, it is also hoped that a lot of the technology developed for LIBs could be transferred to NIBs, but this is not always the case. When researching electrodes for NIBs, attention has not always been paid to the electrolyte used and how it interacts with the electrode. In this thesis we set out to investigate two key interactions between electrolytes and carbon anodes for NIBs. These were solvent co-intercalation and the formation of an SEI

Firstly, co-intercalation of diglyme with Na^+ ions into graphite (which Na does not intercalate into with normal carbonate electrolytes) was investigated. This was done using several techniques including NMR and TGA. The same techniques were then also used to provide evidence that diglyme also co-intercalates into disordered hard carbons, albeit to a lesser extent than in graphite.

The dynamics of diglyme co-intercalated into hard carbon was then investigated using a combination of ^2H SSNMR and simulations. It was found that the molecular rotation model previously proposed for the motion of diglyme co-intercalated into graphite, had to be adapted by including a lognormal distribution of rotation rates. This indicates that hard carbon has more space for diglyme to be move in than graphite. Whilst this is likely a simplified model, it provides a reasonable approximation for the more complex motion that is probably occurring for diglyme molecules intercalated in hard carbon. This work was taken further by comparing the motion of diglyme in hard carbon at different states of charge. This provided information about the structural changes hard carbon undergoes during sodiation. For example, the motion of diglyme in hard carbon electrodes sodiated to the slope have broadly similar degrees of motion. In contrast, there is then a significant increase in the motion of diglyme for hard carbon sodiated to the plateau. This suggests that diglyme molecules have more space to move in; this could be due to hard carbon expanding on sodiation or by diglyme molecules migrating to the pores of the material.

By comparing fully sodiated hard carbons with different specific capacities, it was found that as capacity increases, the motion of diglyme decreases. One explanation for this could be that higher capacity hard carbons have a smaller interlayer spacing and the pores are filled with quasi-metallic Na. Together these effects mean there is limited space for diglyme to move in. Whereas the lower capacity hard carbon, which has fewer pores, but larger interlayer spacings has more space for Na-diglyme complexes to move in. Therefore, the dynamics of co-intercalated diglyme molecules can be used to

provide information about the structure and sodiation mechanisms of hard carbons. Furthermore, the insights gained from these interactions could be used to help design better anodes for NIBs with higher capacities and longer lasting reversibility.

The formation of an SEI is of crucial importance to the performance of a NIB, however most of the work to study the SEI only takes place in half-cells where Na metal is present. This is despite Na being a strong reducing agent which likely influences the SEI and electrolyte degradation products formed. Therefore, the SEI formed on hard carbon anodes in full- and half-cells was compared using a combination of SSNMR, solution NMR and XPS. All three analysis techniques have shown that there is minimal SEI formation on hard carbon for an uncycled full-cell, but an uncycled half-cell does have some SEI and/or electrolyte degradation. SEI is then present for all cycled electrodes and appears to increase on subsequent cycling. Notably, half-cells have an increased amount of organic or polymeric SEI, due to Na metal degrading the electrolyte solvents and therefore care must be taken when analysis the SEI formed in half-cells. Some evidence was also provided that transition metal dissolution occurs in full-cells, however this was only observed for Ti.

Overall, we have demonstrated that the choice of an electrolyte for use in a NIB is not trivial and that the interactions between an electrolyte and the electrodes can alter the electrochemical performance of a cell, as well as being a way (in the case of glymes) to probe the structure of electrodes. The insights gained in this thesis could aid the design of better hard carbon anodes, possibly with higher capacities, as well as providing a way to investigate the structure of other battery electrode materials, that are not currently fully understood. Additionally, the information gained about the SEI could enable improved electrolytes to be designed, with additives that enable the formation of a more stable SEI that has better capacity retention, and overall electrochemical performance. Therefore, future research into NIBs should consider in more detail the interactions between electrodes and electrolytes.

7 References

1 M. E. Mann, S. Rahmstorf, K. Kornhuber, B. A. Steinman, S. K. Miller and D. Coumou, *Sci. Rep.*, 2017, **7**, 45242.

2 P. Tans and R. Keeling, Trends in Atmospheric Carbon Dioxide, gml.noaa.gov/ccgg/trends/, (accessed January 14, 2022).

3 D. Larcher and J.-M. Tarascon, *Nat. Chem.*, 2014, **7**, 19.

4 E. J. Cairns and P. Albertus, *Annu. Rev. Chem. Biomol. Eng.*, 2010, **1**, 299–320.

5 G. E. Blomgren, *J. Electrochem. Soc.*, 2017, **164**, A5019–A5025.

6 L. Lu, X. Han, J. Li, J. Hua and M. Ouyang, *J. Power Sources*, 2013, **226**, 272–288.

7 B. Dunn, H. Kamath and J.-M. Tarascon, *Science (1979)*, 2011, **334**, 928–935.

8 D. B. Agusdinata, W. Liu, H. Eakin and H. Romero, *Environ. Res. Lett.*, 2018, **13**, 123001.

9 S. S. Sharma and A. Manthiram, *Energy Environ. Sci.*, 2020, **13**, 4087–4097.

10 N. P. Kumar, Y. Liangtao, B. Wolfgang and A. Philipp, *Angew. Chem. Int. Ed.*, 2017, **57**, 102–120.

11 K. Hans Wedepohl, *Geochim. Cosmochim. Acta*, 1995, **59**, 1217–1232.

12 Y. Kim, K.-H. Ha, S. M. Oh and K. T. Lee, *Chem. Eur. J.*, 2014, **20**, 11980–11992.

13 R. D. Shannon, *Acta Crystallogr.*, 1976, **32**, 751.

14 A. Bauer, J. Song, S. Vail, W. Pan, J. Barker and Y. Lu, *Adv. Energy Mater.*, 2018, **8**, 1702869.

15 S. Komaba, T. Ishikawa, N. Yabuuchi, W. Murata, A. Ito and Y. Ohsawa, *ACS Appl. Mater. Interfaces*, 2011, **3**, 4165–4168.

16 W. Xu, J. Wang, F. Ding, X. Chen, E. Nasybulin, Y. Zhang and J. G. Zhang, *Energy Environ. Sci.*, 2014, **7**, 513–537.

17 R. Wang, W. Cui, F. Chu and F. Wu, *J. Energy Chem.*, 2020, 48, 145–159.

18 C. M. Hayner, X. Zhao and H. H. Kung, *Annu. Rev. Chem. Biomol. Eng.*, 2012, **3**, 445–471.

19 J. R. Dahn, *Phys. Rev. B*, 1991, **44**, 9170–9177.

20 P. Ge and M. Fouletier, *Solid State Ion.*, 1988, **28–30**, 1172–1175.

21 R. Suresh Babu and M. Pyo, *J. Electrochem. Soc.*, 2014, **161**, A1045–A1050.

22 Z. Jin, Z. Xiaoxi, Z. Yujie, X. Yunhua and W. Chunsheng, *Adv. Funct. Mater.*, 2016, **26**, 8103–8110.

23 H. Moriwake, A. Kuwabara, C. A. J. Fisher and Y. Ikuhara, *RSC Adv.*, 2017, **7**, 36550–36554.

24 R. E. Franklin, *Proc. R. Soc. A*, 1951, **209**, 196–218.

25 R. Väli, A. Jänes, T. Thomberg and E. Lust, *Electrochim. Acta*, 2017, **253**, 536–544.

26 N. Sun, H. Liu and B. Xu, *J. Mater. Chem. A*, 2015, **3**, 20560–20566.

27 D. A. Stevens and J. R. Dahn, *J. Electrochem. Soc.*, 2000, **147**, 1271–1273.

28 Y. Liu, J. S. Xue, T. Zheng and J. R. Dahn, *Carbon N Y*, 1996, **34**, 193–200.

29 E. Irisarri, A. Ponrouch and M. R. Palacin, *J. Electrochem. Soc.*, 2015, **162**, A2476–A2482.

30 P. J. F. Harris, *Crit. Rev. Solid State Mater. Sci.*, 2005, **30**, 235–253.

31 J. M. Stratford, P. K. Allan, O. Pecher, P. A. Chater and C. P. Grey, *Chem. Commun.*, 2016, **52**, 12430–12433.

32 Y. Morikawa, S. ichi Nishimura, R. ichi Hashimoto, M. Ohnuma and A. Yamada, *Adv. Energy Mater.*, 2020, **10**, 1–9.

33 H. Au, H. Alptekin, A. C. S. Jensen, E. Olsson, C. A. O. Keefe, T. Smith, M. Crespo-ribadeneyra, T. F. Headen, C. P. Grey, Q. Cai and J. Drew, *Energy Environ. Sci.*, 2020, **13**, 3469.

34 C. Matei Ghimbeu, J. Górka, V. Simone, L. Simonin, S. Martinet and C. Vix-Guterl, *Nano Energy*, 2018, **44**, 327–335.

35 A. Gomez-Martin, J. Martinez-Fernandez, M. Ruttert, M. Winter, T. Placke and J. Ramirez-Rico, *Chem. Mater.*, 2019, **31**, 7288–7299.

36 G. Çakmak and T. Öztürk, *Diam. Relat. Mater.*, 2019, **96**, 134–139.

37 P. J. F. Harris, *Journal of Materials Science*, 2013, 48, 565–577.

38 Z. Wang, X. Feng, Y. Bai, H. Yang, R. Dong, X. Wang, H. Xu, Q. Wang, H. Li, H. Gao and C. Wu, *Adv. Energy Mater.*, 2021, **11**, 2003854.

39 J. M. Stratford, A. K. Kleppe, D. S. Keeble, P. A. Chater, S. S. Meysami, C. J. Wright, J. Barker, M. M. Titirici, P. K. Allan and C. P. Grey, *J. Am. Chem. Soc.*, 2021, **143**, 14274–14286.

40 W. D. Knight, *Phys. Rev.*, 1949, **76**, 1259–1260.

41 K. Gotoh, T. Ishikawa, S. Shimadzu, N. Yabuuchi, S. Komaba, K. Takeda, A. Goto, K. Deguchi, S. Ohki, K. Hashi, T. Shimizu and H. Ishida, *J. Power Sources*, 2013, **225**, 137–140.

42 B. Jache and P. Adelhelm, *Angew. Chem.*, 2014, **53**, 10169–10173.

43 A. C. S. Jensen, H. Au, S. Gärtner, M. Titirici and A. J. Drew, *Batt. Supercaps*, 2020, **3**, 1306–1310.

44 B. Jache, J. O. Binder, T. Abe and P. Adelhelm, *Phys. Chem. Chem. Phys.*, 2016, **18**, 14299–14316.

45 M. Goktas, B. Akduman, P. Huang, A. Balducci and P. Adelhelm, *J. Phys. Chem. C*, 2018, **122**, 26816–26824.

46 S. Komaba, Y. Matsuura, T. Ishikawa, N. Yabuuchi, W. Murata and S. Kuze, *Electrochem. Commun.*, 2012, **21**, 65–68.

47 A. Darwiche, C. Marino, M. T. Sougrati, B. Fraisse, L. Stievano and L. Monconduit, *J. Am. Chem. Soc.*, 2012, **134**, 20805–20811.

48 L. Baggetto, J. K. Keum, J. F. Browning and G. M. Veith, *Electrochem. Commun.*, 2013, **34**, 41–44.

49 S. I. R. Costa, Y. S. Choi, A. J. Fielding, A. J. Naylor, J. M. Griffin, Z. Sofer, D. O. Scanlon and N. Tapia-Ruiz, *Chem. Eur. J.*, 2021, **27**, 3875–3886.

50 R. J. Gummow, M. M. Thackeray, W. I. F. David and S. Hull, *Mat. Res. Bull.*, 1992, **27**, 327–337.

51 N. Nitta, F. Wu, J. T. Lee and G. Yushin, *Mater. Today*, 2015, 18, 252–264.

52 N. Yabuuchi, H. Yoshida and S. Komaba, *Electrochemistry*, 2012, **80**, 716–719.

53 M. D. Slater, D. Kim, E. Lee and C. S. Johnson, *Adv. Funct. Mater.*, 2013, **23**, 947–958.

54 J.-M. Tarascon, *Joule*, 2020, **4**, 1616–1620.

55 A. Rudola, A. J. R. Rennie, R. Heap, S. S. Meysami, A. Lowbridge, F. Mazzali, R. Sayers, C. J. Wright and J. Barker, *J. Mater. Chem. A*, 2021, 9, 8279–8302.

56 S. Mariyappan, Q. Wang and J. M. Tarascon, *J. Electrochem. Soc.*, 2018, **165**, A3714–A3722.

57 L.-L. Zheng, Y. Xue, B.-S. Liu, Y.-X. Zhou, S.-E. Hao and Z. Wang, *Ceram. Int.*, 2017, **43**, 4950–4956.

58 J. Qian, C. Wu, Y. Cao, Z. Ma, Y. Huang, X. Ai and H. Yang, *Adv. Energy Mate.*, 2018, 8.

59 K. Xu, *Chem. Rev.*, 2004, **104**, 4303–4417.

60 A. Bhide, J. Hofmann, A. Katharina Durr, J. Janek and P. Adelhelm, *Phys. Chem. Chem. Phys.*, 2014, **16**, 1987–1998.

61 A. Ponrouch, D. Monti, A. Boschin, B. Steen, P. Johansson and M. R. Palacin, *J. Mater. Chem. A*, 2015, **3**, 22–42.

62 R. Payne and I. E. Thbodoroij, *J. Phys. Chem*, 1972, **76**, 2892–2900.

63 W. M. Haynes, D. R. Lide and T. J. Bruno, Eds., *CRC Handbook of Chemistry and Physics*, CRC Press, Boca Raton, 95th edn., 2014.

64 H. Zhao, S.-J. Park, F. Shi, Y. Fu, V. Battaglia, P. N. Ross and G. Liu, *J. Electrochem. Soc.*, 2014, **161**, A194–A200.

65 E. Markevich, G. Salitra and D. Aurbach, *ACS Energy Lett.*, 2017, **2**, 1337–1345.

66 L. B. Huang, G. Li, Z. Y. Lu, J. Y. Li, L. Zhao, Y. Zhang, X. D. Zhang, K. C. Jiang, Q. Xu and Y. G. Guo, *ACS Appl. Mater.Interfaces*, 2021, **13**, 24916–24924.

67 X. Li, Z. Yin, X. Li and C. Wang, *Ionics (Kiel)*, 2014, **20**, 795–801.

68 A. L. Michan, Bharathy. S. Parimalam, M. Leskes, R. N. Kerber, T. Yoon, C. P. Grey and B. L. Lucht, *Chemi. Mater.*, 2016, **28**, 8149–8159.

69 J. Song, B. Xiao, Y. Lin, K. Xu and X. Li, *Adv. Energy Mater.*, 2018, 1703082.

70 M. N. Obrovac and V. L. Chevrier, *Chem. Rev.*, 2014, **114**, 11444–11502.

71 B. Jerliu, E. Hüger, L. Dörrer, B. K. Seidlhofer, R. Steitz, V. Oberst, U. Geckle, M. Bruns and H. Schmidt, *J. Phys. Chem. C*, 2014, **118**, 9395–9399.

72 A. L. Michan, G. Divitini, A. J. Pell, M. Leskes, C. Ducati and C. P. Grey, *J. Am. Chem. Soc.*, 2016, **138**, 7918–7931.

73 E. Peled, *J. Electrochem. Soc.*, 1997, **144**, L208.

74 R. Mogensen, D. Brandell and R. Younesi, *ACS Energy Lett.*, 2016, **1**, 1173–1178.

75 B. Lee, E. Paek, D. Mitlin and S. W. Lee, *Chemical Reviews*, 2019.

76 K. Pfeifer, S. Arnold, Ö. Budak, X. Luo, V. Presser, H. Ehrenberg and S. Dsoke, *J. Mater. Chem. A*, 2020, **8**, 6092–6104.

77 B. Marinho, M. Ghislandi, E. Tkalya, C. E. Koning and G. de With, *Powder Technol.*, 2012, **221**, 351–358.

78 K. A. See, M. A. Lumley, G. D. Stucky, C. P. Grey and R. Seshadri, *J. Electrochem. Soc.*, 2017, **164**, A327–A333.

79 M. Dahbi, T. Nakano, N. Yabuuchi, T. Ishikawa, K. Kubota, M. Fukunishi, S. Shibahara, J.-Y. Son, Y.-T. Cui, H. Oji and S. Komaba, *Electrochem. Commun.*, 2014, **44**, 66–69.

80 E. M. Purcell, H. C. Torrey and R. V. Pound, *Phys. Rev.*, 1946, **69**, 37–38.

81 F. Bloch, *Phys. Rev.*, 1946, **70**, 460–474.

82 M. J. Duer, *Introduction to Solid-State NMR Spectroscopy*, Blackwell Science Ltd, Oxford, 1st edn., 2004.

83 C. A. O'Keefe, 2018.

84 G. E. Pake, *J. Chem. Phys.*, 1948, **16**, 327–336.

85 E. L. Hahn, *Phys. Rev.*, 1950, **80**, 580–594.

86 S. R. Hartmann and E. L. Hakn, *Phy. Rev.*, 1962, **128**, 2042–2053.

87 C. Nordling, E. Sokolowski and K. Siegbahn, *Phys. Rev.*, 1957, **105**, 1676–1677.

88 E. Sokolowski, C. Nordling and K. Siegbahn, *Phys. Rev.*, 1958, **110**, 776.

89 H. Hertz, *Ann. Phys.*, 1887, **267**, 983–1000.

90 A. Einstein, *Ann. Phys.*, 1905, 17, 132–148.

91 J. H. Scofield, *J. Electron Spectros. Relat. Phenomena*, 1976, **8**, 129–137.

92 M. P. Seah, *Surf. Interface Anal.*, 2012, **44**, 497–503.

93 A. W. Coats and J. P. Redfern, *Analyst*, 1963, **88**, 906–924.

94 A. R. Shah, R. R. C. Shutt, K. Smith, J. Hack, T. P. Neville, T. F. Headen, D. J. L. Brett, C. A. Howard, T. S. Miller and P. L. Cullen, *J. Phys. Mater.*, 2021, **4**, 042008.

95 W. H. Bragg and W. L. Bragg, *Proc. R. Soc. Lond.*, 1913, **88**, 428–438.

96 H. M. Rietveld, *J. Appl. Cryst.*, 1969, **2**, 65–71.

97 W. Luo, J. Wan, B. Ozdemir, W. Bao, Y. Chen, J. Dai, H. Lin, Y. Xu, F. Gu, V. Barone and L. Hu, *Nano Lett.*, 2015, **15**, 7671–7677.

98 D. A. Stevens and J. R. Dahn, *J. Electrochem. Soc.*, 2001, **148**, A803.

99 H. Kim, J. Hong, Y. U. Park, J. Kim, I. Hwang and K. Kang, *Adv. Funct. Mater.*, 2015, **25**, 534–541.

100 S. C. Jung, Y. J. Kang and Y. K. Han, *Nano Energy*, 2017, **34**, 456–462.

101 N. Leifer, M. F. Greenstein, A. Mor, D. Aurbach and G. Goobes, *Journal of Physical Chemistry C*, 2018, **122**, 21172–21184.

102 K. Gotoh, H. Maruyama, T. Miyatou, M. Mizuno, K. Urita and H. Ishida, *J. Phys. Chem. C*, 2016, **120**, 28152–28156.

103 Y. E. Zhu, L. Yang, X. Zhou, F. Li, J. Wei and Z. Zhou, *J Mater. Chem. A*, 2017, **5**, 9528–9532.

104 A. Bielecki and D. P. Burum, *J. Mag. Res., Ser. A*, 1995, **116**, 215–220.

105 L. C. M. van Gorkom, J. M. Hook, M. B. Logan, J. V Hanna and R. E. Wasylishen, *Magn. Reson. Chem.*, 1995, **33**, 791–795.

106 Z. Guan, X. Shen, R. Yu, Z. Wang and L. Chen, *Electrochim. Acta*, 2016, **222**, 1365–1370.

107 Y. Maniwa, M. Sato, K. Kume, M. E. Kozlov and M. Tokumoto, *Carbon N Y*, 1996, **34**, 1287–1291.

108 A. Wong and G. Wu, *J. Phys. Chem. A*, 2000, **104**, 11844–11852.

109 J. Conard, H. Estrade, P. Lauginie, H. Fuzellier, G. Furdin and R. Vasse, *Physica B+C*, 1980, **99**, 521–524.

110 X. Dou, I. Hasa, D. Saurel, C. Vaalma, L. Wu, D. Buchholz, D. Bresser, S. Komaba and S. Passerini, *Mater. Today*, 2019, **23**, 87–104.

111 C. H. Pennington and V. A. Stenger, *Rev. Mod. Phys.*, 1996, **68**, 855–910.

112 V. Nicholas Vukotic, C. A. O'Keefe, K. Zhu, K. J. Harris, C. To, R. W. Schurko and S. J. Loeb, *J. Am. Chem. Soc.*, 2015, **137**, 9643–9651.

113 C. I. Ratcliffe, J. A. Ripmeester, G. W. Buchanan and J. K. Denike, *J. Am. Chem. Soc.*, 1992, **114**, 3294–3299.

114 N. J. Stone, *At. Data Nuc. Data Tab.*, 2016, **111–112**, 1–28.

115 J. R. De Laeter, J. K. Böhlke, P. De Bièvre, H. Hidaka, H. S. Peiser, K. J. R. Rosman and P. D. P. Taylor, *Pure Appl. Chem*, 2003, **75**, 683–800.

116 C. Zhao, Q. Wang, Y. Lu, B. Li, L. Chen and Y.-S. Hu, *Sci. Bull.*, 2018, **63**, 1125–1129.

117 R. L. Vold and G. L. Hoatson, *J. Mag. Res.*, 2009, **198**, 57–72.

118 V. Macho, L. Brombacher and H. W. Spiess, *Appl. Magn. Reson.*, 2001, **20**, 405–432.

119 K. Gotoh, M. Maeda, A. Nagai, A. Goto, M. Tansho, K. Hashi, T. Shimizu and H. Ishida, *J. Power Sources*, 2006, **162**, 1322–1328.

120 Kureha Battery Materials Co. Ltd., Carbotron P(J), http://www.kureha.co.jp/development/story/pdf/catalog_hc_eg_20120924.pdf, (accessed January 14, 2022).

121 U. Werner and W. Müller-Warmuth, *Z. Phys. B*, 1993, **91**, 65–76.

122 K. Edström, M. Herstedt and D. P. Abraham, *J. Power Sources*, 2006, **153**, 380–384.

123 H. Buqa, A. Würsig, J. Vetter, M. E. Spahr, F. Krumeich and P. Novák, *J. Power Sources*, 2006, **153**, 385–390.

124 M. Nie, D. P. Abraham, Y. Chen, A. Bose and B. L. Lucht, *J. Phys. Chem.C*, 2013, **117**, 13403–13412.

125 M. Balasubramanian, H. S. Lee, X. Sun, X. Q. Yang, A. R. Moodenbaugh, J. McBreen, D. A. Fischer and Z. Fu, *Electrochem. Solid-State Lett.*, 2002, **5**, A22–A25.

126 S. Hy, Felix, Y.-H. Chen, J. Liu, J. Rick and B.-J. Hwang, *J. Power Sources*, 2014, **256**, 324–328.

127 Y. Jin, N.-J. H. Kneusels, P. C. M. M. Magusin, G. Kim, E. Castillo-Martínez, L. E. Marbella, R. N. Kerber, D. J. Howe, S. Paul, T. Liu and C. P. Grey, *J. Am. Chem. Soc.*, 2017, **139**, 14992–15004.

128 J. A. Gilbert, I. A. Shkrob and D. P. Abraham, *J. Electrochem. Soc.*, 2017, **164**, A389–A399.

129 I. Hasa, D. Buchholz, S. Passerini and J. Hassoun, *ACS Appl. Mater. Interfaces*, 2015, **7**, 5206–5212.

130 Y. Pan, Y. Zhang, B. S. Parimalam, C. C. Nguyen, G. Wang and B. L. Lucht, *J. Electroanal. Chem.*, 2017, **799**, 181–186.

131 J. Fondard, E. Irisarri, C. Courrèges, M. R. Palacin, A. Ponrouch and R. Dedryvère, *J. Electrochem. Soc.*, 2020, **167**, 070526.

132 L. A. Ma, A. J. Naylor, L. Nyholm and R. Younesi, *Angew. Chem. Int. Ed.*, 2021, **60**, 4855–4863.

133 D. M. C. Ould, S. Menkin, C. A. O'Keefe, F. Coowar, J. Barker, C. P. Grey and D. S. Wright, *Angew. Chem. Int. Ed.*, 2021, **60**, 24882–24887.

134 R. Morita, K. Gotoh, M. Fukunishi, K. Kubota, S. Komaba, N. Nishimura, T. Yumura, K. Deguchi, S. Ohki, T. Shimizu and H. Ishida, *J. Mater. Chem. A*, 2016, **4**, 13183–13193.

135 V. di Castro and G. Polzonetti, *J. Electron Spectros. Relat. Phenomena*, 1989, **48**, 117–123.

136 S. Creager, L. A. Hockett, G. K. Rowe, K. Aramaki, M. Yamada, H. Nishihara, K. Shimura, B. Gijutsu, T. J. Lin, B. H. Chun, H. K. Yasuda, D. J. Yang, K. K. Lian, D. W. Kirk and S. J. Thorpe, *J. Electrochem. Soc.*, 1995, **142**, 3704–3712.

137 W. E. Slinkard and P. B. Degroot, *J. Catal.*, 1981, **68**, 423–432.

138 B. L. D. Rinkel, D. S. Hall, I. Temprano and C. P. Grey, *J. Am. Chem. Soc.*, 2020, **142**, 15058–15074.

139 D. E. O'Connor and W. I. Lyness, *J. Org. Chem.*, 1965, **30**, 52.

140 P. Barnes, K. Smith, R. Parrish, C. Jones, P. Skinner, E. Storch, Q. White, C. Deng, D. Karsann, M. L. Lau, J. J. Dumais, E. J. Dufek and H. Xiong, *J. Power Sources*, , DOI:10.1016/j.jpowsour.2019.227363.

141 K. Xu, G. v. Zhuang, J. L. Allen, U. Lee, S. S. Zhang, P. N. Ross and T. R. Jow, *J. Phys. Chem. B*, 2006, **110**, 7708–7719.

142 I. A. Shkrob, Y. Zhu, T. W. Marin and D. Abraham, *J. Phys. Chem. C*, 2013, **117**, 19255–19269.

8 Appendix

Table A1: Experimental parameters used to collect MAS SSNMR spectra in Chapter 3.

Experiment	MAS Rate / kHz	90° Pulse Length / µs	Recycle Delay / s	Contact Time / µs	Hartmann-Hahn Matching Power / kHz
^{13}C Hahn Echo	10, 20, 25 or 40	2.09	2	-	-
^{19}F Hahn Echo	10 or 20	2.27	3	-	-
^{23}Na Single Pulse	10, 25 or 40	3.17	1	-	-
^{1}H-^{23}Na CP	10	2.69	1	1000, 5750 or 10000	38 (^{1}H) 81 (^{23}Na)
^{19}F-^{23}Na CP	10	2.30	1	2750 or 6500	76 (^{19}F) 162 (^{23}Na)

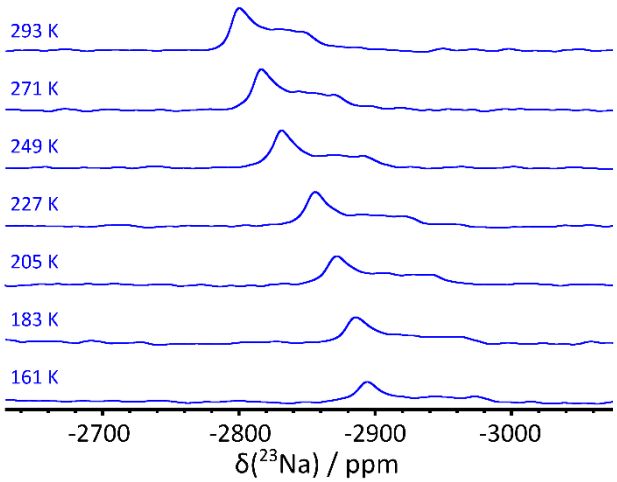

Figure A1: Static SSNMR spectra of $Pb(NO_3)_2$ collected at temperatures ranging from 161 K – 293 K

Table A2: Temperatures determined from the NMR probe compared to temperatures determined from the temperature dependent shifts of $Pb(NO_3)_2$.

Probe Temperature / K	Temperature Determined from $Pb(NO_3)_2$/ K
293	293
273	271
253	249
233	227
213	205
193	183
173	161

Table A3: Experimental parameters used to collect MAS SSNMR spectra in Chapter 5.

Experiment	**MAS Rate / kHz**	**90° Pulse Length / µs**	**Recycle Delay / s**	**Contact Time / µs**	**Hartmann-Hahn Matching Power / kHz**
^{19}F Hahn Echo	20	2.87	5.93	-	-
^{23}Na Hahn Echo	20	3.84	11.00	-	-
^{31}P Hahn Echo	20	1.89	2.00	-	-
^{1}H-^{23}Na CP	10	2.69	1.56	500	38 (^{1}H) 81(^{23}Na)